

A Thesis Submitted for the Degree of PhD at the University of Warwick

Permanent WRAP URL:

<http://wrap.warwick.ac.uk/108759>

Copyright and reuse:

This thesis is made available online and is protected by original copyright.

Please scroll down to view the document itself.

Please refer to the repository record for this item for information to help you to cite it.

Our policy information is available from the repository home page.

For more information, please contact the WRAP Team at: wrap@warwick.ac.uk

STRUCTURE OF ANODIC-OXIDE AND HYDRATED OXIDE FILMS

ON PURE ALUMINIUM

Saleh M. El-Mashri

B.Sc., M.Sc.

A thesis submitted to the University of Warwick
for admission to the degree of Doctor of Philosophy

Department of Physics

January 1985

MEMORANDUM

This thesis is submitted to the University of Warwick in support of my application for admission to the degree of Doctor of Philosophy. It contains an account of my work carried out principally at the Department of Physics of the University of Warwick during the period October 1979 to February 1984 under the supervision of Professor A. J. Forty. No parts of this thesis have been used previously in a degree thesis submitted to this or any other University. The work described is the result of my own independent research except where specifically acknowledged in the text. Some parts of the work have been published as detailed below:

1. El-Mashri, S.M., Forty, A.J., Freeman, L., Smith, D.J. (1981), "Structure of amorphous alumina", proceedings of the electron microscopy and analysis, ed: M.J. Goringe, Inst.Phys.Conf., Series No.61 (Bristol, London: The Institute of Physics), 395 - 398.
2. El-Mashri, S.M., Forty, A.J., Jones, R.G., (1983), "Scanning Electron Microscopy (SEM) and Surface EXAFS (SEXAFS) of Aluminium Oxide prepared Anodically in Phosphoric Acid", Scanning Electron Microscopy 1983/II (pages 569-576).
3. El-Mashri, S.M., Jones, R.G., Forty, A.J. (1983), "The incorporation of a siliceous impurity during the anodic oxidation of aluminium in a sodium tartrate electrolyte. Appl. Surf. Science, 17, 124-130.

4. El-Mashri, S.M., Jones, R.G., Forty, A.J., (1983), "An electron-yield EXAFS study of anodic-oxide and hydrated oxide films on pure aluminium". Philosophical Magazine, 48A, 665-683.
5. Bourdillon, A.J., El-Mashri, S.M., Forty, A.J., (1984), "Application of TEM extended electron energy loss fine structure to the study of aluminium oxide films", Phil. Mag., A49, 341-352.
6. El-Mashri, S.M., (1984), "A morphological study of the anodic-oxide and hydrated-oxide films on pure aluminium", Scanning Electron Microscopy, 1985/I, in press.

It is intended to publish the contents of Chapter Six in the near future.

Saleh M. El-Mashri

ABSTRACT

The technique of electron yield-EXAFS has been used to derive information about the different structures of amorphous films, formed anodically on pure aluminium when various electrolyte solutions are used. It has been found that the uniform non-porous (barrier-type) oxide films which are formed in neutralised sodium tartrate or sodium borate electrolyte are amorphous and have an average Al-O bond length of 0.190 nm. The amorphous oxide produced in neutralised sodium oxalate gives an average Al-O separation of 0.185 nm, while the porous oxides formed in strong aggressive electrolytes, chromic acid and phosphoric acid, have an average Al-O bond length of 0.183 nm and 0.180 nm respectively. Both the non-porous and the porous types of films have also been examined by high resolution scanning electron microscopy. The films formed in neutralised electrolytes show a structureless morphology, while the films prepared in strong acid are shown to have a porous morphology. All these oxide films become hydrated when exposed to hot water at 85°C. The time for complete hydration varies according to whether the film is porous or not. Electron yield-EXAFS analysis of these hydrated films yields two well defined Al-O distances, 0.205 nm and 0.280 nm, which appear to be associated with the formation of an oxy-hydroxide similar in structure to boehmite. The SEM observation of these hydrated films shows a marked change in the micromorphology during hydration. A "cornflake" structure is developed which is related to the oxy-hydroxide structure (boehmite-like phase).

These measured Al-O bond lengths derived from the EXAFS differ,

depending on the nature of the anodising treatment, which suggests different states of aluminium-oxygen coordination. A possible model for the structure of amorphous alumina, based on this information, is proposed. These results are also discussed in relation to the structural chemistry of the hydration process.

ACKNOWLEDGEMENTS

I wish to express my gratitude to Professor A. J. Forty who has introduced me to the subject, for excellent supervision and generous encouragement throughout the course of this work, and for his assiduity in the reading of this manuscript. I am grateful also to Dr. R. F. Pettifer and Dr. D. P. Woodruff for allowing me to use their computer software to carry out the EXAFS analysis and for the excellent discussion with Rob Pettifer, as well as for his interest shown and criticism made. I am grateful to the many people who have helped me in this department, especially Drs. A. Bosland, R. S. Holt, P. Durkin and Mr. M. Ward. I would like to thank the technical staff, particularly Mr. Tim Naylor and Mr. G. Smith, who have assisted me during the course of this work. Thanks also to Miss Sandra Callanan for her careful typing of this manuscript.

I am indebted to the staff of the C.N.R.S. Laboratoire pour l'Utilisation du Rayonnement electromagnetique, Orsay (France), for the use of the ACO synchrotron radiation facility, particularly Dr. P. Lagarde.

My thanks are due to Dr. A.J. Bourdillon for the fruitful discussions and his collaboration in using the electron energy loss facilities at the Metallurgy and Material Science Department at Cambridge University.

I am also grateful to Dr. D. J. Smith and Dr. L. A. Freeman at the Cavendish Laboratory, Cambridge University for their collaboration in using High-Voltage High-Resolution Electron Microscope studies during the course of this study.

I wish to record my love and deep thanks to my wife, Mariam, for her infinite encouragement over the years and in particular during the preparation of this thesis. My love to my children, Sara and Rafiq for their patience. Sincere thanks to my family in Libya for their encouragement and some financial support.

CONTENTS

	<u>PAGE</u>
 <u>CHAPTER 1: General Introduction</u>	
1.1 Introduction	1
1.2 Structure and Composition of anodic aluminium oxide	2
1.2.1. Review of earlier work	2
1.2.2. Summary of the review	9
1.3 The behaviour of anodic aluminium oxide films in water	10
1.4 The aim of the work reported in this thesis	14
1.5 Plan of thesis	16
References	18
 <u>CHAPTER 2: Extended X-ray Absorption Fine Structure: Theory and Modes of Observation</u>	
2.1 Introduction	21
2.2 Theory of EXAFS	21
2.3 The analysis of EXAFS by the Fourier transform method	24
2.4 The determination of phase shift	27
2.5 The derivation of coordination number from the EXAFS	30
2.6 General consideration concerning the measurements of EXAFS	31
2.6.1. Transmission EXAFS	32
2.6.2. Fluorescence EXAFS	35
2.6.3. The electron yield EXAFS	36
2.6.3i The Auger electron yield EXAFS	37
2.6.3ii The total electron yield EXAFS	39
2.7 Summary	39
References	41

	<u>PAGE</u>
<u>CHAPTER 3: The electron yield EXAFS instrumentation and measurement</u>	44
3.1 Introduction	44
3.2 Synchrotron radiation	44
3.3 EXAFS experimental arrangements	45
3.4 Data collection	47
3.5 Normalization of the EXAFS data	48
3.6 The sampling depth of the total electron yield technique	51
3.7 Summary	54
References	56
<u>CHAPTER 4: Sample preparation, EXAFS analysis procedure and results for anodic aluminium oxide films and hydrated oxide films</u>	57
4.1 Introduction	57
4.2 Sample preparation	58
4.2.1 General background	58
4.2.2 Surface preparation of the aluminium substrates prior to anodisation	59
4.2.3 Anodising treatment	59
(i) sodium tartrate solution	60
(ii) sodium oxalate solution	60
(iii) sodium borate solution	60
(iv) phosphoric acid solution	60
(v) chromic acid solution	61
The α -alumina specimen used as the model compound	62
4.2.4 The hydration of the oxide films	

	<u>PAGE</u>
4.3 The analysis of EXAFS data to obtain structural information (Al-O bond length) for the anodic oxide films	64
4.3.1 The EXAFS analysis of the oxide formed in sodium tartrate electrolyte.	65
(i) background subtraction and normalisation of the electron yield spectra	65
(ii) The extraction of the EXAFS oscillation function $\chi(E)$	65
(iii) The conversion of $\chi(E)$, in photon energy space, to $\chi(k)$, in photoelectron wavevector space	66
(iv) Fourier transformation of the EXAFS oscillation function $\chi(k)$	67
(v) The determination of Al-O bond lengths for the anodic oxide formed in sodium tartrate.	69
(vi) Estimation of errors in the EXAFS determination of bond length.	71
4.3.2 The EXAFS results for the oxide formed in sodium oxalate	72
4.3.3 The EXAFS results for the oxide formed in sodium borate	73
4.3.4 The EXAFS results for the oxide formed in chromic acid	73
4.3.5 The EXAFS results for the oxide formed in phosphoric acid.	73
4.3.6 The EXAFS results for the oxide film formed in sodium tartrate electrolyte after hydration.	74
4.3.7 The EXAFS results for the oxide film formed in sodium oxalate electrolyte after hydration	75

	<u>PAGE</u>
4.3.8 The EXAFS results for the oxide films formed in sodium borate electrolyte after hydration	75
4.3.9 The EXAFS results for the oxide film formed in chromic acid electrolyte after hydration	76
4.3.10 The EXAFS results for the oxide film formed in phosphoric acid after hydration.	76
4.4 Summary of results	77
References	80
<u>CHAPTER 5: Micromorphological observations of the anodic-oxide and hydrated oxide.</u>	81
5.1 Introduction	81
5.2 The surface coating technique	81
5.3 SEM observations	82
5.3.1 Micromorphological observations of the oxide and hydrated oxide formed in sodium tartrate solution	83
5.3.2 Micromorphological observations of the oxide and hydrated oxide formed in sodium oxalate solution	84
5.3.3 Micromorphological observations of the oxide and hydrated oxide formed in sodium borate solution	85
5.3.4 Micromorphological observations of the oxide and hydrated oxide formed in phosphoric acid solution	85
5.3.5 Micromorphological observations of the oxide and hydrated oxide formed in chromic acid solution	86
5.4 Summary	87
References	88
<u>CHAPTER 6: Discussion of structure and structural chemistry of hydration of the oxide films</u>	89

	<u>PAGE</u>
6.1 Introduction	89
6.2 The molecular structure of amorphous aluminium oxide	89
6.2.1 General background	89
6.2.2 The relationship between bond length and state of coordination.	91
6.2.3 Comparison with other determinations of co- ordination state	96
6.2.4 A possible model for the local structure of amorphous alumina	98
6.3 The incorporation of impurities in the oxide films	101
6.3.1 The incorporation of silicon impurity in the oxide during the anodic oxidation process	102
6.3.2 The incorporation of phosphorus impurity in the oxide film.	103
6.4 The structure of hydrated alumina films	105
6.5 The structural mechanism of the hydration reaction	106
6.6 Suggestions for further work.	108
References	110
<u>Appendix I</u>	113
<u>Appendix II</u>	114
<u>Appendix III</u>	115

LIST OF FIGURES

		Following Page
2.1	Schematic representation of EXAFS observation in the absorption as a function of photon energy, above the edge. The first 30-30 eV above the edge are the X-ray absorption near edge structure (XANES) and the oscillation modulation above that is the extended X-ray absorption fine structure (EXAFS).	21
2.6.2	Schematic decay processes for core holes leading to X-ray fluorescence or Auger electron emission.	35
2.6.3	Schematic photoemission spectrum of electron emitted from a surface as a function of photon energy.	37
3.2.1	Shows a schematic presentation of some of the possible applications of synchrotron radiation (after Forty, 1979).	45
3.3.1	The experimental arrangement for recording electron yield EXAFS.	45
3.3.2	A photograph showing the monochromator and the sample chamber arrangement.	47
3.3.3	A photograph showing the sample holder (unpolished brass surface), with the actual size of samples mounted and a 25 mm aperture to use for transmission EXAFS measurement.	47
3.4.1	A block diagram of the electronic system used in the electron yield counting.	48
3.4.2	The experimental arrangement for recording the transmission EXAFS.	48

- 3.5.1 The electron yield spectra from the "dirty" 51
brass target versus photon energy for angles
of incidence 40° , 65° and 90° . The
smooth curves are best fit polynomials
(Chebyshev series) to be used to normalise
the electron yield spectra.
- 3.5.2 Illustrates the procedure followed to norma- 51
lise the EXAFS spectrum. Curve 1 is the
recorded electron-yield spectrum for a 50 nm
tartrate formed oxide film; curve 2 is the
polynomial described in figure 3.5.1 adjusted
to fit the electron-yield spectrum prior to
the Al K-edge.
- 3.5.3 Shows the normalised EXAFS spectrum, obtained 51
by subtracting curve 2 from curve 1 and
dividing by curve 2 in figure 5.3.2.
- 3.6.1 The electron yield EXAFS spectra for a series 53
of sodium tartrate formed alumina films with
thicknesses, 50, 100, 300, 400, 500 Å (left-hand
side). The calculated spectra shown on the
right-hand side have been constructed from
the Al transmission EXAFS (curve 1) and the
EXAFS for 500 Å alumina film (curve 2) with
the percentage of oxide contributions shown
to give a fit of the experimental spectra.
- 3.6.2 The electron yield EXAFS spectra for a series 54
of sodium tartrate formed alumina films after
hydration at 85 C for 15 minutes with thicknesses
50, 100, 400 and 500 Å (left-hand side). The
calculated spectra shown on the right-hand
side have been constructed from the pure Al
transmission EXAFS (curve 1) and the EXAFS
for the 500 Å hydrated alumina (curve 2) with
the percentage of hydrated oxide contributions
shown to give a fit of the experimental spectra.

3.6.3	The percentage contribution from the total EXAFS spectrum for various thicknesses of film as deduced from figures 3.6.1 and 3.6.2 and that of Jones and Woodruff (1982). ● denotes results obtained by Jones and Woodruff for borate formed films, ○ are the results obtained in this work for as-formed tartrate films (figure 3.6.1); □ are the results obtained for sodium tartrate formed films, after hydration in hot water at 85°C for 15 minutes (figure 3.6.2). The curve is the theoretical relationship based on calculated by Jones and Woodruff.	54
4.3.1a	The normalised electron-yield for the sodium tartrate formed oxide showing the polynomial used for extracting the EXAFS function $\chi(E)$.	65
4.3.1b	A plot of the fine structure function, $\chi(E)$, against the photon energy (eV) obtained from figure 4.3.1a.	65
4.3.2	The EXAFS function $\chi(k)$ weighted by k^3 for the sodium tartrate-formed oxide. The crosses represent individual data points; the continuous line is the cubic spline fit used for the Fourier transform.	66
4.3.3	The Fourier transform of the EXAFS function shown in figure 4.3.2. The dashed line represents the window function, the dotted line shows the back-Fourier transform.	66
4.3.4	The EXAFS function $\chi(k)$ weighted by k^3 for the model compound (α -Al ₂ O ₃ , "Sapphire specimen"). The crosses individual data points; the continuous line is the cubic spline fit used for the Fourier transform.	69

4.3.5	The Fourier transform of the EXAFS functions shown in figure 4.3.4. The dashed line represent the window function placed around the first nearest neighbour.	69
4.3.6i	The EXAFS function $\chi(k)$ weighted by k^3 for the sodium oxalate-formed oxide. The crosses represent individual data points; the continuous line is the cubic spline fit used for the Fourier transform.	72
4.3.6ii	The Fourier transform of the EXAFS function shown in figure 4.3.6i.	72
4.3.7i	The EXAFS function $\chi(k)$ weighted by k^3 for the sodium borate-formed oxide. The crosses represent individual data points; the continuous line is the cubic spline fit used for the Fourier transform.	73
4.3.7ii	The Fourier transform of the EXAFS function shown in figure 4.3.7i.	73
4.3.8i	The EXAFS function $\chi(k)$ weighted by k^3 for the chromic acid-formed oxide. The crosses represent individual data points; the continuous line is the cubic spline fit used for the Fourier transform.	73
4.3.8ii	The Fourier transform of the EXAFS function shown in figure 4.3.8i.	73
4.3.9i	The EXAFS function $\chi(k)$ weighted by k^3 for the phosphoric acid-formed oxide. The crosses represent individual data points; the continuous line is the cubic spline fit used for the Fourier transform.	73

4.3.9ii	The Fourier transform of the EXAFS function shown in figure 4.3.9i.	73
4.3.10i	The EXAFS function $\chi(k)$ weighted by k^3 for the sodium tartrate-formed oxide after immersion in water at 85°C for 30 minutes. The crosses represent individual data points; the continuous line is the cubic spline fit used for the Fourier transform of the EXAFS function.	74
4.3.10ii	The Fourier transform of the EXAFS function shown in figure 4.3.10i.	74
4.3.11i	The EXAFS function $\chi(k)$ weighted by k^3 for the sodium oxalate-formed oxide after immersion in water at 85C for 30 minutes. The crosses represent individual data points; the continuous line is the cubic spline fit used for the Fourier transform.	75
4.3.11ii	The Fourier transform of the EXAFS function shown in figure 4.3.11i.	75
4.3.12i	The EXAFS function $\chi(k)$ weighted by k^3 for the sodium borate-formed oxide film after immersion in water at 85C for 30 minutes. The crosses represent the individual data points; the continuous line is the cubic spline fit used for the Fourier transform.	75
4.3.12ii	The Fourier transform of the EXAFS function shown in figure 4.3.12i.	75
4.3.13i	The EXAFS function $\chi(k)$ weighted by k^3 for the chromic acid-formed oxide after immersion in water at 85C for 4 hours. The crosses represent individual data points; the continuous line is the cubic spline fit used for the Fourier transform.	76

4.3.13ii	The Fourier transform of the EXAFs function shown in figure 4.3.13i.	76
4.3.14i	The EXAFS function $\chi(k)$ weighted by k^3 for the phosphoric acid formed oxide after immersion in water at 85°C for 4 hours. The crosses represent individual data points; the continuous line is the cubic spline fit used for the Fourier transform.	76
4.3.14ii	The Fourier transform of the EXAFS function shown in figure 4.3.14i.	76
5.3.1a	SEM image of a 50 nm uniform non-porous (barrier type) oxide formed anodically on pure aluminium in sodium tartrate, coated with 3 nm of platinum.	83
5.3.1b	SEM image and EDAX spectra for an oxide formed in sodium tartrate electrolyte. Note the occurrence of a silicon peak in the EDAX spectrum of the particle.	83
5.3.1c	SEM image of the same sodium tartrate-formed oxide (figure 5.3.1a) after hydration at 85°C for 30 minutes. The "Cornflake" structure has been revealed by a thin coating (3 nm) of platinum.	83
5.3.1d	Schematic representation of the oxy-hydroxide morphology (after Venables et. al. 1980).	83
5.3.2a	SEM image of a 50 nm uniform non-porous type oxide formed anodically on pure aluminium in sodium oxalate, coated with 3 nm of platinum.	84
5.3.2b	SEM image of the same sodium oxalate-formed oxide (figure 5.3.2a) after hydration at 85°C for 30 minutes. The "Cornflake" structure has been revealed by a thin coating (3 nm) of platinum.	84

5.3.3a	SEM image of a 50 nm uniform non-porous type oxide formed anodically on pure aluminium in sodium borate, coated with 3 nm of platinum.	85
5.3.3b	SEM image of the same sodium borate-formed oxide (figure 5.3.3a), after hydration at 85°C for 30 minutes. The "Cornflake" structure has been revealed by a thin coating (3 nm) of platinum.	85
5.3.4a	SEM image of 100 nm layer anodically formed on pure aluminium in phosphoric acid. The cellular, porous structure has been revealed by a thin (3 nm) coating of platinum.	85
5.3.4b	SEM image of the same phosphoric acid-formed oxide (Figure 5.3.4a) after hydration at 85°C for 4 hours. The "Cornflake" structure has been revealed by a thin coating (3 nm) of platinum.	85
5.3.5a	SEM image of oxide layers anodically formed on pure aluminium in chromic acid. The porous structure has been revealed by a thin (3 nm) coating of platinum. The hillocks of oxide have been revealed by tilting the specimen 40° away from normal incidence. Note the occurrence of siliceous impurity particles on many of the hillocks.	86
5.3.5b	SEM image of the same chromic acid formed oxide (Figure 5.3.5a) after hydration at 85°C for 4 hours. The "Cornflake" structure has been revealed by a thin coating (3 nm) of platinum.	86
6.2.1a	Plot of the average number of oxygen neighbours of aluminium versus the average Al-O bondlength for aluminium oxide, assuming ionic bonding.	93
6.2.1b	The expected relationship between the distribution states of octahedral (AlO ₆) and tetrahedral (AlO ₄) bond configurations and average Al-O bondlength, for aluminium oxide, assuming ionic bonding.	93

- 6.2.2 The proposed model for amorphous alumina:- 99
- (a) the Al_4O_6 dimer suggested by Wilsdorf (1951). The large circles represent O^{2-} ions and smaller circles are Al^{3+} ions (the relative sizes of the O^{2-} ions and Al^{3+} ions are such that the O^{2-} ions are in close contact but they are separated in the diagram for clarity of presentation);
- (b) part of a three-dimensional sheet of edge-sharing Al_4O_6 octahedra;
- (c) the three-dimensional structure composed of stacked sheets of octahedra. The Roman letters indicate the close packing of layers of O^{2-} ions and the Greek letters indicate Al^{3+} in tetrahedral (β) and octahedral (γ) interstitial sites. Note the occurrence of four O^{2-} ions bonded to each β -type Al^{3+} ion and six O^{2-} ions around each γ -type Al^{3+} ion.
- 6.2.3 Shows a three dimensional representation in several 99 different perspectives using a more realistic ratio of O^{2-} and Al^{3+} ionic radii for the proposed model for amorphous alumina. On the left-hand side the Al_4O_6 dimer suggested by Wilsdorf (1951) and on the right hand side a "unit cell", composed of parts of three edge-sharing octahedra; note the omission of two-thirds of the Al^{3+} ions from "octahedral" sites to achieve stoichiometry.
- 6.2.4 Basal phase projections of the proposed sheet 100 structure. Large circles represent O^{2-} ions and small circles are Al^{3+} ions. The solid lines represent Al-O bonds. Al^{3+} ion vacancies are introduced to achieve the stoichiometric composition of Al_2O_3 :-

(a) the Wilsdorf octahedron Al_4O_6 ;
(b) a "unit cell", denoted by the dotted lines, composed of parts of three edge-sharing octahedra; note the omission of two-thirds of the Al^{3+} ions from "octahedra" sites to achieve stoichiometry;

(c) a sheet of three "unit cells" with the omission of $5/9$ of the Al^{3+} from "octahedral" sites and $1/9$ of Al^{3+} from "tetrahedral" sites to achieve stoichiometry.

(d) a sheet of five "unit cells" with the omission of $9/15$ of the Al^{3+} ions from "octahedral" sites and $1/15$ from "tetrahedral" sites; this structure is stoichiometric and the tetrahedral sites are occupied in the ratio 7:3.

6.3.1 (a) The electron yield EXAFS spectrum for the oxide film prepared in phosphoric acid appears to have a second peak at 2149 eV, corresponding to the phosphorus K-absorption edge; 104

(b) The electron yield EXAFS spectrum for the same oxide film formed in phosphoric acid after hydration for 4 hours at 85°C.

6.5.1 (a) The electron yield EXAFS spectrum for a 50 nm sodium tartrate-formed oxide on pure aluminium, appears to have a second peak at 1840 eV, corresponding to the silicon K-absorption edge; 106

(b) the electron yield EXAFS spectrum for the same film after hydration for 15 minutes at 85°C. Noting the disappearance of the silicon K-absorption edge.

CHAPTER 1

GENERAL INTRODUCTION

1.1. Introduction

Aluminium oxide (Al_2O_3) films formed by anodic oxidation of pure aluminium in aqueous electrolytes are of great interest in many technological applications. For example, adhesive bonding of structural components fabricated from aluminium alloys is now used extensively in the aerospace industry (see for example Venables et al, 1979). Aluminium is also used in the construction of chemical reactors and water desalination plants, in the fabrication of integrated circuits, and in the construction of mirrors for solar collectors. In all these applications the structure of the oxide layer and its reaction with water are critical for reliable performance.

When aluminium is anodized in certain electrolytes, an oxide film, consisting mainly of amorphous alumina, is formed on the surface. The nature of the film depends on several factors, the most important of which are the nature of the electrolyte used in forming the film, the applied voltage, the current density, and the time of anodizing. When aluminium is anodized in neutral electrolytes, such as neutralised tartrates, carbonates and phosphates, a thin film is formed, the thickness of which is proportional to the forming voltage. This is generally referred to as a barrier layer. The relation between the film thickness and the applied voltage has been investigated by many research workers, and is generally accepted as 1.4 nm V^{-1} , (see for example, Hunter and Fowle, 1954).

When aluminium is anodized in more aggressive electrolytes, such as 5-20% phosphoric or sulphuric acid, the resulting anodic oxide has a porous structure; also the film grows to a much greater thickness, depending on current density and time of anodizing. This anodic oxide film consists of two distinct regions; the inner region is a thin, dense barrier layer located at the oxide/metal interface, with a thickness of about 5-15nm, the outer region is a much thicker layer, which is very porous and is super-imposed on top of the barrier layer. The structure of the outer oxide region varies with the electrolyte used and the anodizing voltage, see for example, Thompson and Wood, 1981. Our interest in the structure of these types of oxide films arises from its importance in the epoxy-resin bonding of aluminium engineering structures. The strength and chemical stability of these oxides, which depend on the surface preparation, are of prime importance in determining the strength of the bond. Hydration of the aluminium oxide to an oxy-hydroxide, by exposure to water, is a major cause of engineering failure, because the oxy-hydroxide is mechanically weaker. A knowledge of the molecular structure of such films should be an important step in reaching an understanding of the structural chemistry of the anodic oxide. This should lead to a better understanding of the effect of hydration and crystallisation on mechanical stability.

1.2. Structure and Composition of anodic aluminium oxide

1.2.1. Review of earlier work

The extensive earlier studies of the structure and composition of aluminium oxide formed during the anodic oxidation of aluminium are

When aluminium is anodized in more aggressive electrolytes, such as 5-20% phosphoric or sulphuric acid, the resulting anodic oxide has a porous structure; also the film grows to a much greater thickness, depending on current density and time of anodizing. This anodic oxide film consists of two distinct regions; the inner region is a thin, dense barrier layer located at the oxide/metal interface, with a thickness of about 5-15nm, the outer region is a much thicker layer, which is very porous and is super-imposed on top of the barrier layer. The structure of the outer oxide region varies with the electrolyte used and the anodizing voltage, see for example, Thompson and Wood, 1981. Our interest in the structure of these types of oxide films arises from its importance in the epoxy-resin bonding of aluminium engineering structures. The strength and chemical stability of these oxides, which depend on the surface preparation, are of prime importance in determining the strength of the bond. Hydration of the aluminium oxide to an oxy-hydroxide, by exposure to water, is a major cause of engineering failure, because the oxy-hydroxide is mechanically weaker. A knowledge of the molecular structure of such films should be an important step in reaching an understanding of the structural chemistry of the anodic oxide. This should lead to a better understanding of the effect of hydration and crystallisation on mechanical stability.

1.2. Structure and Composition of anodic aluminium oxide

1.2.1. Review of earlier work

The extensive earlier studies of the structure and composition of aluminium oxide formed during the anodic oxidation of aluminium are

reviewed in this section. These studies have been carried out using the different techniques of electron diffraction, electron microscopy, optical microscopy, X-ray diffraction, infra-red spectroscopy, X-ray photoelectron spectroscopy, radio-active tracer techniques, extended X-ray absorption fine structure spectroscopy (EXAFS) and many other analytical methods. Notwithstanding the very large amount of such work, there is still no precise agreement about the structure or composition of the oxide films. One of the earliest studies, by Burgers, Claasson and Zernicke (1932), was on aluminium oxide layers formed anodically on aluminium in a boiling solution of borate and boric acid at 400-500 V and low current density. Such films showed sharp X-ray diffraction patterns. These patterns were related to the characteristic crystalline structure of γ -alumina. In 1936, Belwe reported an investigation into the structure of a barrier oxide layer on aluminium using the technique of electron diffraction. He observed two sharp diffraction rings. Using a reflection electron diffraction technique he found a pattern of diffuse rings for thicker oxide films. Harrington and Nelson (1940), also using electron diffraction, examined thinner oxide films than those studied by Burgers et.al (1932) with X-ray diffraction. They observed only diffuse rings in the electron diffraction patterns. Hass and Kehler (1941), used an electron microscope to examine thin oxide films (20-40 nm thick), prepared on aluminium in an aqueous solution of an organic acid at 25°C. After it was detached from the substrate these films showed a structureless image. Also the electron diffraction pattern of the films showed broad rings which were interpreted as being related to γ -alumina. Taylor, Tucker and Edwards (1943) studied the structure of aluminium oxides produced by anodic oxidation in boric, oxalic,

phosphoric, chromic and sulphuric acid electrolyte solutions, using X-ray diffraction. They reported that these films had the structure of γ' -alumina. Brandenberger and Hafel (1948) investigated the structure of oxide layers formed anodically at low voltage (20 V), using X-ray diffraction. The X-ray diffraction pattern showed the characteristic structure of boehmite. This suggests that these very thin films are hydrated to some degree. The same authors studied thicker films prepared by anodizing treatments at higher voltages (\approx 600 volts). These showed a structure which appeared to be a mixture of γ - and γ' -alumina. They suggested that the mixture consisted of large developed crystals of γ and γ' Al_2O_3 . They also studied oxide films formed at a range of voltages between 50 and 200 volts. The structure of these films was shown to be a mixture of hydrated and crystalline γ - Al_2O_3 . Later, in 1949, Hass examined the structure of the film on aluminium anodized at constant voltages in the range 10-15 V in a tartaric acid electrolyte having a pH value equal to 5.5. Using electron microscopy he found that the film was structureless. The same films were also studied by electron diffraction, and showed diffuse rings which were related to an amorphous structure.

Wilsdorf (1951) also studied the structure of aluminium oxide films using transmission electron diffraction. These oxide films were grown by annealing aluminium in air at 400°C for 75 hours. They were then stripped from the aluminium substrate by immersion in a dilute mercuric chloride solution, washed, and mounted on a specimen holder and placed in a 40-60 kV electron beam diffraction camera. He found that the diffraction pattern consisted of two diffuse haloes. He attempted to explain this in terms of a possible model for the amorphous structure consisting of Al_4O_6 molecular units. Kerr

(1956), examined anodic aluminium oxide films formed at 50 volts in an ammonium borate solution which were then stripped from the metal substrate in chlorine at 200°C again using transmission electron diffraction. The diffraction patterns of these films also contained diffuse haloes, which therefore appear to be typically associated with amorphous alumina. The diffraction pattern also showed sharper rings, which could be identified as arising from γ -alumina. David and Walsh (1956), studying various anodic oxide films, found that the structure of these depended on whether the current used was a.c. or d.c. They showed that the process of formation of the oxide by the use of d.c. led to a crystalline γ -alumina, while in the case of the a.c. process the film was an amorphous oxide. Franklin (1957) reported electron microscope observations on the structure of oxide formed by the anodising of aluminium in an electrolyte at high voltage (500 V) at 20°C. He found that the film consisted of closely packed domes superposed on barrier oxide layer with a density of about 1.4×10^4 domes cm^{-2} . He suggested on the basis of his observations that although the barrier layer is uniform in thickness on a microscopic scale the thickness within the dome structure varies across the surface. Plumb (1958), examined thin barrier films formed by anodic oxidation in a phosphate electrolyte using a radioactive tracer technique based on P^{32} ; he showed that the oxide layer contained phosphorus which was distributed uniformly through the film. He also reported the probable composition of the film to be 96.5% Al_2O_3 and 3.5% P_2O_5 . Stirland and Bicknell (1959), studied the structure of non-porous anodic oxide films on aluminium formed in an aqueous mixture of boric acid and borax at room temperature, using a forming voltage of less than 100 volts for 5 minutes. They examined these films after they were stripped from the metal substrate, using

electron diffraction and electron microscopy. They found that these films contained more than one region; some areas in the film were truly amorphous, while other areas consisted of a mixture of amorphous and γ -alumina.

Bernard and Randall (1960) carried out spectrographic analysis of barrier layer films on aluminium, anodically oxidised in a borate electrolyte. They showed that the films contained a small amount (0.7%) of boron which had been incorporated in the film during the anodizing process. McMullen and Pryor (1961) studied the structure of an aluminium oxide anodically produced in neutralized ammonium tartrate of pH 7.2, using various voltages (40-100 V). The structure was studied by electron diffraction. They concluded that these oxide films gave diffraction patterns with characteristics related to γ -alumina when the films were examined at high electron acceleration voltage (100 kV). However, when the films were examined at lower accelerating voltage (50 kV) the diffraction pattern showed only two diffuse rings. Hoar and Yahalom (1963) used electron microscopy to study the development of pores in the oxide layer on aluminium substrates anodised at room temperature in 3% ammonium tartrate electrolyte at a forming voltage of 14.4 V, for short exposures (0.5 sec) and longer (10 minutes). They found the film contained no pores after 0.5 sec, while distinct pores were visible after anodizing for 10 minutes. Tajima, Baba and Mori (1964) studied the structure and composition of a thick anodic oxide film ($> 20 \mu\text{m}$) formed on aluminium in a non-aqueous system of boric acid/formamide. The chemical analysis of the film showed an appreciable amount of B_2O_3 to be present with an overall composition of 81.2 W % Al_2O_3 and 18.7 W %

B₂O₃. The density of this film measured by a picnometric method was found to be 3.565 g cm⁻³, which may be compared with that of γ-Al₂O₃ (3.99 g cm⁻³) and that of B₂O₃ (1.85 g cm⁻³).

Jones (1974) studied the local atomic arrangement of amorphous alumina formed by anodic oxidation in boric acid electrolyte, using electron diffraction. He obtained a reduced radial distribution and radial distribution curve which he interpreted in terms of a model for the structure consisting of 92% of the aluminium ions existing in a tetrahedral coordination state (AlO₄), with an Al-O separation of 0.175 nm; and the remaining 8% of the aluminium ions are in octahedral coordination states with Al-O separation of 0.185 nm. He also reported that the Al-Al separation distance was equal to 0.275 nm, and the O-O separation was 0.32 nm. Takahashi et.al. (1976) measured the X-ray diffraction radial distribution function for anodic amorphous alumina prepared using d.c. and pulsed voltages. They found that the films formed by both methods had a spinel-type structure, but the degree of octahedral coordination was greater in the coating obtained by pulse electrolysis. Popova (1979), using transmission electron diffraction, investigated the structure of thin films of amorphous alumina (≈ 50 nm thick), formed anodically in a borate electrolyte at 40 V and then stripped from the metal substrate in a solution of bromine in methyl alcohol at room temperature. He found a radial distribution which gave a Al-O bond length of 0.182 nm, which corresponds to a 100% tetrahedral coordination. Oka et al (1979) also studied the structure of amorphous anodic oxide films formed on aluminium in a sulphuric acid electrolyte, using both a.c. and d.c. polarising voltages. Their study, based on an analysis of the X-ray radial distribution function, showed that the aluminium ions were

coordinated with 4, 5 and 6 oxygen ions [AlO_4 , AlO_5 and AlO_6], and the average coordination number was 4.64 and 4.81 for a.c. and d.c. respectively. These results indicate that the $\text{AlO}_6/\text{AlO}_4$ ratio is 30/70 for the film formed in a.c. and 40/60 for the film prepared with d.c. They also reported that the chemical composition of both types of oxide was 86.1 wt% Al_2O_3 and 12.4 wt% SO_3 , with a density of 3.05 g cm^{-3} .

Thompson, Furneaux, Wood and Hutchings (1978), studied in detail the structure and composition of the pore structure in anodic oxide films prepared on an electro-polished aluminium surface at a constant voltage (150 V) in a phosphoric acid electrolyte with an anodizing time of 10 minutes. These films were investigated by scanning transmission electron microscopy (STEM) and with x-ray energy dispersive analysis (EDAX). They showed that the cell boundaries in the porous structure are composed of nearly pure Al_2O_3 , while the material within the cells contain some phosphorus which is incorporated during the anodizing process. Later, in 1980, Alvey, Wood and Thompson, studying the mechanical properties of porous oxide films having a thickness of 15 μm , formed in various electrolyte solutions (sulphuric, phosphoric, oxalic and chromic acids), under a wide range of anodizing conditions found that anions are incorporated in the oxide from the various electrolytes in amounts of 11.1 wt% SO_4^{2-} , 7.6 wt% PO_4^{2-} , 2.4 wt% $(\text{COO})^{2-}$ and < 0.1 wt% CrO_4^{2-} respectively. Konno et al (1980a) investigated the composition of the barrier-type anodic oxide films on aluminium in borate and phosphate solutions of pH 7.4 at 20°C at a constant voltage of 50 volts. These oxides were compact and hard, with a thickness of about 76 nm. Using X-ray photoelectron spectroscopy (XPS) they were able to detect Al^{3+} ,

O^{2-} , B^{3+} and Al^{3+} , O^{2-} , P^{3+} ions in the films. Further, they reported that the film formed in neutral borate solution consisted of two parts: an outer part (depth 0-40 nm) having an average composition of $AlO_{1.36}(OH)_{0.28}(BO_2)_{0.14}$ and an inner part (depth 40-76 nm) with an average composition of $AlO_{1.5}(B_2O_3)_{0.027}$. Thus the outer part was slightly hydrated. Overall the film had an average content of 5.8% B_2O_3 . The film formed in neutral phosphate solution consisted of three parts: an outer part (~ depth 5-15 nm) having a composition of $AlO_{1.09}(OH)_{0.74}(PO_4)_{0.025}$; a middle part (~ depth 20-45 nm) with composition of $AlO_{1.463}(PO_4)_{0.025}$; and an inner part (~ depth 60-75 nm) showing only pure Al_2O_3 . Again, the outer part was hydrated. The film contained 11.7 wt% PO_4^{2-} overall.

1.2.2. Summary of the review

The main conclusions that can be drawn from this review are summarized as follows:

- (i) There is some disagreement concerning the structure of the film. Some workers have reported observations that show that the anodic oxide films are composed of amorphous alumina, while others have found a crystalline phase of either γ -alumina or what has been described as γ' - Al_2O_3 . From these various results it can be concluded that the structure of the oxide films depends on the forming conditions. There have been attempts to interpret the structure of the amorphous alumina in terms a disordered spinel structure. The ratio of tetrahedral to octahedral coordination (AlO_4/AlO_6) within this structure also appears to be strongly dependent on the forming conditions.

(ii) The morphology of the films is also dependent on both the electrolyte and the electrochemical conditions. A porous oxide is developed when aluminium is anodized in slightly acidic electrolytes, whilst more compact films (non-porous barrier layer oxides) are found with neutralized or slightly alkaline electrolytes ($\text{pH} \approx 7.2$).

(iii) Analyses of the composition of the films have shown that anions from the electrolyte can be included in the oxide. The amount of included electrolyte ions depends on the electrolyte used and also on the electrolytic forming conditions. There is some uncertainty about the form in which the anions are incorporated.

1.3. The behaviour of anodic aluminium oxide films in water

The anodic oxide, formed on aluminium by anodic polarization in an aqueous electrolyte, has a composition of primarily Al_2O_3 , with some electrolyte anions incorporated in it. Often the films have an amorphous structure. The XPS studies reported by Konno et. al. (1980a) showed a small amount of water incorporated in the outer layers. It is commonly found that the anodic oxide converts to an oxy-hydroxide when it is immersed in hot water. This hydration has been studied by many research workers who have shown that the rate of hydration depends on the type of oxide layer (uniform non-porous or porous layer), and the electrolyte used to form the oxide.

Hart (1954) used electron diffraction to investigate the hydration of anodic films, which had been formed in ammonium borate solution on aluminium substrates (99.99% purity) which were then

immersed in boiling water. The diffraction pattern of these hydrated films showed sharp rings which could be related to the boehmite (Al-OH) structure. As a result of studying the rate of formation of the boehmite he concluded that the hydrated oxide grew as a result of the migration of Al^{3+} from the aluminium substrate through the oxide film and then reaction of these ions with the water, rather than the hydration of the pre-formed oxide. He also made an attempt to hydrate the oxide films after they had been stripped from the substrate by immersing just these in boiling water but was unable to detect any structural change.

Spooner (1956) investigated the hydration of anodised surfaces during the process of steam sealing at 115°C for 30 minutes for the case of porous films formed anodically on aluminium in sulphuric acid, again using an electron diffraction technique. He found that the diffraction patterns of both the films formed in-situ on the aluminium substrate and films which had been stripped from the aluminium substrates, showed sharp rings after reaction with the steam and these could be identified as those corresponding to the structure of boehmite. This observation indicated that conversion of the aluminium oxide to the oxy-hydroxide (boehmite) had occurred, which confirmed that, in this case, the process was the result of the hydration of the existing oxide and not a reaction of the water with the aluminium substrate.

Kerr (1956) studied the sealing of films formed in ammonium borate solution at a polarising voltage of 50 V (giving rise to a barrier layer of about 70 nm thick) in boiling water. By selected area electron diffraction, he showed that boehmite was formed only when aluminium was in contact with the film.

Hunter et al (1959), in a comprehensive study of the hydration of oxide films formed in different electrolytes, showed that there is an incubation period of about 3 minutes before hydration of the barrier-type films occurred in boiling water; after this period the entire film became converted to boehmite in about 15 minutes. Films prepared in a phosphoric acid electrolyte which were porous and thicker required a longer incubation period, about 15 minutes, and thereafter hydrated more slowly than the other films. They found that only about one-third of this oxide formed in phosphoric acid had hydrated after about 25 minutes, and that more than 50 minutes were required to give complete hydration. They interpreted this reduced rate of hydration to be a result of the phosphorus ions from the forming electrolyte being incorporated into the oxide. They also found that the rate of hydration of both types of film was highly dependent on the temperature of the water, being rapid in boiling water, and decreasing significantly as the water temperature decreased. Although the incorporation of phosphorus from the phosphoric acid electrolyte had a marked inhibiting effect on hydration, other anions such as those incorporated from sulphuric, chromic and oxalic acids had little effect.

Bernard and Randall (1961), also found an incubation period before hydration of barrier oxide films commenced, but this was lower than the period observed by Hunter et.al. For a borate-formed film immersed in boiling water the incubation time was 12 seconds, compared to 60 seconds for an oxide film formed in tartrate solution and 2 minutes for oxides prepared in a phosphoric acid electrolyte. They also measured the times for complete hydration of the various films and related these times to the initial film thickness. This resulted in an approximately logarithmic dependence of the rate of hydration on

film thickness for the first 30 minutes of hydration.

Konno et.al. (1980b), using XPS chemical analysis, studied the hydration of barrier layer oxides (about 70 nm thick) on aluminium anodised in a borate solution of pH 7.4 at 20°C. The hydration was carried out by immersion of the film for 3 days in distilled water. They found that after this period the OH⁻ content in the outer layer of the oxide film had increased by a factor of about 3 times that originally present (reported previously, Konno et.al. (1980a)). These authors also reported that the hydration was strongly inhibited by chromate ions in the solution because CrO₄²⁻ ions were detected on the oxide surface, possibly forming a monolayer which obstructed the penetration of the water into the oxide.

Venables et.al. (1980) have studied the effect of hot water on two types of aluminium oxide, one prepared by the immersion of aluminium in a commercially used electrolyte, the Forest Product Laboratory (FPL) and the other using the Boeing phosphoric acid process (PAA). The FPL electrolyte contained Na₂Cr₂O₇.H₂O, H₂SO₄ and H₂O in a ratio of 1:10:30 by weight. The aluminium surface to be anodised was immersed for 15 minutes in this solution at 60°C. This process forms thin oxide films (= 8 nm thick) on the surface. The other process (PAA), in which the aluminium surface is first treated in FPL solution and then anodised at constant voltage (10 volts), produces very thick, porous oxide films (about 100 nm thick). The surfaces after immersion in hot water were monitored using a high resolution SEM technique and optical ellipsometry. The SEM observations showed a "Cornflake" morphology after hydration for both types of oxide, which could be related to the growth of the oxyhydroxide i.e. boehmite crystallites. Ellipsometry measurements on the FPL type oxide indicated that there is an incubation time of about 2 minutes before the oxide starts to be

converted to oxy-hydroxide, but for the PAA-formed oxide that the incubation time was 15 minutes or greater.

El-Mashri, Forty, Freeman and Smith (1981), using a high-voltage high resolution electron microscope (HVREM), studied very thin barrier layer specimens of anodic alumina, approximately 6 nm thick, formed in neutralized sodium tartrate solution on high purity aluminium. The oxide film after stripping in mercuric chloride showed large areas which appeared to be truly amorphous with a few patches (50-100 nm in extent) in which "lattice fringes" could be observed. After hydration in water at 80°C for about 7 minutes the films showed significant structural changes which could be attributed to the early stages of hydration. The domains of "lattice fringes" had grown and a much greater proportion of the film had been apparently converted to an oxy-hydroxide. This work is described in greater detail in Appendix II.

Davis et.al (1982), using scanning electron microscopy, studied the morphological changes occurring in the porous oxide films, formed by anodising in phosphoric acid, and exposed to water vapour with 100% relative humidity at 50°C. They observed that it took 2 to 4 hours before the surface exhibited the distinctive "cornflake" structure, which as previously shown is related to the development of the boehmite structure.

1.4. The aim of the work reported in this thesis

From the previous review in sections 1.2 and 1.3 it is evident that the anodically formed oxides and the products of their hydration are often amorphous in character. The amorphous structure may well be

related to the structure of γ -alumina but there has been no serious attempt hitherto to study the amorphous structure in detail. The main objective of the work presented in this thesis is to study the possibility of using extended x-ray absorption fine structure (EXAFS) to examine the molecular structure of various types of oxide film, formed anodically on pure aluminium sheets in a wide range of anodizing treatments. The EXAFS yields information about interatomic distances and the coordination of atoms in a solid and therefore should throw considerable light on the structure of these oxide films. By using the electron yield from the oxidised surface to detect the EXAFS a degree of surface sensitivity can be achieved as will be discussed in the next chapter, and this makes the electron yield EXAFS particularly useful as a method of studying thin oxide films, and the work described in the following chapters is intended to demonstrate this.

The structural changes in the oxide films following their hydration in hot water are very important for a better understanding of the structural factors which affect the usefulness of anodising treatments in practical applications such as corrosion protection and adhesive bonding. Consequently, a further aim of the work is to attempt to follow the structural changes occurring as a result of hydration and to relate these to the initial structure of the oxide layers. In addition to the EXAFS measurements, a high resolution scanning electron microscopy technique is developed to observe the morphological changes of the films following their hydration. This is expected to be particularly useful as a method of direct observation to confirm that hydration of the films has occurred. In this way, it should be possible to relate changes of internal atomic arrangements

in the anodic oxide films with the hydration process and hence obtain insight into the mechanism by which the transformation to boehmite occurs.

1.5. Plan of thesis

The thesis is divided into six chapters and three appendices: Chapter 2 - gives an account of the theory of EXAFS and the method by which accurate bond lengths can be obtained from the EXAFS data. This chapter also describes the modes in which the EXAFS data can be obtained and leads to the conclusion that the measurement of the yield of electrons emitted from the oxide films during X-ray absorption in the vicinity of the Al K-edge should be the most useful for the present purpose.

Chapter 3 - describes the experimental arrangement and the experimental procedure used for measuring the total electron yield EXAFS.

Chapter 4 - describes the method of preparation of various oxide films formed by anodic oxidation of pure aluminium, using different electrolytes. Also an account is given of the procedure by which the EXAFS spectra for the oxide are analysed and Al-O bond lengths representative of the structure can be obtained. This chapter also describes the hydration treatment of the various anodic oxide films and presents the EXAFS results for these.

Chapter 5 - gives a brief description of the use of a transmission electron microscope (TEM) with a scanning attachment (i.e. TEM STEM) to provide high resolution scanning electron microscope (SEM) images and the use of this to examine the micromorphological structure of the

various oxides and the hydrated phases. A method of surface decoration with a thin deposit of platinum to ensure good contrast and to reduce the surface charging of the oxide is described and the usefulness of this is demonstrated by observations made on the various oxides.

Chapter 6 - discusses the structure of the anodic oxide films and the hydrated films in the light of the EXAFS results and the SEM observations described in the preceding chapters. The kinetics of the hydration process as revealed by the EXAFS and SEM results are also discussed and this leads to important ideas concerning the role of impurities incorporated in the oxide films.

Appendix I - gives an account of the use of electron energy loss measurements to provide structural information similar to that obtained with EXAFS. The extended fine structure in the energy loss spectra (EXELES) in the vicinity of the oxygen K-absorption edge has been recorded for an anodic oxide film formed in sodium tartrate solution using a TEM microscope fitted with an electron energy loss spectrometer, and this has been used to obtain Al-O bond lengths which compare closely with those derived from conventional EXAFS.

Appendix II - describes high resolution electron microscope observations of the structure of very thin amorphous alumina films formed by anodic oxidation in sodium tartrate and also of these films after hydration.

Appendix III - develops a mathematical model advanced by Jones and Woodruff (1981) by which the surface sensitivity of the total electron yield in the soft X-ray region (i.e. at the Al K-edge) can be discussed.

REFERENCES

1. Alvey, C.E., Wood, G.C. and Thompson, G.E., (1980), Proceedings of Interfinish 80, 275.
2. Belwe, E., (1936), Z. Phys., 100, 192.
3. Bernard, W.J. and Randall, J.J., (1961), J. Electrochem. Soc., 108, 822.
4. Brandenberger, E. and Halef, R., (1948) Helv. Chim. Act., 31, 1168
5. Burgers, W.G., Claassen, A. and Zernicke, J., (1932), Z. Phys., 74, 592.
6. David, I. and Walsh, D., (1956), Trans. Faraday Soc., 52, 1642.
7. Davis, G.D., Sun, T.S., Ahearn, J.S. and Venables, J.D., (1982) J. Material Sci. 17, 1807.
8. El-Mashri, S.M., Forty, A.J., Freeman, L.A. and Smith, D.J. (1981) Inst. Phys. Conf. Ser. No. 61, 395.
9. Franklin, R.W., (1957), Nature, 180, 470.
10. Hanada, T., Aikawa, T. and Soga, N., (1982), J. Non-Crystalline Solids, 50, 397.
11. Harrington, R.A. and Nelson, H.r., (1940), Trans. Amer. Inst. Mining. Eng. Met. Eng. Div. Tech., 137, 128.
12. Hart, R.K., (1954) Trans. Faraday Soc., 50, 269.
13. Hass, G. and Kehler, H. (1941), Koll. Z., 95, 26.
14. Hass, G., (1949), J. Opt. Soc. Amer., 29, 532.
15. Hoar, T.P. and Yahalom, J., (1963), J. Electrochem. Soc. 101, 53.
16. Hunter, M.S. and Fowle, P., (1954), J. Electrochem. Soc. 101, 53.
17. Hunter, M.S., Towner, P.F. and Robinson, D.L., (1959), Amr. Electro-plat. Soc., Techn. proc., 220.

18. Jones, A.M., (1974), Texas Christian University, Ph.D. Thesis.
19. Kerr, I.S., (1956), *Acta. Cryst.*, 9, 879.
20. Kerr, I.S., (1956), *Proc. Phys. Soc.* 69, 1055.
21. Konno, H., Kabayashi, S., Fujimoto, K., Takahoshi, H. and Nagayama, M., (1980a), *Electrochim. acta*, 25, 1667.
22. Konno, H., Kabayashi, S., Takahashi, H. and Nagayama, M., (1980b) *Hakkaido Kogakubu Kenkyu Kokoku*, 102, 103.
23. McMullen, J.J. and Pryor, M.J., (1961). 1st International Congress on Metallic Corrosion, London.
24. Oka, Y., Takahashi, T., Okada, K. and Iwai, S., (1979), *J. Non-Cryst. Solids*, 30, 349.
25. Plumb, R. C., (1958), *J. Electrochem. Soc.*, 105, 498.
26. Popova, I. A., (1979), *Inorg. Mater. Consultants, Bur, Transl.*, 14, 1503.
27. Spooner, R. C., (1956), *Nature*, 178, 1113.
28. Stirland, D.J. and Bicknell, R.W., (1959), *J. Electrochem. Soc.*, 106, 481.
29. Tajima, S., Baba, N. and Mori, T., (1964), *Electrochim. acta*. 9, 1509.
30. Takahashi, T., Nagano, T., Wada, K., Sazuki, Y., Tajai, H. and Kimura, J., (1976), *Arumiyuma Kenkyu Kaishi*, 108, 53.
31. Taylor, C.S., Tucker, C.M. and Edwards, (1943), *J. Electrochem. Soc.*, 88, 325.
32. Thompson, G. E., Furneaux, R. C., Wood, G. C. and Hutchings, R., (1978), *J. Electrochem. Soc.*, 125, 1480.
33. Thompson, G.E., Wood, G. C., (1981), *Nature*, 290, 230.
34. Venables, J.D., McNamara, D.K., Chen, J.M., Sun, T.S. and Hopping, R.L., (1979) *Appl. Surf. Science*, 3, 88.

35. Venables, J.D., McNamara, D.K., Chen, J.M., Ditchek, B.M.,
Morgenthaler, T.I., Sun, T.S., and Hopping, R.L., (1980), 12th
National SAMPE technical conf., Oct. 7-9 (1980).
36. Wilsdorf, H.G.F. (1951), *Nature*, 168, 600.

CHAPTER 2

EXTENDED X-RAY ABSORPTION FINE STRUCTURE: THEORY AND MODES OF OBSERVATION

2.1 Introduction

Extended X-ray absorption fine structure (EXAFS) appears as oscillations of the absorption of X-rays on the high energy side of characteristic X-ray absorption edges, and is observed in nearly all forms of matter, (except monatomic gases). The fine structure can extend to several hundreds of electron volts above the edge, as illustrated schematically in figure 2.1. The EXAFS oscillations result from the interferences of the outgoing photoelectron wave, emitted during X-ray absorption, and those parts of the photoelectron wave which are backscattered from the neighbouring atoms surrounding the absorbing atom. This gives rise to a modulation of the X-ray absorption cross-section as a function of X-ray photon energy. As an interference effect the periodicities in the EXAFS are related to the distances between the absorbing atom and its neighbours. The amplitude of the EXAFS oscillations is related to the number of neighbours and hence to the coordination of the atom whose absorption edge is being studied with the surrounding structure. EXAFS is therefore potentially a very useful probe for studying the structure of materials. In recent years this has become increasingly important in the study of amorphous solid materials where conventional diffraction methods are not applicable (Teo and Joy, 1980).

2.2. Theory of EXAFS

The oscillatory part of the X-ray absorption cross-section, $\chi(k)$,

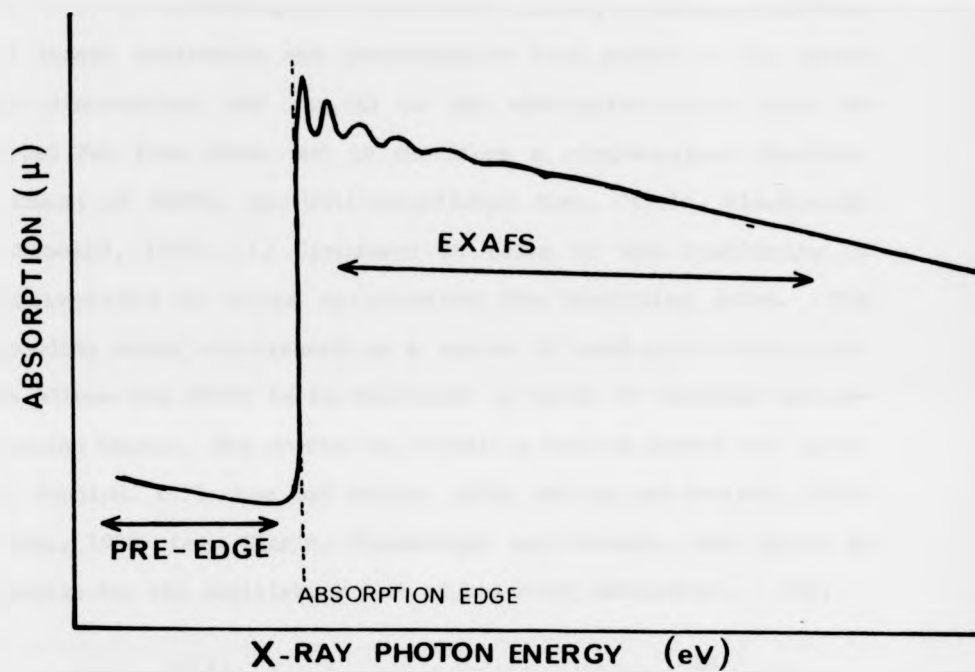


Figure 2.1: Schematic representation of EXAFS observed in the absorption as a function of photon energy, above the edge. The first 30-40 eV above the edge are the X-ray absorption near edge structure (XANES) and the oscillation modulation above that is the extended X-ray absorption fine structure (EXAFS).

is defined as:

$$\chi(k) = \frac{\mu(k) - \mu_0(k)}{\mu_0(k)} = \frac{\Delta\mu(k)}{\mu_0(k)} \quad (2.1)$$

where $\mu(k)$ is the absorption coefficient arising primarily from core level atomic excitation and photoemission from atoms in the system under observation, and $\mu_0(k)$ is the absorption which would be observed for free atoms and is therefore a single-valued function. The theory of EXAFS, now well-established (Lee, Citrin, Eisenberger and Kincaid, 1981), is discussed in terms of the scattering of photoelectrons by atoms surrounding the absorbing atom. The surrounding atoms are treated as a system of weak point-scatterers, which allows the EXAFS to be described in terms of standard single-scattering theory. The scattering formalism used by Sayers and Lytle, 1970; Schoich, 1973; Lee and Pendry, 1975; Ashley and Doniach, 1975; Pettifer, 1978; Lee, Citrin, Eisenberger and Kincaid, 1981 gives an expression for the oscillatory part of the x-ray absorption, $\chi(k)$:

$$\chi(k) = \frac{\Delta\mu(k)}{\mu_0(k)} = \sum_j \frac{N_j}{kR_j^2} \exp(-2\sigma_j^2 k^2) |F_j(\pi, k)| \exp(-2R_j/\lambda_j k) \times \sin[2kR_j + \psi(k)] \quad (2.2)$$

Where N_j is the number of atoms in the j^{th} shell around the absorbing atom at a distance R_j . The summation in $\chi(k)$ is over all shells of atoms. The term $|F_j(\pi, k)|$ is the amplitude of the back-scattered photoelectron wave from the j^{th} atom. This has phase, $\phi_j(k)$ given in terms of

$$|f_j(\pi, k)| = F_j(\pi, k) e^{-i\phi_j(k)} \quad (2.3)$$

$\psi(k)$ is the total phase shift experienced by the photoelectron wave in leaving the absorbing atom and being scattered by neighbouring atoms and can be expressed as:

$$\psi_j(k) = \phi_j(k) + 2\delta_1(k) \quad (2.4)$$

where $\delta_1(k)$ is the 1th phase shift due to the central atom (see Pettifer, 1978). It is important to realise that the atoms are not stationary; thus thermal vibration smears out the EXAFS oscillation, and this leads to a reduction in the intensity and an increase in the background, Beni and Platzmann, 1976. This and other atomic displacements due to disorder are represented in $\chi(k)$ by the additional term which takes the form of a Debye-Waller factor $[\exp(-2\sigma_j^2 k^2)]$, where σ_j^2 is the mean square relative displacement of absorber and scatterer. In an amorphous material, there is a greater spread of distances from the central atom to the atoms of a particular shell than in crystalline materials and this static disorder must also be included in σ_j^2 , Taylor 1984.

$$\text{i.e. } \sigma_j^2 \text{ amorphous (or glasses)} > \sigma_j^2 \text{ crystalline}$$

The term $\exp(-2R_j/\lambda_j k)$ allows for damping of the photoelectron wave by including the mean free path between inelastic collisions. (k) is the photoelectron wave vector defined by:

$$k = \frac{2m}{\hbar} (E-E_0)^{1/2} \quad (2.5)$$

where m is the mass of the electron, $\hbar = h/2\pi$, is the Planck's constant, E is the photon energy ($h\nu$); and E_0 is the photon energy close to the characteristic absorption edge, from which the kinetic energy of the photoelectrons is measured. The value of E_0 is not easy to identify in terms of photon energy precisely and it is usually taken to be an adjustable parameter within a few eV of the edge, Lee and Beni, 1977. The error in E_0 results in an apparent phase shift, which decreases with the electron momentum as $1/k$. In many applications E_0 is taken to be the energy at mid-step height, Rabe, 1978, but this can lead to considerable error in the determination of bond lengths.

2.3. The Analysis of EXAFS by the Fourier Transform Method

Although it is possible to obtain structural information by computing the fine structure for various models and then comparing the result with the experimental EXAFS data it is often more straightforward to analyse the data by considering the Fourier transform. The EXAFS function consists of a sum of damped sine-waves originating from successive coordination shells. The atomic structure in the material is therefore contained in the EXAFS function so that interatomic distances can be revealed by the Fourier transform of $\chi(k)$. Owing to the finite range of k over which the EXAFS can be observed due to the effect of both the Debye-Waller term and the decrease in the backscattering amplitude with k , the range over which the Fourier transform can be calculated is limited. This has the effect of broadening the peaks in the Fourier transform. Hence it is desirable to measure the EXAFS over as wide a range of energies as possible. Furthermore, the truncation of the data can give rise to

large termination effects which introduce unwanted structure in the Fourier transform. The truncation errors can be minimised by using a suitable window function (Gurman and Pendry, 1976). For this purpose a trigonometric Hanning window function is commonly used (equation 2.6). The form suggested by Lee and Beni (1977) is:

$$W(k) = \begin{cases} \{1 - \cos [(k - k_{\min})/D]\} & \text{for } k_{\min} > k > k_{\min} + D \\ 1 & \text{for } k_{\min} + D > k > k_{\max} + D \\ \{1 + \cos [k - (k_{\max} - D)]/D\} & \text{for } k_{\max} - D > k > k_{\max} \\ 0 & \text{elsewhere} \end{cases} \quad (2.6)$$

where D is chosen to be of the order $(k_{\max} - k_{\min})/10$. k_{\min} is usually chosen to correspond to a photon energy 20-50 eV above the absorption edge, depending on the type of near-edge fine structure; k_{\max} is determined by the limit of the available data. The window function should start and end at nodes of $\chi(k)$, as suggested by Lee and Beni (1977).

The EXAFS function $\chi(k)$ must also be multiplied by a term k^n which is a weighting factor included to compensate for the rapidly attenuating amplitude of the EXAFS components at larger k -values. The value of the exponent n depends on the atomic number of the back-scattering atoms. When the back-scattering is from the heavy elements, the amplitude is large and so only a small degree of weighting is needed, then $n=1$ is used; for light elements in which the back-scattering amplitude is small a larger degree of weighting is required, $n=3$. Teo and Lee (1979) suggested the power of the weighting factor (k^n) should be as follows:

$$\begin{aligned}
 n = 1 & \quad Z > 37 \\
 n = 2 & \quad Z > 19-36 \\
 n = 3 & \quad Z < 18
 \end{aligned}
 \tag{2.7}$$

In practice the choice of the weighting factor to be used must also depend on the quality of the EXAFS spectrum, that is the ratio of signal-to-noise in the EXAFS data. Therefore the power of the weighting factor should be considered to be a variable parameter taking the value 1, 2 or 3, in such a way as to keep the total amplitude of the data to be transformed more uniform throughout the range in k-space. Thus the Fourier transform to be used takes the form.

$$F(R) = \frac{1}{2\pi} \int_{k_{\min}}^{k_{\max}} W(k) \chi(k) k^n \exp(-2ikR) dk
 \tag{2.8}$$

The Fourier transform so obtained consists of a series of peaks with positions in R-space corresponding to interatomic distances but shifted towards the origin by an amount which is related to the phase shifts ψ_j in the EXAFS. By assuming that the phase shift $\psi_j(k)$ is linear over the range of k-space being considered and of the form:

$$\psi_j(k) = a_0 + a_1 k \quad \dots
 \tag{2.9}$$

then the argument of the sine term of equation (2.2) would be

$$[2kR_j + \psi_j(k)] = 2kR_j + a_0 + a_1 k = a_0 + 2 \left(\frac{a_1}{2} + R_j \right) k
 \tag{2.10}$$

Thus the peaks in the Fourier transform in R-space are shifted by an amount $a_1/2$. Although the phase shift can be calculated, and, indeed, values for many elements have been tabulated by Teo and Lee (1979), it is often preferable to determine the phase shift experimentally by comparing the EXAFS of the material under investigation with that obtained using a "model" compound, chosen to have the same chemical composition and whose structure is well known. This approach assumes that the phase shifts are transferable.

2.4. The Determination of Phase Shifts

As described previously, to determine the interatomic distance R_j , the phase shift ψ_j in the sine term in equation 2.2 must be determined or eliminated. The total phase shift for a pair of atoms (absorber and back-scatterer) can be calculated using the results of Teo and Lee (1979) or can be measured using a well characterised model compound. In this study we have chosen to determine the phase shift using a model compound in the form of crystalline α -alumina. This has the same backscattering pairs (Al-O) as the amorphous alumina films studied in this work. The structure of α -alumina is well known (WycCkoff, 1964). The Al^{3+} ions are octahedrally bonded to neighbouring O^{2-} ions with an average separation of 0.1915 nm.

There are two ways of obtaining the phase shift by the use of a model compound. In the first method the phase shift is determined directly by examining the Fourier transform of the EXAFS data from the model compound and comparing the peaks in this with the expected positions of the nearest neighbour shells. The difference determines $a_1/2$, which can then be used to correct the interatomic distances obtained from the Fourier transform of the EXAFS for the unknown structure.

A more reliable method is that described by Stohr et.al. (1980). This involves a comparison of the phases of individual sine terms ($\sin(2kR_j + \psi_j)$) for the model compound and the unknown. In order to make such a comparison the Fourier transform such as that described earlier (equation 2.8) is back-transformed using a suitable narrow window placed over a specific peak in real space. Thus, the back-transform

$$\chi'(k) = 1/k^n \int_{R_{\min}}^{R_{\max}} F(R) W(R) \exp(i2kR) dR \quad (2.11)$$

where R_{\min} and R_{\max} define the window, gives the sine component present in the EXAFS in k -space associated with the chosen peak in R -space. $\chi'(k)$ has a real and an imaginary part:

$$\chi'(k) = X(k) + iY(k) = A_j(k) \exp(i\delta_j(k)) \quad (2.12)$$

where $A_j(k)$ is the amplitude

$$A_j(k) = \frac{N_j}{R_j^2} f_j(\pi, k) \exp(-\sigma_j^2 k^2) \exp\left(\frac{\lambda(k)}{R_j}\right) \quad (2.13)$$

and $\delta_j(k)$ is the phase

$$\delta_j(k) = 2kR_j + \psi_j(k) \quad (2.14)$$

of the EXAFS due to the j th neighbour shell.

The amplitude can be computed by

$$A_j(k) = \sqrt{(X(k))^2 + (Y(k))^2} \quad (2.15)$$

Also the phase shift can be computed as:

$$\delta(k) = \cos^{-1} (X/A) \quad Y > 0 \quad (2.16a)$$

$$\delta(k) = -\cos^{-1} (X/A) \quad Y < 0 \quad (2.16b)$$

$$\delta(k) = 0 \quad X > 0, Y = 0 \quad (2.16c)$$

$$\delta(k) = \pi \quad X < 0, Y = 0 \quad (2.16d)$$

To determine the phase shift a comparison of a model compound and a material of unknown structure should be made.

Since the phases of the selected EXAFS components are given by

$$\delta_u(k) = (2kR_u + \psi_u(k)) \text{ for the unknown structure} \quad (2.17)$$

$$\text{and } \delta_m(k) = (2kR_m + \psi_m(k)) \text{ for the model compound} \quad (2.18)$$

the difference in the phases is

$$\delta_m(k) - \delta_u(k) = 2k(R_m - R_u) + (\psi_m(k) - \psi_u(k)) \quad (2.19)$$

If the assumption of transferability of phase shifts is correct then $\psi_m(k) = \psi_u(k)$ and hence

$$R_m - R_u = \Delta R = \left(\frac{\delta_m(k) - \delta_u(k)}{2k} \right) \quad (2.20)$$

The plot of $R_m(k) - R_u(k)$ versus k should therefore be a straight line passing through the origin of k . In practice this will not be the case because of uncertainty in the choice of E_0 , the position of the absorption edge, which therefore affects the zero in k -space for

the momentum of the photoelectrons. The analysis requires an adjustable parameter ΔE_0 so that

$$k' = (k^2 - 0.263 \Delta E_0)^{1/2} \quad (2.21)$$

and therefore

$$\delta_m(k') - \delta_u(k') = 2k' (R_m - R_u) + \frac{0.263 \Delta E_0 (R_m - R_u)}{(k'^2 + 0.263 \Delta E_0)^{1/2}} \quad (2.22)$$

ΔE_0 is then adjusted until the intercept of $\delta_m(k) - \delta_u(k)$ versus k' passes through the origin. If E_0 is carefully chosen, ΔE_0 should be within the range $-10 \text{ eV} \leq \Delta E_0 \leq +10 \text{ eV}$, corresponding to $-1.6 \text{ \AA}^{-1} \leq k' - k \leq 1.6 \text{ \AA}^{-1}$. Under these conditions the gradient gives the difference between the interatomic distances in the model compound and the unknown material structure.

2.5. The Derivation of Coordination Number from the EXAFS

The total amplitude function ($A_j(k)$) in the EXAFS data, given by equations (2.12) and (2.13), contains information about the coordination number (N_j) and the relative disorder (σ_j^2). This information can be extracted by using the measurements on the model compound and comparing the EXAFS from a single shell, after taking the Fourier transform and its back-transform, of the model in which N_j and σ_j are known, with the EXAFS from the same shell of the unknown material. This involves the use of the back Fourier transform, described in the previous section (equation 2.9), with a narrow window placed around a single peak in R-space. This gives the EXAFS contribution from a single shell of atoms for the model compound and the unknown structure. If both

materials have the same type of backscattering atoms and similar photoelectron mean free paths then the terms relating to these factors can be omitted in the ratio of the EXAFS amplitudes for the two materials (see Stohr et.al. 1980, and references therein). Therefore, the ratio of the amplitudes becomes:

$$\ln[A_m(k)/A_u(k)] = \ln \left[\frac{N_m}{N_u} \left(\frac{R_u}{R_m} \right)^2 \right] + 2 (\sigma_u^2 - \sigma_m^2) k^2 \quad (2.21)$$

and a plot of this versus k^2 should yield a straight line. The intercept of this straight line at $k=0$ should be the log ratio of N/R^2 for the two materials, and the slope should give the difference in σ . The accuracy of the amplitude measurement depends on the Gaussian shape of the peaks in the Fourier transform which, in turn, depends highly on the quality of the EXAFS data and also the range of the data in k -space. The absence of long range order in the material also causes broadening of the peaks in the Fourier transform. Furthermore the shape and position of the peaks in the Fourier transform are affected by the accuracy with which the smooth background (μ_0) is subtracted from the experimental EXAFS data. These factors all contribute to a large degree of uncertainty in the determination of the coordination number from the EXAFS. Thus, an alternative method for determining the coordination number, based on the theoretical ratio of the equilibrium interionic distances $R_O^u/R_O^m = (N^u/N^m)^{1/n-1}$, has been used in this work on alumina. As will be discussed in detail in chapter 6, this is permissible since the materials used are strongly ionic.

2.6. General considerations concerning the measurements of EXAFS

The technique of extended X-ray absorption fine structure (EXAFS)

has been widely employed in structural studies of solid materials. The application of the technique to the study of amorphous solids has proved to be particularly useful (see for example, Pettifer and McMillan 1977). It enables the study of short range, local order in such solids, which is not readily obtainable by conventional methods such as X-ray and electron diffraction. There are various methods or modes by means of which EXAFS can be monitored. These are described briefly below in order to consider their relative usefulness for the study of surface films in the present work.

2.6.1. Transmission EXAFS

This involves the transmission of X-rays through a thin specimen. The intensity of the X-ray beam is attenuated in its passage through the absorbing material according to the relation

$$I_t = I_0 \exp(-\mu t) \quad (2.22)$$

$$\text{or} \quad \mu t = \ln (I_0/I_t) \quad (2.23)$$

where μ is the linear absorption coefficient and t is the thickness of the sample. Experimentally, the beam intensity, I_0 and I_t , before and after the absorption, is measured by ionisation chambers, and $\ln(I_0/I_t)$ is plotted as a function of the incident X-ray energy. In early experiments of this kind (Lytle, 1966), a conventional X-ray generator was used as a source of X-rays, but nowadays the X-rays are usually provided by a synchrotron radiation source. This has the advantages of higher intensities over a continuum of energy.

The linear absorption coefficient (μ) can be calculated from standard data in tables in order to determine the optimum thickness needed to get maximum EXAFS signal-to-noise ratio, using the criterion suggested by Kincaid (1976)

$$t = \frac{1.2}{\mu} \quad (2.24)$$

where the absorption is measured close to the absorption edge under investigation. The linear absorption coefficient for a component can be determined using the additivity of the mass absorption coefficients $(\frac{\mu}{\rho})_i$, so that

$$\left(\frac{\mu}{\rho}\right)_i = \sum g_i \left(\frac{\mu}{\rho}\right)_i \quad (2.25)$$

where g_i is the mass fraction of atomic component i . The approximate values of $\left(\frac{\mu}{\rho}\right)_i$ in the wavelength (λ) range = 0.3 - 2.75 Å² can be found tabulated in International Tables for X-ray Crystallography, Vol. III, 1962. Outside the range $\lambda = 0.3 - 2.75$ Å the values of $(\frac{\mu}{\rho})_i$ are not readily found in tabulated form and therefore they are best obtained by calculation using the relation given by Bragg (1933) and Agarwal (1979)

$$\bar{\mu} = \begin{cases} c\lambda^3 Z^4 & \text{for } \lambda = \lambda_k \\ c'\lambda^3 Z^4 & \text{for } \lambda > \lambda_k \end{cases} \quad (2.26)$$

where $c = 1.92 \times 10^{-2}$ cm and $c' = 0.32 \times 10^{-2}$ cm, Z is the atomic number of the element and λ is the X-ray wavelength at the absorption edge. Therefore the mass absorption coefficient $(\frac{\mu}{\rho})_i$ is equal to

$$\left(\frac{\mu}{\rho}\right)_i = \bar{\mu} / (A/N) \quad (2.27)$$

where A is the atomic weight of the element and N is the Avogadro's number. For $\lambda = 7.95$ Å just above the aluminium K-edge, the linear

absorption coefficient of aluminium metal, obtained from the calculated mass absorption coefficient and the density of aluminium, is approximately $(1025) \text{ cm}^2 \text{ gm}^{-1}$. The optimum thickness is then found to be about $4.5 \text{ }\mu\text{m}$. Also, at the same value of λ , the mass absorption coefficients $(\frac{\mu}{\rho})_i$ of aluminium and oxygen are about $1025 \text{ cm}^2 \text{ gm}^{-1}$ and $245 \text{ cm}^2 \text{ gm}^{-1}$, respectively. The atomic weights of aluminium and oxygen are 27 and 16. Thus the mass absorption coefficient for Al_2O_3 (alumina) is obtained from

$$\left(\frac{\mu}{\rho}\right)_{\text{Al}_2\text{O}_3} = \frac{2}{5} \left(\frac{\mu}{\rho}\right)_{\text{Al}} + \frac{3}{5} \left(\frac{\mu}{\rho}\right)_{\text{O}} = \frac{2}{5} (1025) + \frac{3}{5} (245) = 557 \text{ cm}^2 \text{ g}^{-1} \quad (2.28)$$

Hence the linear absorption coefficient of Al_2O_3 is obtained by multiplying this by the density (ρ) of the alumina, which in the case of anodic alumina has been found to be between 1.1 and 2.2 g cm^{-3} (Simons et al., 1980). Therefore, the linear absorption coefficient at the Al K-edge has a maximum value of $(557 \times 2.2) = 1225 \text{ cm}^{-1}$. The optimum thickness of anodic alumina for transmission EXAFS is therefore about $10 \text{ }\mu\text{m}$. If we assume the density of the anodic alumina to be nearly the same as in γ -alumina, 3.5 gcm^{-3} , then the optimum thickness is reduced to about $6 \text{ }\mu\text{m}$.

In the case of the oxides studied in this work, formed by anodic oxidation of aluminium, the film thickness varies from about 5 to 150 nm ($0.005 - 0.15 \text{ }\mu\text{m}$). This is extremely thin compared with the optimum thickness of transmission EXAFS and hence the signal-to-noise in such spectra for stripped oxide films will be very low ($S/N = 10^{-4}$). Thus, the transmission method is unsuitable for the examination of very thin films, such as those formed by the anodisation of aluminium. There is a further problem in carrying out transmission EXAFS for such thin films arising from the damage caused by the intense X-ray beam. This will be less important in the case of

the X-ray fluorescence and electron yield modes of recording the EXAFS because in these cases the films are retained on their metal substrate which can absorb energy.

2.2.6. Fluorescence EXAFS

The excitation of a photoelectron leaves the absorbing atom with an empty core level. A higher shell electron fills the core hole and this is accompanied by emission of energy in the form of an electron (Auger emission) or an X-ray photon (Fluorescence), as shown schematically in figure 2.2.6. In this way energy conservation is maintained. In either case, the flux of Auger electrons or the fluorescence intensity is a measure of the absorption of the incident X-rays.

In the fluorescence detection mode the fluorescence intensity is measured by an array of scintillation detectors places around the sample (see, for example, the arrangement described by Phillips (1981); Hasnain et al. (1984). As in the case of the transmission mode, the initial intensity of the X-ray beam is measured by an ionization chamber. The fluorescence intensity is then normalized relative to the incident X-ray intensity. Care is necessary in choosing a suitable geometrical configuration of the detectors in order to avoid interference between the fluorescence signal and the incident beam (Jacklevic et al. 1977; Lee et al. 1981).

In a theoretical calculation, originally made by Wentzel (1927) the fluorescence yield, w_k , has been found to be

$$w_k(Z) = (1 + A/Z^4)^{-1} \quad (2.29)$$

where Z is the atomic number of the fluorescent atom and A is a

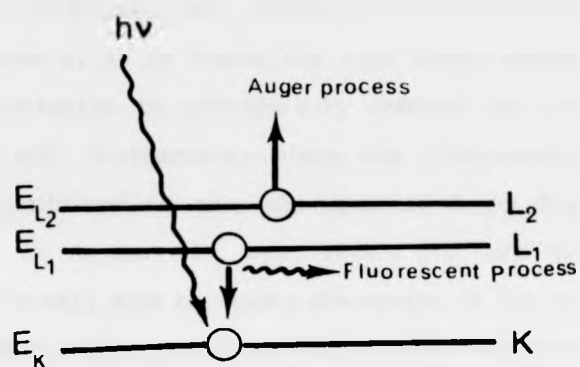


Figure 2.6.2: Schematic decay processes for core holes leading to X-ray fluorescence or Auger electron emission.

numerical constant. In a more detailed discussion of this result (see Dick and Lucas, 1970) for K-L shell transitions the appropriate values for A are $A = 1.19 \times 10^5$ for $Z < 10$, $A = 1.19 \times 10^6$ for $10 < Z < 18$ and $A = 1.27 \times 10^6$ for $Z > 18$.

The fluorescence mode is useful for EXAFS studies of materials in which the absorbing species are dispersed at low concentration throughout the sample, and, because of the strong dependence of w_k on atomic number Z, it is useful for high atomic number materials ($Z > 20$). The emission is considerably reduced for low atomic number materials and, furthermore, since the fluorescence detectors are normally positioned in air, the measured X-ray fluorescence yield, which will be in the soft X-ray region for such materials, is very small. There will also be strong absorption of the soft X-rays in the sample. These factors make the fluorescence mode unattractive for low Z materials, such as Al_2O_3 . In principle the fluorescence X-rays could be detected in a very high vacuum environment using a windowless detector. Even then the signal-to-noise ratio will be very small because of the low fluorescence yield and in practice long data accumulation times are needed to obtain high quality EXAFS spectra. This technique is therefore not ideal for the present work.

2.6.3. The electron yield EXAFS

This technique has been developed to measure the extended X-ray absorption fine structure for surface atomic arrangements (SEXAFS) and for the study of surface films, such as oxides on metals. There are two types of measurements, one in which the Auger electron yield is used and the other in which the total electron yield is used. The total electron yield is particularly suitable for determining the

structure of very thin films, i.e. 10-50 nm thick, composed of light elements having Z less than 20 because the sampling depth of the total yield is comparable with the film thickness. This is the thickness range for which the other modes of EXAFS such as the transmission mode are not suitable. It has been used by Stohr et al. (1979), for the study of oxide films on aluminium and silicon where the EXAFS in the vicinity of the oxygen K-edge makes the technique extremely surface sensitive. It is also the technique used extensively in the EXAFS studies discussed in this work.

The general concept of photoelectron spectroscopy is summarised in fig. 2.6.3 which shows a schematic representation of the photoelectron spectrum expected for a typical solid. There is a large secondary electron yield at low energies, arising from inelastic scattering of the characteristic photoelectron emission and the Auger electron emission. The photoelectrons and the Auger electrons occur at well-defined energies which depend on the electronic structure of the absorbing atoms in the solid. In the following sections the use of the Auger electrons in partial yield EXAFS and the larger flux of secondary electrons in total yield EXAFS will be discussed.

2.6.4. The Auger electron yield EXAFS

In the Auger electron emission mode only the elastic Auger electrons from the sample are collected. The photo-ionisation of the absorbing atom leaves an empty core hole in the K-shell, as shown schematically in figure 2.6.2. This can be filled by an L-shell electron and the excess energy is accounted for by the emission of a second electron from a higher shell. This Auger electron is usually emitted from a nearby L-shell. In such cases the Auger emission

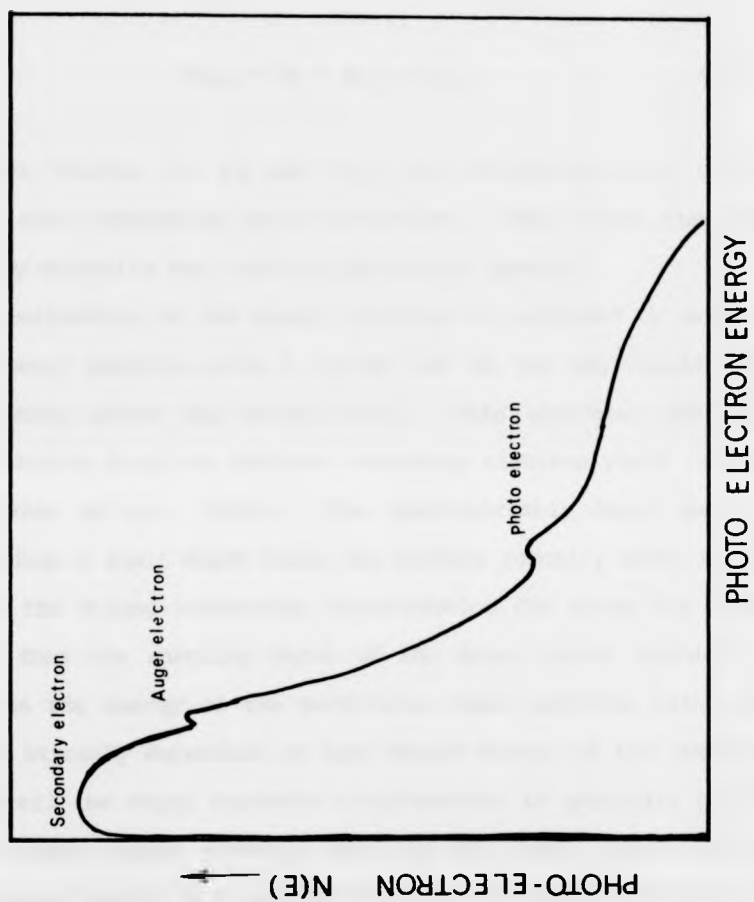


Figure 2.6.3: Schematic photoemission spectrum of electrons emitted from a surface as a function of photon energy.

process is designated KLL. The Auger electron is emitted into the vacuum with the remaining kinetic energy E_{kin} given by

$$E_{kin} = E_K - E_{L1} - E_{L23} \quad (2.30)$$

These three levels (K, L_1 and L_{23}) are characteristic of the particular atom undergoing photo-ionisation. This makes the Auger yield highly selective for a particular atomic species.

The collection of the Auger electrons is achieved by using an electron energy analyser with a window set at the particular Auger emission energy above the vacuum level. This separates the Auger electron emission from the dominant secondary electron yield (see for example, Stohr et al., 1980). The characteristic Auger emission originates from a small depth below the surface (usually about 1-2 nm) because of the strong scattering cross-section for those low energy electrons. Thus the sampling depth of the Auger yield technique is dependent on the energy of the particular Auger emission being used and is not strongly dependent on the atomic number of the absorbing atom. However, the Auger emission cross-section is generally greater for lower atomic number elements and thus the Auger yield mode for EXAFS is more useful for such materials. The Auger technique is particularly useful for studies of surface or near-surface structures. the technique is limited in usefulness for studies of films thicker than about 2 nm because the Auger emission is relatively small and the measurements require a sophisticated electron analyser. For thicker films it is more advantageous to use the total electron yield.

4.6.3ii. The total electron yield EXAFS

The total electron yield involves all electrons regardless of their kinetic energies emanating from the sample. All the elastically emitted Auger electrons, photo-electrons and inelastically scattered electrons are collected. However, as indicated in the previous section the inelastically scattered secondary electrons are dominant. The secondary ionisation by the more energetic Auger and photo-electrons can give rise to a cascade effect. This accounts for the very large broad peak in the low-energy part of the photoemission spectra shown in figure 2.6.3.

The technique of total electron yield was first used to measure X-ray absorption spectra by Lukirskii and Brylov (1964), then later by Gudate and Kunz (1972), who first used synchrotron radiation in such experiments. It was further developed by Stohr et al. (1980), who applied the total yield technique and also a partial yield method to study the oxidation of aluminium and silicon. Jones and Woodruff (1982), applied the total yield technique to detect the EXAFS for various anodised aluminium surfaces, using the Al K-edge, and obtained a measure of the surface sensitivity. They concluded that the method is useful for measurements of EXAFS for alumina films of thicknesses greater than about 50 nm. As shown in Appendix III the sampling depth of the total yield is strongly dependent on the atomic number of the absorbing atom. Thus, it is very suitable for the present work on anodic alumina films. The total yield technique is less appropriate for thinner films and higher atomic number elements.

2.7. Summary

In this study we have chosen to use the total electron yield detection technique because it provides a very convenient method for

monitoring EXAFS spectra for thin oxide films on aluminium, and gives good quality data. The technique has been used to measure the EXAFS for a large number of anodic alumina films formed under a wide range of anodizing treatments of pure aluminium. The method has also been used to measure the EXAFS for a similar set of films after hydration treatment in hot water. The experimental procedures and the method of data collection will be discussed in detail in the next chapter.

REFERENCES

1. Agarwal, B.K., (1979), X-ray Spectroscopy, (Springer-Verlag Berlin Heidelberg New York).
2. Ashley, C.A. and Doniach, S., (1975), Phys. Rev. B11, 1279.
3. Beni, G. and Platzmann, P.H., (1976), Phys. Rev., B14, 9514.
4. Bianconi, A. and Bachrach, R.Z., (1979), Phys. Rev. Lett, 42, 104.
5. Bragg, L. (1933), The Crystalline State, Vol. 1, (Bell and Sons Ltd.
London).
6. Brennan, S.M., (1982), Ph.D. Thesis, Stanford University, USA.
7. Citrin, P.H., Eisenberger, P. and Hewitt, R.C., (1978), Phys. Rev. Lett., 41, 309.
8. Dick, C.E. and Lucas, A.C., (1970), Phys. Rev. A, 580.
9. Gurman, S.J. and Pendry, J.B., (1976), Solid State Comm., 20, 287.
10. Gudate, W. and Kunz, C., (1972), Phys. Rev. Lett., 29, 169.
11. Hasnain, S.S., Quinn, P.D., Diakun, G.P., Wardell, E.M. and Garner, C.D., (1984), J. Phys. E: Sci. Inst., 17, 11.
12. Jaklevic, J., Kirby, J.A., Klein, M.P., Robertson, A.S., Brown, G. S., and Eisenberger, P., (1977), Solid State Comm., 23, 679.
13. Jones, R.G. and Woodruff, D.P., (1982), Surface Sci., 114, 83.
14. Kincaid, B., (1976), Ph.D. Thesis, Stanford University, USA.
15. Lee, P.A. and Beni, G., (1977), Phys. Rev., B15, 2862.
16. Lee, P.A. and Pendry, J.B., (1975), Phys. Rev., B11, 2795.
17. Lee, P.A., (1976), Phys. Rev. B13, 5261.
18. Lee, P.A., Citrin, P.H. and Eisenberger, P., (1981).
19. Lee, P.A., Citrin, P.H., Eisenberger, P. and Kincaid, B.M. (1981) Rev. Mod. Phys., 53, 769.

20. Lukirskii, A.P., and Brylov, I.A., (1964), Soviet Phys-Solid State, 6, 33.
21. Lytle, F.W., (1966), Advances in X-ray Analysis, 9, 398.
22. Norman, D., Brennan, S., Jaeger, R. and Stohr, J., (1981), Surf. Science, 105, 1297.
23. Pettifer, R.F. and McMillan, P.W., (1977), Phil. Mag. 35, 871.
24. Pettifer, R.F., (1979), 4th European Physical Society General Conf (Inst. Phys. London, 1979) 522.
25. Phillips, J.C., (1981), J. Phys. E: Sci. Inst., 14, 1425.
26. Rabe, P., (1978), Japanese J. of Applied Physics, 17, Supplement 17-2, 22.
27. Schaich, W., (1973), Phys. Rev., B8, 4078.
28. Schmidt, V.V., (1963), Bull. Acad. Sci., USSR Phys. Ser., 27, 392.
29. Sayers, D.E. and Lytle, F.W., (1970), Adv. in X-ray Analysis, 13, 248.
30. Simons, D.G., Crowe, C.R., Brown, M.D., De Jannette, H., Land, D.J and Brennan, J.G., (1980), J. Electrochem. Soc. 127, 2558.
31. Stohr, J., Johonsson, L.I., Brennan, S., Hecht, M. and Miller, J.N (1980), Phys. Rev. B22, 4052.
32. Stohr, J., (1980), Stanford Synchrotron Radiation Laboratory, Report 80/07, Stanford University, USA.
33. Taylor, J.M., (1984), Ph.D. Thesis, University of Warwick, UK.
34. Teo, B.K. and Lee, P.A., (1979), J. Amer. Chem. Soc., 101, 2815.
35. Teo, B.K. (1980), EXAFS Spectroscopy Techniques and Applic. ed. Teo, B.K. and Joy, D.G., (New York: Plenum).
36. Teo, B.K. and Joy, D.C. (editors), (1980), EXAFS Spectroscopy Techniques and Applications (New York: Plenum).

37. Via, G.H., Sinfelt, J.h. and Lytle, F.W., (1979), J. Chem. Phys. 71, 690.
38. Wentzel, G., (1927), Z. Physik, 43, 524.
39. Wyckoff, r.W.G., (1964), Crystal Structure, second edition (New York: Wiley).

CHAPTER 3

THE ELECTRON YIELD EXAFS INSTRUMENTATION AND MEASUREMENT

3.1. Introduction

This chapter contains a description of the experimental arrangement at the CNRS Orsay Laboratory where the work on electron yield EXAFS was carried out using the ACO storage ring. This includes a discussion of the arrangement of the source and monochromator and the facility for the electron yield EXAFS data collection. The monochromator was designed to provide soft X-rays in the region of 1000-2500 eV which embraces the aluminium K-edge. The procedure for normalization of the EXAFS data using the pre-edge background is also discussed. Finally, this chapter discusses the total electron yield sampling depth for aluminium films in terms of a mathematical model for the secondary electron emission. The sampling depth is also measured experimentally using a series of oxide films of various thicknesses.

3.2. Synchrotron radiation

Synchrotron radiation is used nowadays to provide ultra-violet and X-ray radiation for many experiments where high photon fluxes are required, and where a continuous spectrum of photon energies covering the spectral range of interest is needed. Synchrotron radiation sources are usually in the form of electron beam storage rings in which electrons are accelerated in a nearly circular orbit defined by high magnetic fields, usually in ultra-high vacuum to minimize the decay of the stored electron current. The energy spectrum of the radiation depends on the energy and the current of the circulating electrons stored in the ring.

Electron energies range from several mega-electron volts (MeV) as for example, in the case of the ACO source at Orsay (France), to several Giga-electron volts (GeV) in the SPEAR machine at Stanford University (USA) and the new SRS at the Daresbury Laboratory (UK). Such machines produce a continuous spectrum of radiation with photon fluxes of $10^7 - 10^{11}$ photons s^{-1} ev^{-1} $mrad^{-1}$. Depending on the electron energy and the radius of the orbit the photon spectrum has a cut-off wavelength at the high energy end; for example at ACO $\lambda_c = 38 \text{ \AA}$ and at the SRS $\lambda_c = 1.1 \text{ \AA}$. (for more details see the excellent review article on the properties of synchrotron radiation by Kunz, 1979).

During the last 20 years synchrotron radiation has become very useful in a great many fields of scientific research, using the entire spectral range from the far infra-red to soft and hard X-rays. The applications include studies in physics, chemistry, material science and biological science disciplines. Fig. 3.2.1 shows a schematic presentation of some of these applications of synchrotron radiation (see Forty 1979).

For EXAFS experiments, synchrotron radiation has many advantages over radiation from conventional X-ray tubes. The synchrotron radiation provides a more intense, continuous X-ray spectrum and is a stable source over the period of beam life-time. The life-time depends on the stability of the stored electron beam and the quality of the vacuum.

3.3. EXAFS experimental arrangements

The experimental arrangement used for making the electron yield EXAFS measurements to be described in later chapters is shown schematically in figure 3.3.1. Because measurements at the Al K-edge

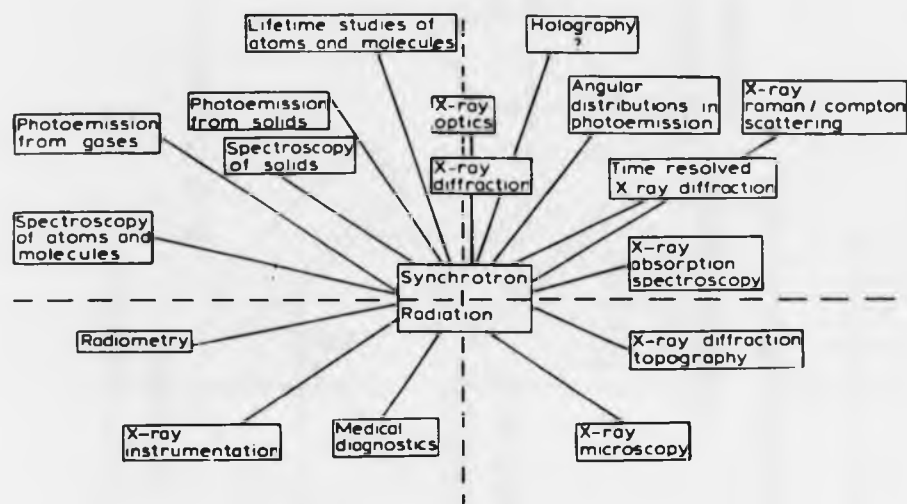


Figure 3.2.1: Shows a schematic presentation of some of the possible applications of synchrotron radiation (after Forty, 1979).

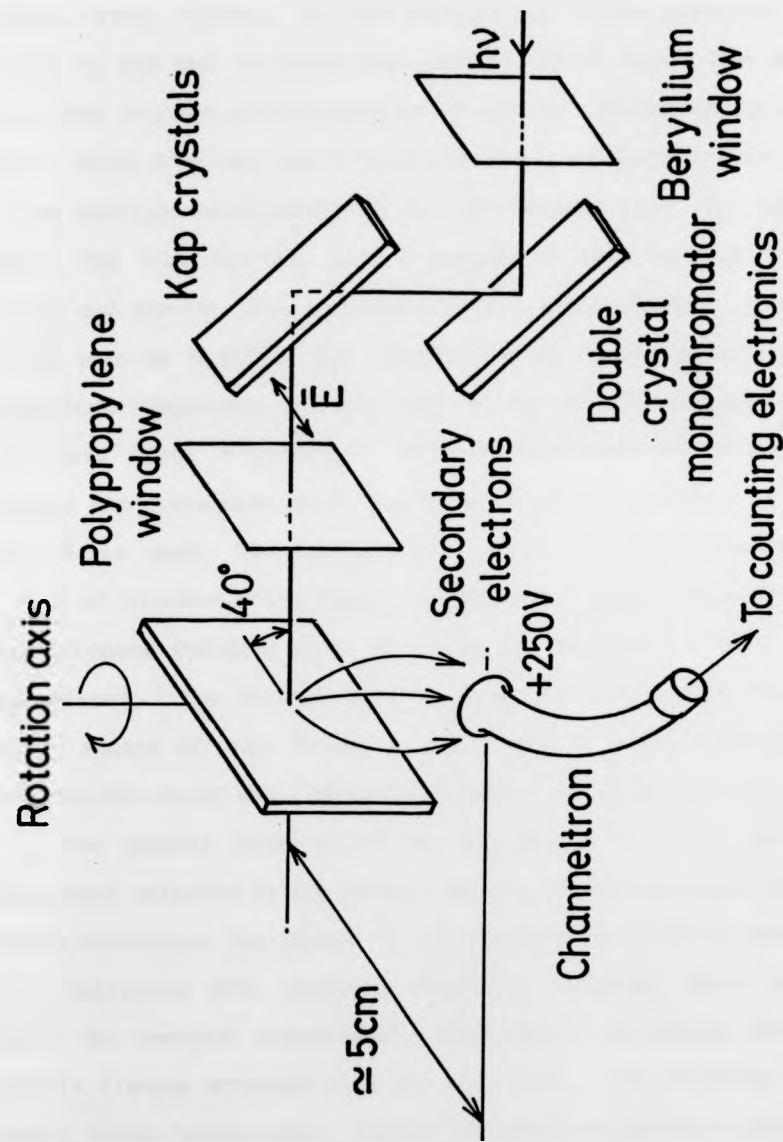


Figure 3.3.1: The experimental arrangement for recording electron yield EXAFS.

require soft X-rays the experiments were performed at the ACO storage ring at Laboratoire pour l'Utilisation du Rayonnement Electromagnetique (LURE), Orsay, France. In this machine the stored electron current is 100 mA at 450 MeV in ultra high vacuum (10^{-10} torr). The soft X-rays leave the storage ring tangentially and are collected by a toroidal mirror which focusses the X-ray beam onto a horizontal exit slit, (for a more detailed description of the ACO storage ring, see Guyon et al, 1976). The beam travels some 8 meters to pass through a beryllium window and thence into a double-crystal monochromator. The beryllium window acts as a filter for visible and UV light. In order to obtain sufficient dispersion of the soft X-rays the monochromator crystals must have large d -spacings. For the ACO soft X-ray monochromator organic KAP (potassium acid phthalide) crystals having a $2d$ -spacing of 26.63 Å are used. The crystals are 1.0 cm wide, and are able to accept 1 mrad of incident X-ray beam. Measurements made on the output of the monochromator indicate that typically 10^7 photons s^{-1} eV^{-1} $mrad^{-1}$ are transmitted. The storage ring and monochromator therefore provide a strong source of soft X-rays in the spectral range 1000-2500 eV (for more details about the LURE monochromator, see Lemonnier et al. 1978).

The angular position of the two crystals (which determines the wavelength selected by the monochromator) and the distance between them (which determines the height of the emergent X-ray beam) are controlled by a Tektronix 4051 computer (Fontaine, Lagarde, Raoux and Esteve, 1979). The emergent monochromatic beam enters the sample chamber, which has six flanges arranged in a six-way cross. One of these carries the sample holder/manipulator, another carries the electron yield detector and the remaining flanges provide connections for vacuum pumping,

viewing window and an ionization chamber which can be used to measure the transmitted beam for the conventional mode of EXAFS. A photograph of this arrangement is shown in figure 3.3.2. The pressure in the monochromator and the sample chamber was about 10^{-7} torr.

The sample to be examined was mounted on a plate (see fig. 3.3.3) which could be rotated through a full 360° by means of a rotary drive. This plate was designed to carry a number of samples on each side so that measurements on various types of oxide film could be made under identical conditions. The individual samples could be selected by vertical movement and, as necessary, rotation through 180° using the rotary drive manipulator unit. The plate was also constructed so that transmission EXAFS measurements could be made on a thin aluminium foil mounted over a 25 mm aperture. The plate was fabricated from brass and it was possible to use the electron yield from the unpolished surface to obtain a measure of the background spectrum of radiation from the monochromator and storage ring. This was essential for the extraction of EXAFS data from the electron yield from the specimens.

The monochromator crystals become degraded as a result of long periods of exposure to the high fluxes of X-rays provided by the storage ring. In order to ensure sufficiently large outputs from the monochromator and also to retain the high energy resolution required for EXAFS measurements, the crystals were freshly cleaved to remove any contamination before the EXAFS experiments were carried out.

3.4. Data collection

To perform an EXAFS experiment in the total electron yield mode, all the electrons emitted from the surface of the sample are collected, including secondary electrons as well as primary Auger and

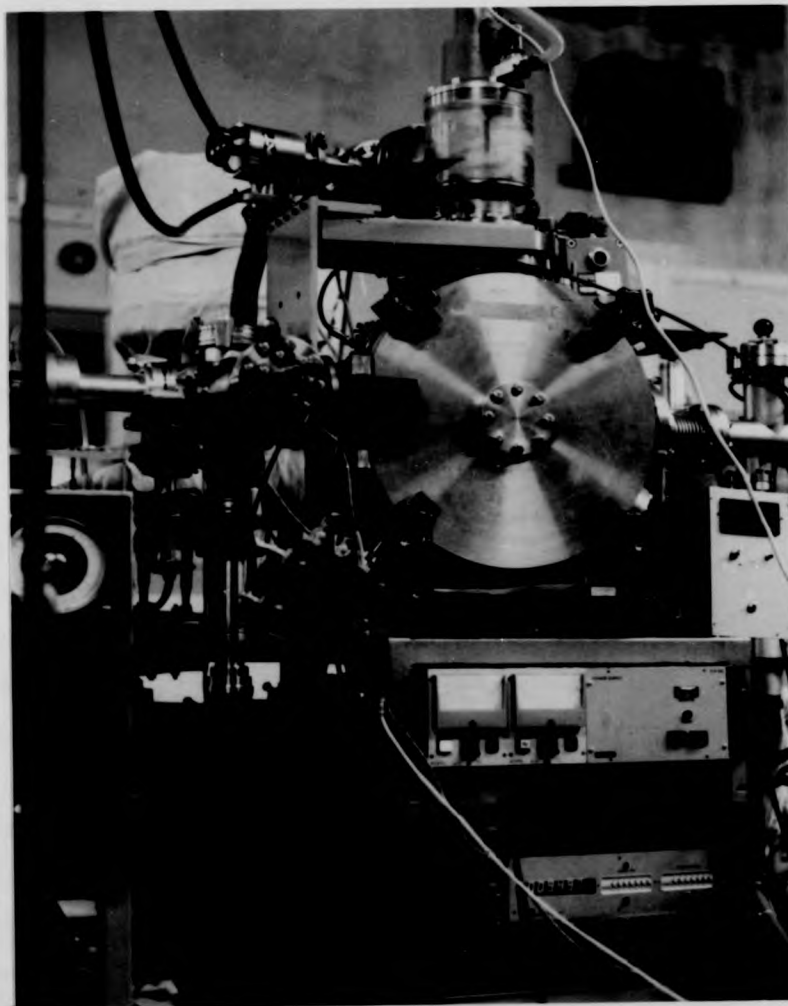


Figure 3.3.2. A photograph showing the monochromator and the sample chamber arrangement.

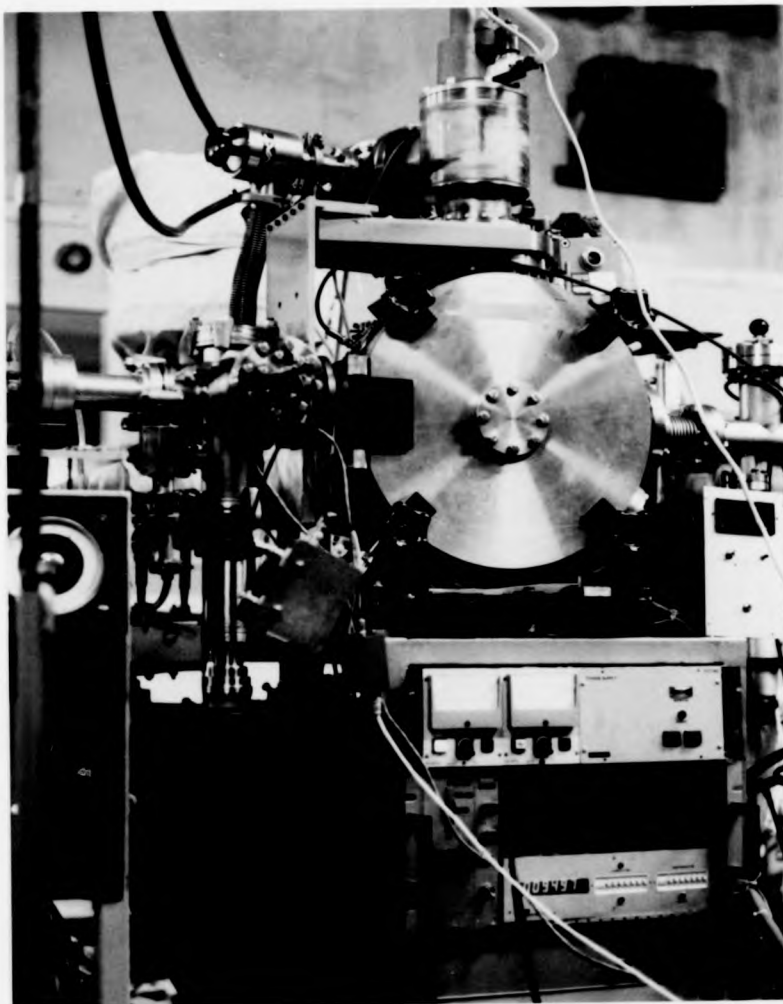


Figure 3.3.2. A photograph showing the monochromator and the sample chamber arrangement.



Figure 3.3.3. A photograph showing the sample holder (un-polished brass surface), with the actual size of samples mounted and a 25 mm aperture to use for transmission EXAFS measurement.

photoelectrons. This total emission was collected using a channel electron multiplier (Galileo type 4800 channeltron, open ended). The channeltron was operated in a pulse counting mode. The front of the channeltron was positioned about 7 cm from the sample, and the sample holder was rotated to obtain an optimum take-off angle. It was found by trial and error that an angle of incidence of 40° for the output beam of the monochromator gave the best signal-to-noise ratio for the total electron yield - EXAFS spectra. The front of the channeltron was set at + 250 volts to attract the secondary electrons emitted from the surface of the sample. The output of the channeltron was passed through a pre-amplifier to a pulse amplifier and discriminator (see figure 3.4.1) to improve the signal-to-noise ratio. The noise level was further reduced by inserting a thin polypropylene film across the entrance to the specimen chamber in order to filter out stray radiation in the form of either secondary electrons or low energy ultra violet photons from the monochromator. The channeltron was capable of recording up to 10^6 counts sec^{-1} , but the counting rate was limited to about 10^4 counts sec^{-1} by the available photon flux.

EXAFS measurement in the transmission mode was made on a thin aluminium foil using an ionization chamber to record the incident and transmitted X-ray intensities. The ionization chamber was filled with air to a pressure of about 300 torr, and had a $3\text{ }\mu\text{m}$ thick mylar window, chosen because mylar does not absorb more than a few % of the incident X-ray beam in the soft X-ray range of 1000 eV to 2500 eV. The output of the ionization chamber was passed through a Keithley amplifier and then a voltage-to-frequency converter to produce a frequency which was proportional to that input voltage. This a.c. signal was converted to a digital input for the data acquisition by means of a scalar circuit.

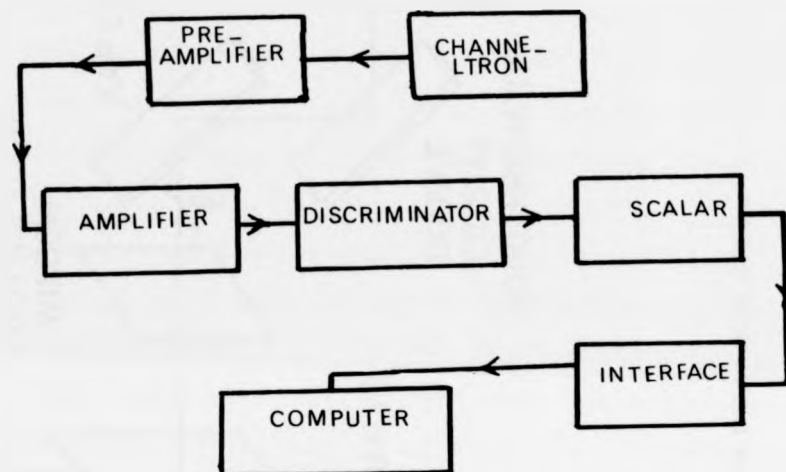


Figure 3.4.1. A block diagram of the electronic system used in the electron yield counting.

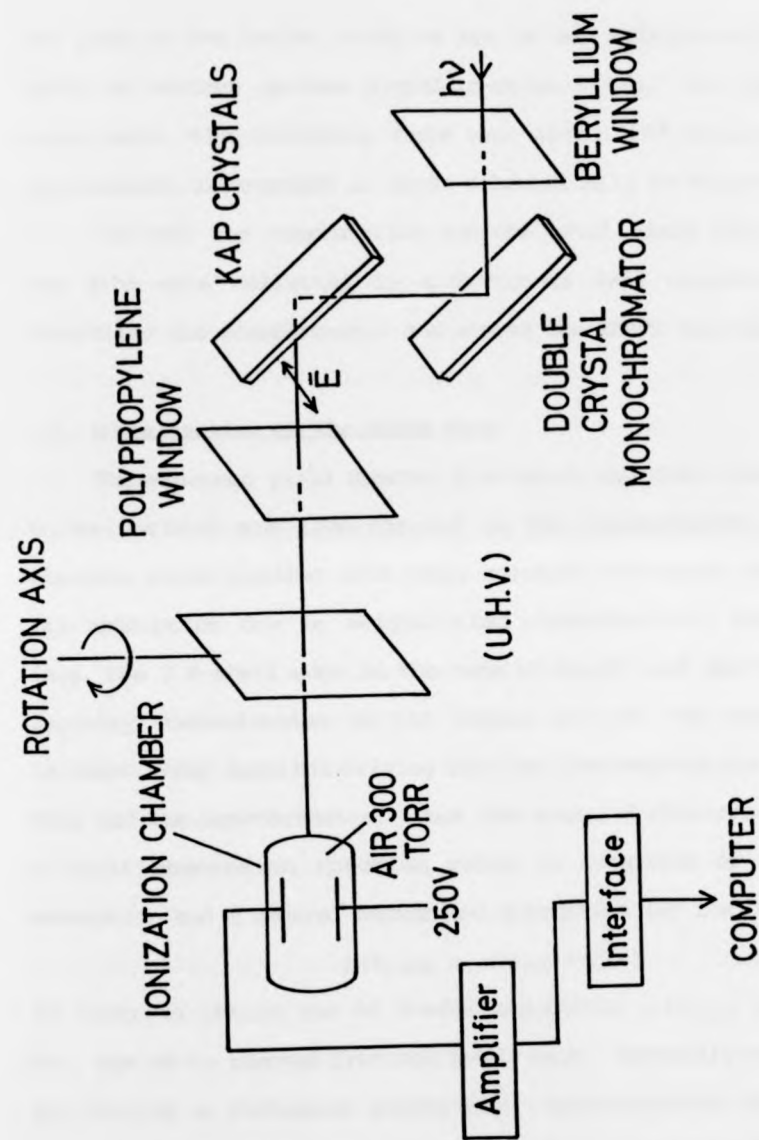


Figure 3.4.2. The experimental arrangement for recording the transmission EXAFS

The gate of the scaler could be set to any multiple of one second in order to achieve optimum signal-to-noise ratio. In the transmission experiment the counting rate was about 10^4 counts sec^{-1} . The experimental arrangement is shown schematically in figure 3.4.2.

In both the transmission and the total yield EXAFS measurements the data were collected by a Tektronix 4051 computer, which also controlled the monochromator and stored the EXAFS spectral data.

3.5. Normalization of the EXAFS data

The electron yield spectra from which the EXAFS oscillations have to be derived are incorporated in the measurements of the total electron yield together with other spectral variations which arise from (a) absorption due to neighbouring characteristic absorption edges (e.g. the O K-shell edge in the case of Al_2O_3) and (b) the presence of impurity contamination in the sample and (c) the variation in the incident X-ray spectrum arising from the characteristics of the storage ring and the monochromator. Thus the measured data can be regarded as a total absorption spectrum which is composed of the Al K-edge absorption and a general background absorption (μ) i.e.

$$\mu(k)_{\text{obs}} = \mu(k)_{\text{Al}} + \mu'(k)$$

In order to obtain the Al K-edge absorption $\mu(k)_{\text{Al}}$, the background, $\mu'(k)$, has to be removed from the total data. Generally this can be done by fitting a Victoreen polynomial representative of the pre-edge background. In this way it is possible to remove the non-K-shell absorption by extrapolating the pre-edge absorption and subtracting this Victoreen polynomial from the total absorption spectrum, (see for example, Lee et al. 1981). The accuracy of this method is limited because it does not take into account the variation of the X-ray flux incident on the specimen, over the whole experimental range.

Rather than using the method of simply extrapolating the pre-edge background a new, empirical method has been used in the present work to normalise the EXAFS data. This involves using a standard target containing no edges in the absorption spectral region of interest (1500 eV - 2500 eV) and counting the electron emission from its surface. For this purpose it was found convenient to use the "dirty" surface of the brass specimen holder described in section 3.3. Such a surface is expected to be covered with oxygen, nitrogen, carbon and hydrogen all of which have absorption edges at lower photon energy (O-532 eV, N-399 eV, C-230 eV and H-14 eV). The copper and zinc in the brass have absorption edges at much higher energies and the electron yield is therefore a broad spectrum of secondary emission, effectively a continuum.

The yield spectrum from the standard surface is therefore representative of the convolution of the various instrumental factors involved, including the synchrotron storage ring and the monochromator. This measured spectrum can therefore be used to normalize the electron yield spectra from the Al_2O_3 samples. In order to carry out the normalization procedure the measured background spectrum must firstly be represented by a smooth polynomial. For this purpose a Chebyshev series polynomial has been employed

$$f(E) = a_0 T_0(E) + a_1 T_1(E) + a_2 T_2(E) + \dots + a_i T_i(E)$$

where $T_1(E)$ is the Chebyshev parameter of the first degree and $T_i(E)$ is the i^{th} degree parameter (for more detail, see Cox and Hayes, 1973).

This polynomial was used to fit the whole range of data and adjusted to achieve the best fit for the experimental data obtained with an angle of incidence of 40° which was found to give the best

signal-to-noise (see section 3.4). The results so obtained are shown in figure 3.5.1. For comparison the results are also shown for angles of incidence of 65° and 90° using the same polynomial with suitable scaling factors. This demonstrates the very satisfactory fit that can be obtained using the Chebyshev series polynomial.

Figure 3.5.2. illustrates the procedure for using the polynomial derived from the measured background to obtain the normalised X-ray absorption spectra. The upper curve (1) is the total electron emission measured for an anodic oxide formed on aluminium in neutralized tartaric acid electrolyte, (the preparation of this oxide film will be discussed in the next section). The raw data contain the absorption above the Al K-edge for the film superimposed on the general background. By fitting the Chebyshev polynomial function derived from the electron emission of the brass surface (Figure 3.5.1.) to the measured intensity below the aluminium K-edge with a suitable scaling factor curve (2), shown in figure 3.5.2., can be obtained. By subtracting curve (2) from curve (1) and dividing by (2), the true absorption spectrum due to the Al K-edge can be derived as shown in figure 3.5.3.

3.6. The sampling depth of the total electron yield technique

The total electron yield from the sample consists of all electrons (photoelectrons, Auger electrons and secondary electrons produced by inelastic collisions) originating not only from the surface but also from material below the surface. This can be characterized by a sampling depth which is clearly related to the mean electron escape depth. It has been shown previously by Jones and Woodruff (1982) that the total electron yield spectrum for a sample consisting of an anodic oxide film on aluminium can be accounted for by a simple incoherent

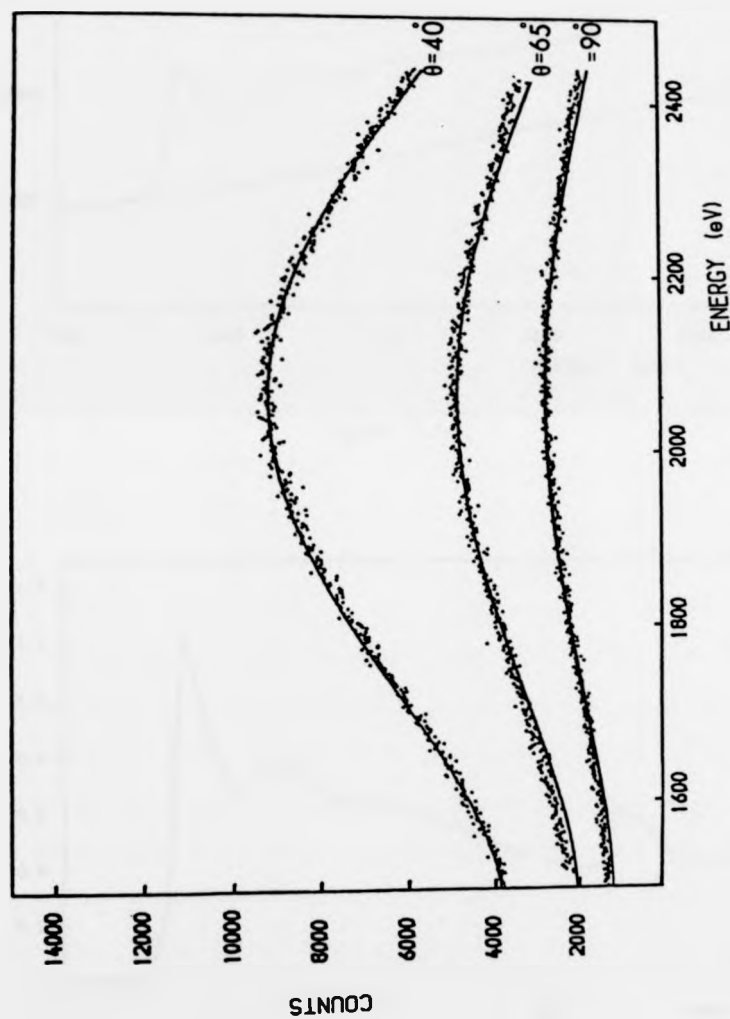


Figure 3.5.1. The electron yield spectra from the "dirty" brass target versus photon energy for angles of incidence 40° , 65° and 90° . The smooth curves are best fit polynomials (Chebyshev series) to be used to normalise the electron yield spectra.

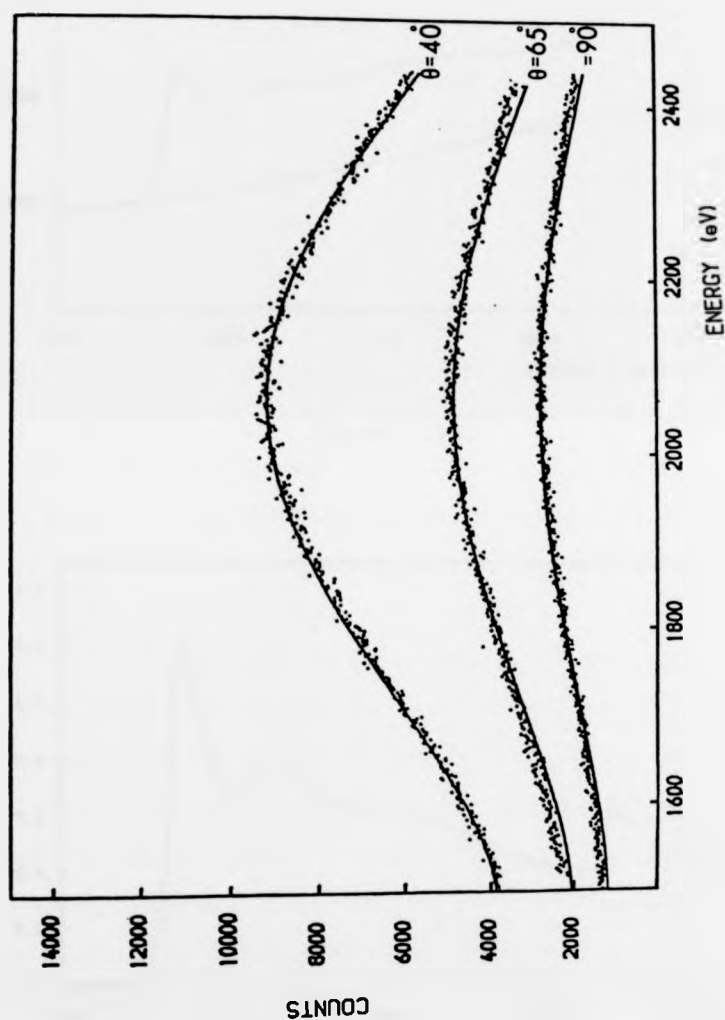


Figure 3.5.1. The electron yield spectra from the "dirty" brass target versus photon energy for angles of incidence 40° , 65° and 90° . The smooth curves are best fit polynomials (Chebyshev series) to be used to normalise the electron yield spectra.

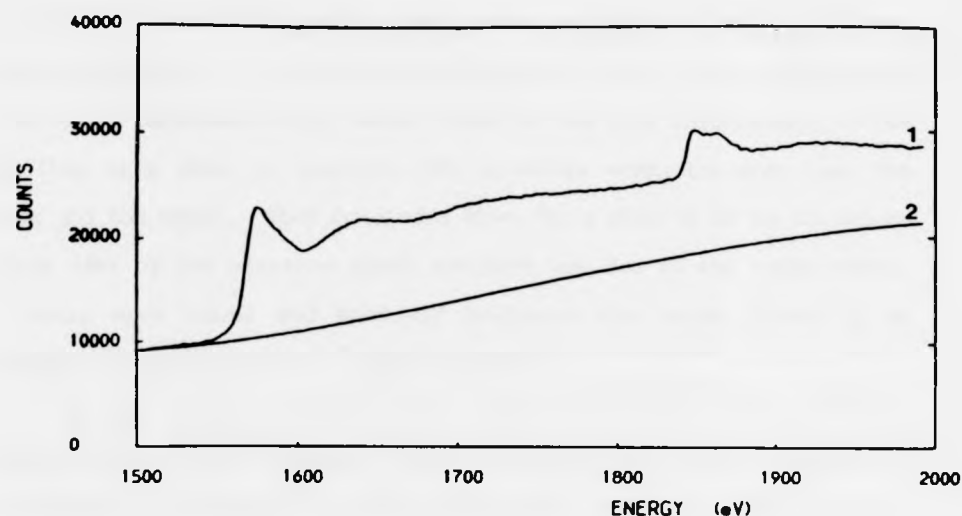


Figure 3.5.2

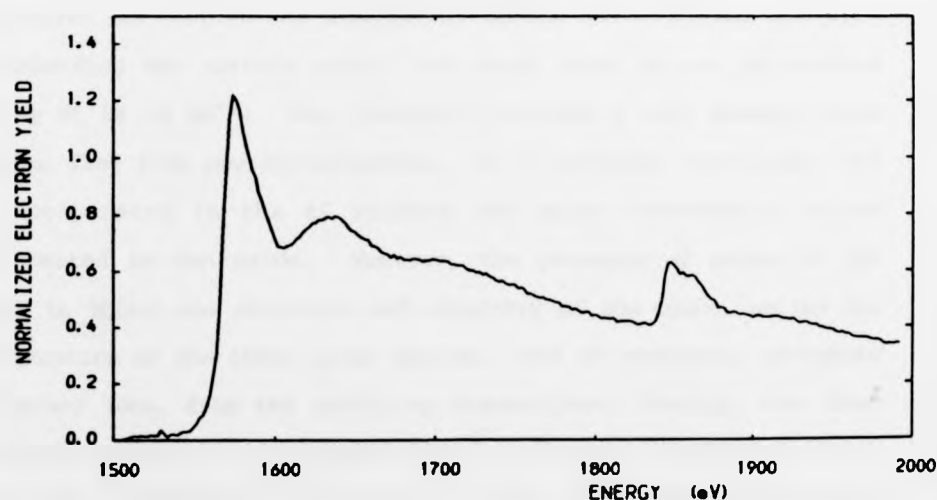


Figure 3.5.3

Figure 3.5.2 illustrates the procedure followed to normalise the EXAFS spectrum. Curve 1 is the recorded electron-yield spectrum for a 50 nm tartrate formed oxide film; curve 2 is the polynomial described in figure 3.5.1 adjusted to fit the electron-yield spectrum prior to the Al K-edge.

Figure 3.5.3 shows the normalized EXAFS spectrum, obtained by subtracting curve 2 from curve 1 and dividing by curve 2 in figure 5.3.2.

summation of the EXAFS due to the oxide and EXAFS arising from the underlying metal. By analysing measurements of the electron yield from a series of specimens with oxide films of various thicknesses (3-100 nm) they were able to quantify the relative contributions from the oxide and the metal. They concluded that for a film of 50 nm thickness almost 100% of the electron yield spectrum was due to the oxide EXAFS. In their work Jones and Woodruff prepared the oxide films by an anodizing treatment using a borate solution.

In the present study this investigation of the surface sensitivity of the electron field technique has been extended to measurements on films of various thicknesses (5-100 nm) formed on pure aluminium by anodic oxidation in sodium tartrate electrolyte. In all cases the aluminium surface was initially polished mechanically and thoroughly washed in distilled water and methanol. A final surface preparation was carried out immediately before the anodising treatment by bombarding the surface with 5 keV argon ions, at an ion current density of $20 \mu\text{A mm}^{-2}$. This procedure provides a very smooth, clean surface, free from any contamination. It is possible that argon will be incorporated in the Al surface and might eventually become incorporated in the oxide. However, the presence of argon is not likely to affect the structure and chemistry of the oxide, unlike the incorporation of the other ionic species, such as carbonate, phosphate and borate ions, from the anodising electrolytes. Finally, the clean aluminium surfaces were anodised in a neutral solution tartrate electrolyte, composed of 0.5 M tartaric acid $(\text{CHOH.COOH})_2$ neutralized to $\text{pH} \approx 7.2$ with 0.5 M sodium hydroxide (NaOH). Throughout, an aluminium cathode was employed. This treatment yields a thin oxide layer of very uniform thickness, the so-called barrier layer. The

film thickness is dependent on the anodizing voltage, with a well defined relationship of about 1.4 nm V^{-1} (Hunter and Fowle, 1954). A number of oxide films with increasing thickness were grown in this way. A similar set of oxide samples, prepared under the same condition, were hydrated for 15 minutes at 85°C and these were also used to study the surface sensitivity of the electron yield technique. EXAFS spectra of both the unhydrated and hydrated specimens were recorded by counting the electron yield as a function of photon energy at 2 eV intervals from 1500 eV (just below the Al K-edge at 1560 eV) to 2000 eV. These spectra were normalized to allow for variation of the X-ray flux over the energy range, using the method described previously in section 3.5. The spectra from the two sets of measurements are shown in figures 3.6.1 and 3.6.2. Figures 3.6.1 and 3.6.2 also show on a similar scale the transmission EXAFS spectrum obtained for a pure Al foil. On the right-hand side of figures 3.5.1 and 3.5.2 are simulated spectra obtained by a linear combination of the pure aluminium EXAFS spectrum and the 50 nm thick aluminium oxide spectra, in the case of unhydrated oxides, and the pure aluminium and the 50 nm thick hydrated aluminium oxide spectra for the hydrated oxides, with the proportions of oxide and aluminium contributions adjusted to match the corresponding measured spectra.

It can be seen from a comparison of the experimental and simulated spectra that the electron yield EXAFS truly represents the aluminium oxide only if the film thickness is greater than 50 nm. There is about 50% contribution to the EXAFS spectrum from an oxide film of 5 nm and about 90% from a 40 nm thick oxide film.

Figure 3.6.3. shows the results of evaluating the proportions of the oxide EXAFS spectra required to simulate the total electron yield

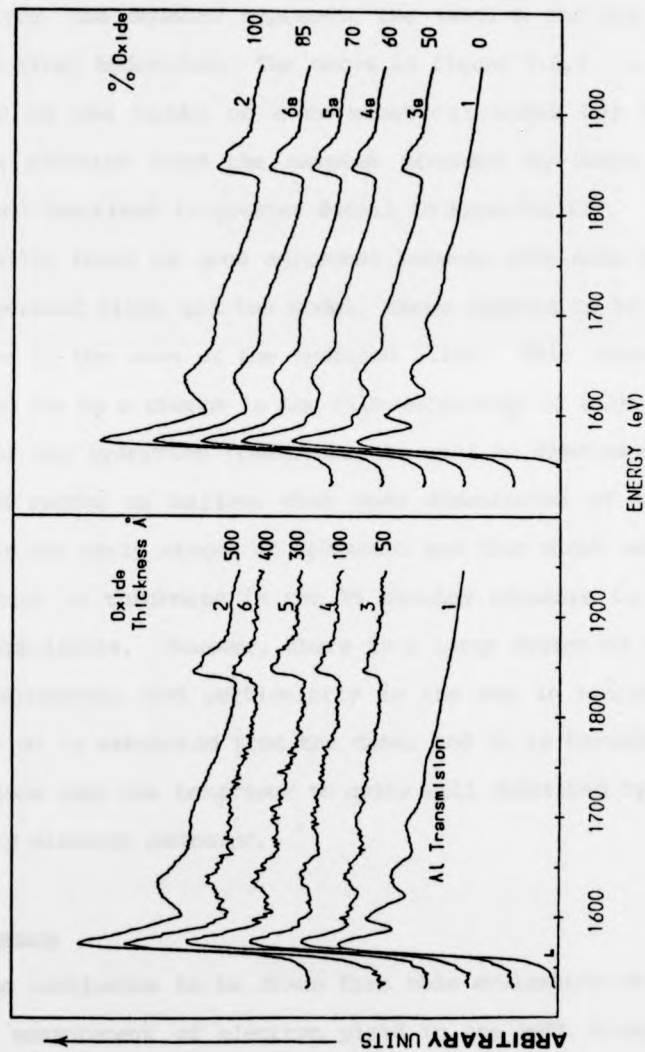


Figure 3.6.1. The electron-yield EXAFS spectra for a series of sodium tartrate formed alumina films with thickness, 50, 100, 300, 400, 500 Å (left hand side). The calculated spectra shown on the right-hand side have been constructed from the Al transmission EXAFS (curve 1) and the EXAFS for 500 Å alumina film (curve 2) with the percentage of oxide contributions shown to give a fit of the experimental spectra.

spectra for films of various thicknesses. The filled circles represents the results obtained by Jones and Woodruff (1982) for films prepared in sodium borate electrolyte whilst the open circles represent the results of the present experiments using sodium tartrate electrolyte. The squares represent the results for the same type of film but after hydration. The curve in figure 3.6.3. is the behaviour expected on the basis of a mathematical model for the secondary electron emission from the samples proposed by Jones and Woodruff (1982) and described in greater detail in Appendix III. It can be seen that, whilst there is good agreement between both sets of results for the unhydrated films and the model, there appears to be a significant departure in the case of the hydrated films. This departure might be accounted for by a change in the film morphology or film thickness as a result of the hydration treatment. As will be discussed in Chapter 6 there is reason to believe that some dissolution of the oxide film occurs in the early stages of hydration and this might well account for a reduction in thickness in the 15 minutes exposure to water used in these experiments. However, there is a large degree of uncertainty in the measurements, and particularly in the way in which this kind of information is extracted from the data, and it is therefore reasonable to conclude that the behaviour is quite well described by the model for secondary electron emission.

3.7. Summary

The conclusion to be drawn from this evaluation of the technique is that measurement of electron yield in the soft X-ray energy range (1000-2500 eV), provides a means of monitoring the Al K-edge EXAFS with a high degree of surface sensitivity and results in good quality

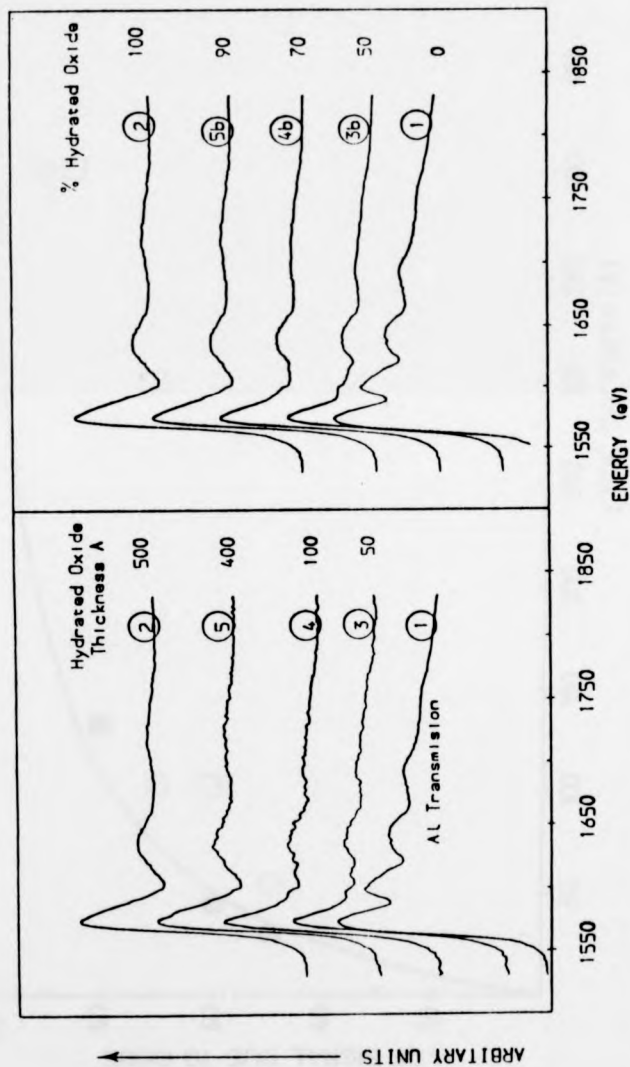


Figure 3.6.2. The electron yield EXAFS spectra for a series of sodium tartrate formed alumina films after hydration at 85°C for 15 minutes with thicknesses 50, 100, 400 and 500 Å (left-hand side). The calculated spectra shown on the right-hand side have been constructed from the pure Al transmission EXAFS (curve 1) and the EXAFS for the 500 Å hydrated alumina (curve 2) with the percentage of hydrated oxide contributions shown to give a fit of the experimental spectra.

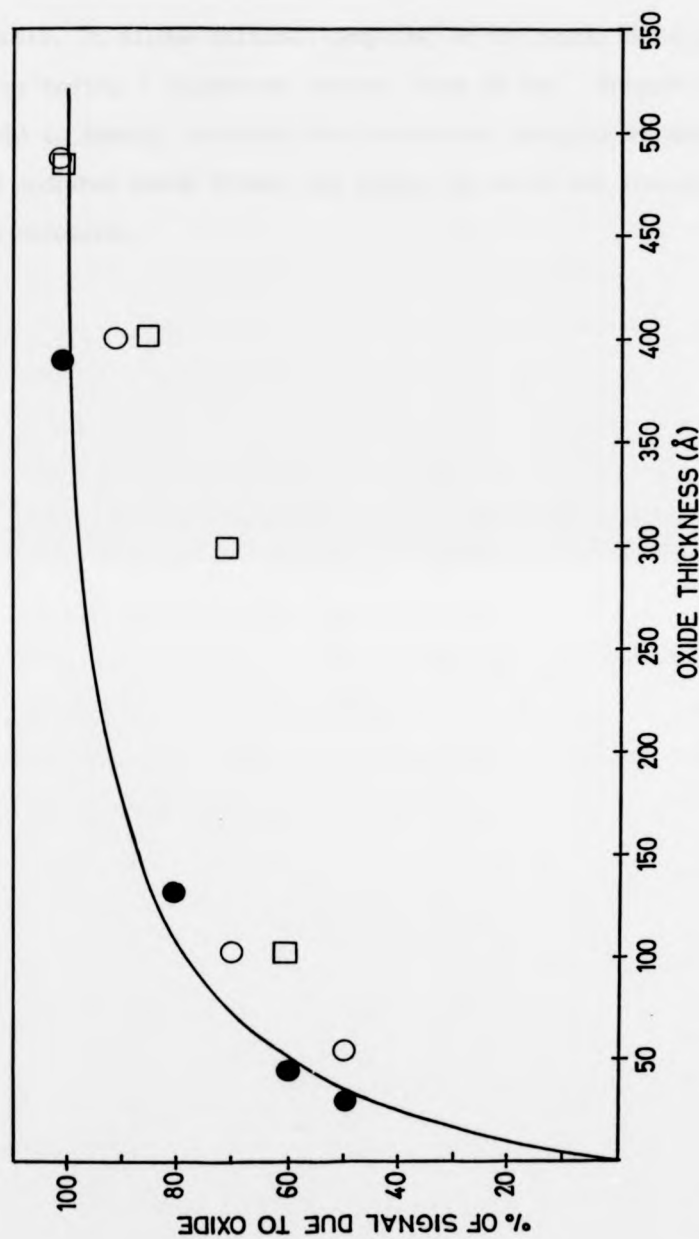


Figure 3.6.3.

The percentage contribution from the total EXAFS spectrum for various thicknesses of film as deduced from figures 3.6.1 and 3.6.2 and that of Jones and Woodruff (1982). ● denotes results obtained by Jones and Woodruff for borate formed film; ○ are the results obtained in this work for as-formed tartrate films (fig. 3.6.1); □ are the results obtained for sodium tartrate formed films, after hydration in hot water at 85°C for 15 minutes (figure 3.6.2). The curve is the theoretical relationship based on calculations by Jones and Woodruff.

spectra. It allows reliable sampling of the oxide structure for alumina films having a thickness greater than 50 nm. Therefore the electron yield is ideally suitable for structural analysis of amorphous alumina and hydrated oxide films, the result of which are discussed in the next two chapters.

REFERENCES

1. Cox, M.G. and Hayes, J.C., (1973), Report NAC26, National Physical Laboratory, Teddington, Middx.
2. Forty, A.J. (1979), Proc. Roy. Inst. (GB), 50, 1.
3. Fontaine, A., Lagarde, P., Raoux, D. and Esteva, J.M., (1979), J. Phys. F: Metal Phys, 9, 2143.
4. Guyon, P.M., Depautex, C., Morel, G., (1976), Rev. Sic. Inst., 47, 1347.
5. Hunter, R.G. and Fowle, P., (1954), J. Electrochem. Soc., 101, 481.
6. Jones, R.G. and Woodruff, D.P., (1982), Surf. Sci, 38, 46.
7. Kunz, C., (1979), Synchrotron Radiation, ed. C. Kunz, (Springer-Verlag, Berlin Heidelberg New York).
8. Lee, P.A., Citrin, P.H. and Eisenberger, P. and Kincaid, B.M., (1981), Rev. Mod. Phys. 53, 769.
9. Lemonnier, M., Collet, O., Depautex, C., Esteva, J.M., Raoux, D., (1978), Nucl. Inst. Meth. 152, 109.

CHAPTER 4

SAMPLE PREPARATION, EXAFS ANALYSIS PROCEDURE AND RESULTS FOR ANODIC ALUMINIUM OXIDE FILMS AND HYDRATED OXIDE FILMS

4.1. Introduction

From the historical review of work done on the oxide films formed on aluminium by anodic treatments in aqueous electrolytes, presented in Chapter 1, it is evident that a great deal is already known about the morphology and the chemical composition of such films. However, there is relatively little knowledge about the structure of the oxide from which the films are formed, particularly in the case of amorphous films. Because of the importance of the anodising treatment in technological applications it is clearly very desirable for structural determination to be made. The various attempts that have been made to use conventional X-ray and electron diffraction techniques have achieved only limited success. In contrast, the technique of extended X-ray absorption fine structure (EXAFS) analysis should have a much greater potential for this kind of study since it is a structural probe which does not depend on a regular ordering of the molecular structure and it has already proved to be a very useful technique for studying amorphous materials such as inorganic glasses, as described in Chapter 2. The method of electron yield EXAFS, having a high degree of surface sensitivity, should be particularly useful for the study of thin oxide films, 50 nm or greater in thickness.

This Chapter describes the application of total electron yield EXAFS to the study of several different aluminium oxides, 50-150 nm thick, formed in different electrolytes and subjected to various hydration treatments. In the following sections the procedures used

for the preparation of the aluminium substrate and the method for carrying out the anodising in the various electrolytes are described. The procedure for hydrating the oxide films after anodising is also described. In the later sections the procedures for analysis of the EXAFS data and the measurements of structural details (such as Al-O bond length) are reported for all the oxides in both the as-formed condition and also after the hydration.

4.2. Sample Preparation

4.2.1. General background

When aluminium is made the anode is an electrolytic cell, an oxide is formed on the surface. This oxide has a complex microstructure (see, for example Thompson and Wood, 1981) which depends on the electrolyte used. Oxide films, formed by anodising in an aggressive electrolyte solution, such as sulphuric acid, chromic acid or phosphoric acid, are generally porous and are partly crystalline (a mixture of amorphous and γ -alumina). The degree of crystallinity increases as the film thickens. With neutral electrolyte solutions, such as sodium tartrate, or sodium borate, at room temperature, the films are thinner and more uniform (non-porous, barrier layer films). The thickness is proportional to the applied voltage with a relationship of about 1.4 nm per volt at room temperature ($d = 1.226 + 0.0047t(\text{nm})$, where t is the temperature of the electrolyte measured in $^{\circ}\text{C}$ (Hunter and Fowle, 1954). Very thin films of this type (≈ 10 nm thick) are largely composed of amorphous alumina according to high resolution TEM studies (El-Mashri et al., 1981). Again, for thicker films a greater degree of crystallinity is formed, according to electron and X-ray diffraction studies.

4.2.2. Surface Preparation of the Aluminium substrates prior to Anodisation

The oxide layers in all our experiments were prepared on high purity (99.999%) polycrystalline aluminium sheets. In all cases the specimen dimensions were 20 x 10 x 0.5 mm. The surfaces of these were carefully mechanically polished with a very fine paste of alumina powder (0.01 μm). This was followed by applying a liquid metal polish, such as "Brasso". The surface was then thoroughly washed in running de-ionized water and finally rinsed in methanol. The final surface preparation, carried out immediately before the anodising treatment, consisted of bombardment of the surface by 5 kV argon ions for 45 minutes, using an Ion Tech B21 gun. In order to avoid serious surface damage during this treatment, the ion gun was operated at an ion current of 20 μA , resulting in a low current density (0.2 A m^{-2}). This proved to be sufficient to remove gross contamination and gave a smooth, clean surface.

4.2.3. Anodising Treatment

Two types of electrolyte were used in this work. One type, consisting of neutral solutions, gave uniform non-porous layer type films, while the other solutions used were more strongly acidic and these formed porous oxide films. In all these treatments the cathode was in the form of a ring of aluminium surrounding the specimen.

Three neutral electrolyte solutions were used to form the barrier layer (non-porous) oxide. These were:-

(i) Sodium tartrate solution

The sodium tartrate bath was composed of 0.5M tartaric acid (CHOH.COOH)₂ which was neutralised to $\text{pH} \approx 7.2$ with 0.5M sodium hydroxide (NaOH). Initially, the anodising treatment was carried out in a pyrex glass container, but this was found to lead to incorporation of Si in the oxide (see later sections of this chapter and also Chapters 5 and 6). Subsequently, the anodisation was carried out in an aluminium container to avoid this.

(ii) Sodium oxalate solution

The sodium oxalate bath consisted of 0.5M oxalic acid ($\text{(COOH)}_2 \cdot 2\text{H}_2\text{O}$). This was neutralised to $\text{pH} \approx 7.2$ with 0.5M sodium hydroxide. An aluminium container was used in this process.

(iii) Sodium borate solution

The sodium borate solution was composed of 0.5M boric acid (H_3BO_3), neutralised to $\text{pH} \approx 7.2$ with 0.5M sodium hydroxide. An aluminium container was used in this process.

In each case the oxide films were prepared at a constant voltage (≈ 35 volts) to yield an oxide thickness of 50 nm.

Two acid electrolyte solutions were used to form the porous oxide films. These were:-

(iv) Phosphoric acid solution

The phosphoric acid bath consisted of an aqueous solution of 10% wt orthophosphoric acid (H_3PO_4). In this case a pyrex

(i) Sodium tartrate solution

The sodium tartrate bath was composed of 0.5M tartaric acid (CHOH.COOH)₂ which was neutralised to pH \approx 7.2 with 0.5M sodium hydroxide (NaOH). Initially, the anodising treatment was carried out in a pyrex glass container, but this was found to lead to incorporation of Si in the oxide (see later sections of this chapter and also Chapters 5 and 6). Subsequently, the anodisation was carried out in an aluminium container to avoid this.

(ii) Sodium oxalate solution

The sodium oxalate bath consisted of 0.5M oxalic acid ($\text{(COOH)}_2 \cdot 2\text{H}_2\text{O}$). This was neutralised to pH \approx 7.2 with 0.5M sodium hydroxide. An aluminium container was used in this process.

(iii) Sodium borate solution

The sodium borate solution was composed of 0.5M boric acid (H_3BO_3), neutralised to pH \approx 7.2 with 0.5M sodium hydroxide. An aluminium container was used in this process.

In each case the oxide films were prepared at a constant voltage (\approx 35 volts) to yield an oxide thickness of 50 nm.

Two acid electrolyte solutions were used to form the porous oxide films. These were:-

(iv) Phosphoric acid solution

The phosphoric acid bath consisted of an aqueous solution of 10% wt orthophosphoric acid (H_3PO_4). In this case a pyrex

container was used. This did not lead to Si contamination of the oxide. The aluminium surface was first pre-oxidised using the Forest Product Laboratory (FPL) process. This is the standard treatment for the preparation of Al surfaces for the preparation of good adherent porous oxide. The FPL solution contained $\text{Na}_2\text{Cr}_2\text{O}_3$, H_2SO_4 and H_2O in a ratio of 1:10:30 by weight. The aluminium surface was immersed for 15 minutes in the solution at 60°C . This formed a layer of oxide about 8 nm thick on the surface of the aluminium. Immediately after this treatment the sample was thoroughly washed in running de-ionized water and dried using an air blower. It was then anodised in the phosphoric acid bath at a constant voltage of 10 volts, and an initial current density of 1000 A m^{-2} , for 15 minutes at room temperature. The oxide film thus formed was expected to have an average thickness of 100 nm according to work done previously on similar films (Ahearn et al, 1980).

(v) Chromic acid solution

The chromic acid bath was composed of an aqueous solution of 5% by weight of chromic trioxide (Cr_2O_3). Since the leaching of Si from the glass was not expected in this case the anodising treatment was performed in a pyrex container. This was found to be convenient because it permitted visual observation of the surface. However, it was found that a certain amount of Si contamination actually occurred as will be described later and in chapters 5 and 6. Again, the aluminium surface was pre-treated in FPL solution using an identical procedure to that described for the phosphoric acid process. The surface was then

anodised at a constant voltage of 49 volts and an initial current density of 1000 A m^{-2} , for 40 minutes. The temperature of the bath was kept at 35°C during the anodising process. This process produced a very thick oxide estimated to be about 150 nm according to previous work using a similar method of preparation by Venables et al (1979).

The α -alumina specimen used as the model compound

In order to derive values for the Al-O bondlength from EXAFS measurements on all these films it is necessary to compare the EXAFS data with EXAFS from a suitable reference material (see Chapter 2). For this purpose a disc of α -alumina cut from a large single crystal of sapphire was used. This was mechanically polished using a diamond disc (with surface grade 30-40 μm) for 3 hours to produce a smooth surface, then thoroughly washed in running de-ionised water and finally rinsed in methanol. This surface was then bombarded with argon ions for 3 hours, as described previously in this chapter.

4.2.4. The Hydration of the Oxide Films

In this section the treatment used to hydrate the various types of anodized aluminium oxide is described.

Samples of the non-porous oxides, 50 nm thick were formed on pure aluminium in sodium tartrate, sodium oxalate and sodium borate electrolytes as described in Section 4.2.3i, ii, iii. These were then hydrated by immersion in hot water at about 85°C , for 30 minutes. This period of immersion was found to be sufficient for complete hydration of the film as estimated by the evolution of gas from the

metal substrate and the accompanying change in colour of the oxide surface from whitish to a pale brown. The hydrogen gas evolution indicates that the water has penetrated through the oxide surface, and has reached the underlying aluminium substrate. The time needed for complete oxide-to-oxyhydroxide conversion, revealed by these observations, was approximately 25 minutes, and therefore the oxide should be converted fully to oxy-hydroxide in 30 minutes. This is consistent with observations by other workers (Ahearn, 1983, private communication).

Samples of the porous oxides, 100-200 nm thick were formed in 10% wt phosphoric acid and 5% wt chromic acid, following the same procedures described in Section 4.2.3 iv and v. Oxides formed in both electrolytes have a duplex morphology: there is a thin barrier layer, 10-15 nm thick, formed initially on the aluminium surface, followed by a thicker porous layer (Venables et al., 1979; Thompson and Wood, 1981). These oxide films were hydrated by immersion of the oxidised metal in hot water at $85^{\circ}\text{C} \pm 5^{\circ}\text{C}$. The time for hydration as indicated by a colour change was considerably longer than was found for the non-porous oxides, requiring about 4 hours for complete hydration. This longer hydration period has been attributed to the time required for water to penetrate through the duplex oxide layer. It is also possible, as will be discussed in Chapter 6, that the incorporation of anion species from the electrolyte during the anodizing treatment might inhibit the hydration (Davis et al, 1982; El-Mashri et al, 1983, Alwitt, 1984, private communication).

4.3. The Analysis of EXAFS Data to Obtain Structural Information (Al-O Bond Length) for the Anodic Oxide Films

This section describes the procedure used to obtain the extended X-ray absorption fine structure spectra from the raw data collected as described in Chapter 3. It also describes the data manipulation used to extract the structural information from the EXAFS spectrum.

The first step in the data analysis is to normalise the measured electron yield, allowing for the background intensity, to give the Al K-edge absorption spectrum for the sample. The second step is to separate the EXAFS oscillation function, χ , from the smooth atom-like background. The resulting fine structure contains the structural information. The third step in the analysis is to convert the EXAFS oscillations from being a function of the photon energy, $\chi(E)$ to a function of photoelectron wave vector, $\chi(k)$. The Fourier transform of $\chi(k)$ can then be used to give information about nearest-neighbour, next-nearest neighbour etc. separations. This requires a knowledge of the appropriate phase shift which can be determined from the EXAFS of the reference compound (α -Al₂O₃ in this case) or can be computed from tables published by Lee and Beni (1977).

In this section the analytical procedures for the oxide formed in the sodium tartrate electrolyte only will be described in detail. The same procedure has been followed to analyse the EXAFS for all the other oxides and hydrated samples but only the important features and results for these will be given.

4.3.1. The EXAFS analysis of the oxide formed in sodium tartrate electrolyte

(i) Background subtraction and normalisation of the electron yield spectra

The EXAFS above the Al K-edge must be normalised to allow for variation of the incident photon intensity in that part of the spectrum and the contribution to the absorption from other absorption edges (the background absorption) must be subtracted. This is done by fitting the polynomial derived from the electron yield from the brass test-sample to the pre-edge electron yield for the oxide. This procedure has already been described in detail in Chapter 3 and can be illustrated by reference to figures 3.5.2. and 3.5.3. The variation of background intensity is represented by curve (2) in figure 3.5.2 fitted to the pre-edge electron yield data. The EXAFS spectrum is then normalised by subtraction of curve (2) from curve (1) and division of this difference by curve (2).

(ii) The extraction of the EXAFS oscillation function $\chi(E)$

The normalised electron yield is a direct measure of the X-ray absorption spectrum $\mu(E)$. The next step in the analysis is to isolate the EXAFS oscillations, $\chi(E)$, in the normalised K-shell absorption spectrum $\mu(E)$, by subtracting the free atom-like absorption $\mu_0(E)$. This is generally not possible experimentally, and usually μ_0 is obtained by fitting a smooth polynomial through the oscillations in the normalised absorption coefficient, $\mu(E)$. The EXAFS oscillation function $\chi(E)$ per atom of aluminium in the sample is then obtained from the computation

Figure 4.3.1a

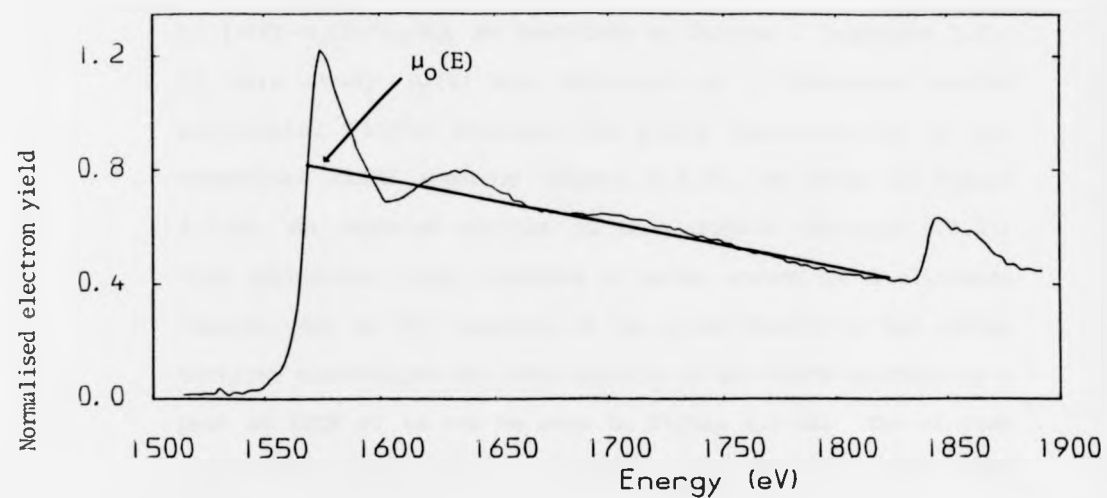


Figure 4.3.1b

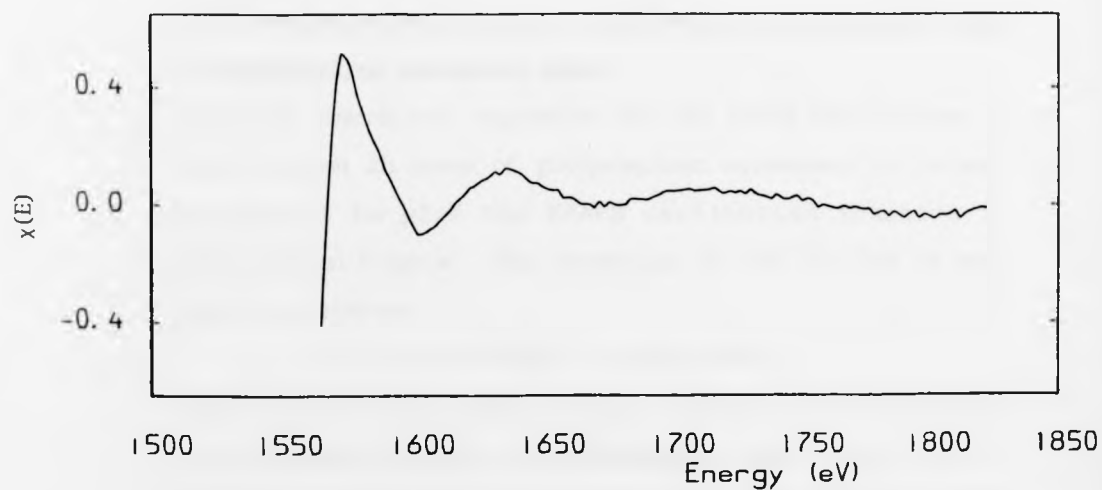


Figure 4.3.1a The normalised electron yield for the sodium tartrate formed oxide showing the polynomial used for extracting the EXAFS function $\chi(E)$.

Figure 4.3.1b A plot of the fine structure function, $\chi(E)$, against the photon energy (eV) obtained from figure 4.3.1a.

of $(\mu(E) - \mu_0(E))/\mu_0(E)$, as described in Chapter 2 (equation 2.1). In this study $\mu_0(E)$ was obtained as a Chebyshev series polynomial fitted through the EXAFS oscillations in the normalised EXAFS spectrum (figure 3.5.3), as shown in Figure 4.3.1a. As reported earlier in this chapter (Section 4.2.3i) this particular oxide contains a larger amount of a siliceous impurity due to the leaching of the pyrex beaker by the sodium tartrate electrolyte and this appears in the EXAFS spectrum as a peak at 1839 eV as can be seen in figure 4.3.1a. The Si peak (Si K-shell absorption) is removed from the normalised EXAFS oscillation function (figure 4.3.1b) simply by terminating the spectrum at a point just below the Si K-edge.

(iii) The conversion of $\chi(E)$, in photon energy space, to $\chi(k)$, in photoelectron wavevector space

Since the theoretical expression for the EXAFS oscillations is usually given in terms of photoelectron wavevector it is more convenient to plot the EXAFS oscillation function in photoelectron k-space. The conversion of $\chi(E)$ to $\chi(k)$ is made using the relation

$$k = (2m/h)^{1/2} \sqrt{E - E_0} = 0.5123 \sqrt{E - E_0}$$

where E is the X-ray photon energy, measured in eV and E_0 being the true position of the Al K-absorption edge. Great care is necessary in the choice of the value of E_0 since this determines the k-scale, and this in turn affects the determination of the Al-O bond length. In this present study two different methods of bond length determination were used; in both cases care was taken to avoid this form of systematic error

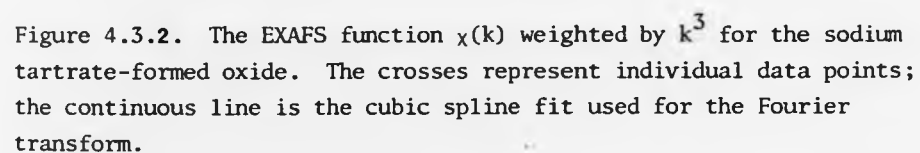


Figure 4.3.2. The EXAFS function $\chi(k)$ weighted by k^3 for the sodium tartrate-formed oxide. The crosses represent individual data points; the continuous line is the cubic spline fit used for the Fourier transform.

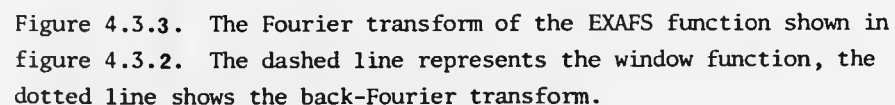
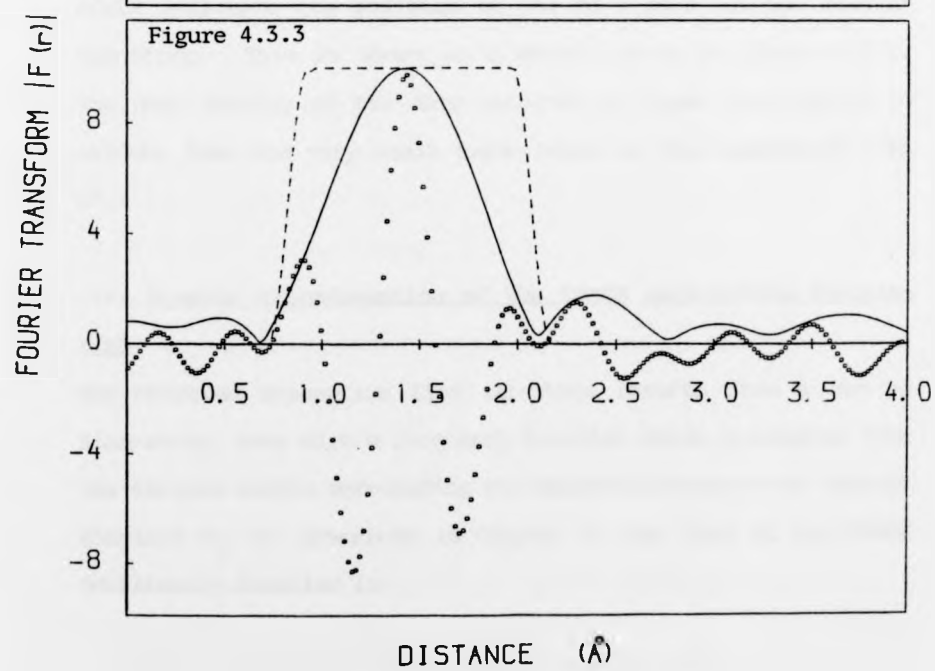
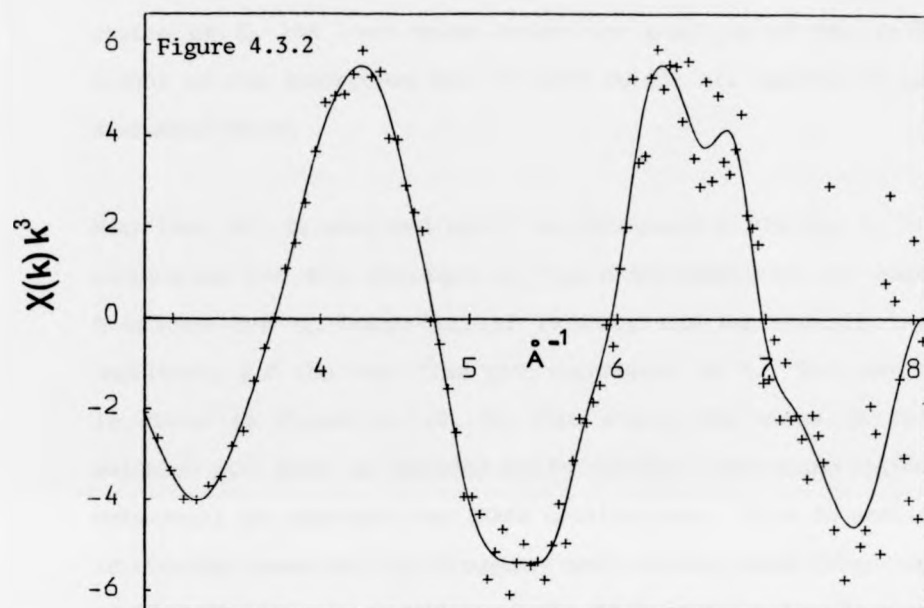


Figure 4.3.3. The Fourier transform of the EXAFS function shown in figure 4.3.2. The dashed line represents the window function, the dotted line shows the back-Fourier transform.



as will be explained in Sections 4.3.1 (iv), and the best choice of E_0 has been taken to be the position of the half height of the absorption edge at 1558 eV for all spectra to be discussed below.

Next the $\chi(k)$ is weighted by k^3 , as discussed in Chapter 2, to compensate for the decrease of the EXAFS amplitude at high k -values due to Debye-Waller factor, the backscattering amplitude, and the mean free path dependence on k . The result is shown in figure 4.3.2. At this stage the noise in the weighted $\chi(k)$ data is filtered out by fitting a smoothing spline polynomial to represent the EXAFS oscillations. This is useful in removing unwanted high frequency oscillations which otherwise could influence the position of the Al-O peak in the Fourier transform. This is shown as a smooth curve in figure 4.3.2. The high quality of the data obtained in these experiments is evident from the very small noise level in the unsmoothed $\chi(k)k^3$.

(iv) Fourier transformation of the EXAFS oscillation function $\chi(k)$

The observed absorption fine structure results from a sum of sine-waves, each with a frequency function which originates from the various shells surrounding the absorbing atom at the average distance R_j , as described in Chapter 2; the form of the EXAFS oscillation function is

$$\chi(k) = \sum_j \frac{N_j}{kR_j^2} \exp(-2\sigma_j^2 k^2) |F_j(\pi, k)| \exp(-2R_j/\lambda_j k) \\ \times \sin[2kR_j + \psi_j(k)]$$

It follows that information about interatomic distances, R_j , can be obtained from the Fourier transform of this expression. As was explained in Chapter 2, it is necessary to weight $\chi(k)$ to allow for damping of the oscillations at high k value. In the case of Al_2O_3 the appropriate weighting factor is k^3 and the smoothed weighted function $\chi(k) k^3$ is shown in figure 4.3.2. for the case of the anodic oxide formed in sodium tartrate. The window used to truncate the EXAFS oscillation function in this case, and all other cases to be described was placed between 2.8 and 8.0 \AA^{-1} . The Fourier transform of this is shown in figure 4.3.4. The peak at $R=0.148 \text{ nm}$ should correspond to the Al-O nearest-neighbour separation, but shifted towards the origin by the linear part of the phase shift. In order to determine the true interatomic distances in an unknown material, the phase shift must be identified, which can be done using a model compound as described previously in Chapter 2. Care is needed in making a correct choice of the energy of the X-ray absorption edge (E_0) otherwise errors in this can cause spurious phase shift due to the accompanying error in the k -scale. In the case of the reference material (sapphire) and all the anodic oxide films examined E_0 was chosen to be the energy corresponding to the half-height of the absorption edge, 1558 eV. The correctness of this choice of E_0 can be demonstrated by taking the back-Fourier transform of the Fourier transform of the EXAFS using a window to isolate the first nearest neighbour peak, to yield the sinusoidal contribution to the EXAFS in k -space due to the nearest neighbour shell of atoms, and then back-Fourier transforming this again to R -space. The result is shown in figure 4.3.3 where it can be seen that the

peak of the double back-Fourier transform coincides with that in the original forward Fourier transform. This means that the k-scale is correct, as a consequence of the correct choice of E_0 .

(v) The determination of Al-O bond length for the anodic oxide formed in sodium tartrate

The model compound chosen in this study is an α -alumina sample (sapphire specimen, see section 4.2.3.vi) for which the crystal structure is well known. All the aluminium atoms are bonded octahedrally to oxygen atoms with two distinct Al-O bond lengths, 0.186 nm and 0.197 nm (Wyckoff, 1964). Since the EXAFS gives only an average bond length, this should correspond to the average of these two values, i.e. 0.1915 nm. Since this model compound has the same chemical composition (Al_2O_3) as the anodic films the phase shift obtained by comparing the position of the strong peak in the Fourier transform with this average bondlength of 0.1915 nm should be directly transferable to the EXAFS results from the unknown structure.

The EXAFS oscillations for the model, shown in Figure 4.3.4 weighted by k^3 , were obtained from the normalised electron yield following the same procedure as that described already for the anodic oxide. The same window (2.8 - 8.0 \AA^{-1}) as that used for the anodic film was applied to obtain the Fourier transform for the α -alumina, shown in figure 4.3.5. This shows a large peak at 0.150 nm which should correspond to a Al-O bondlength of 0.192nm. Thus the phase shift for Al_2O_3 produces a shift in peak position of 0.042 nm. This can now be used to correct the Al-O peak position for the anodic films.

Figure 4.3.4

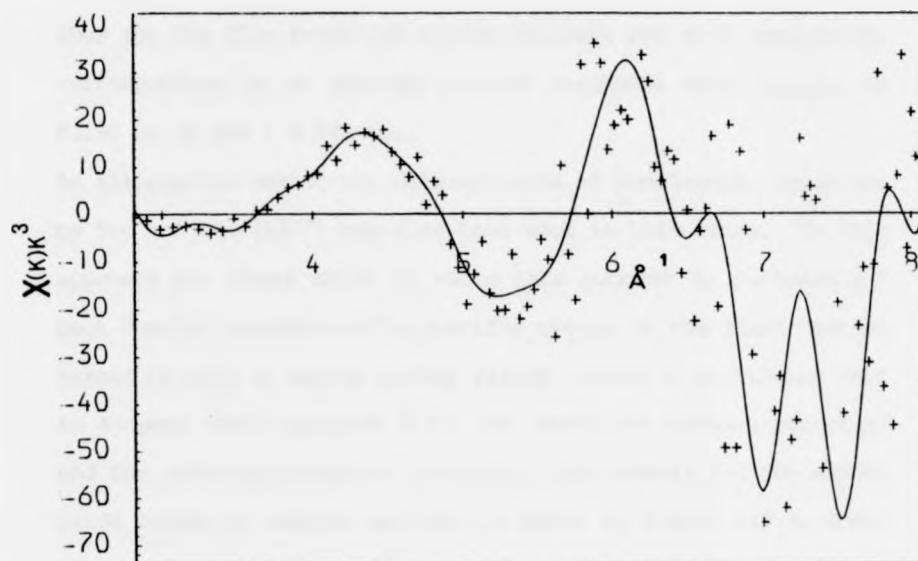


Figure 4.3.5

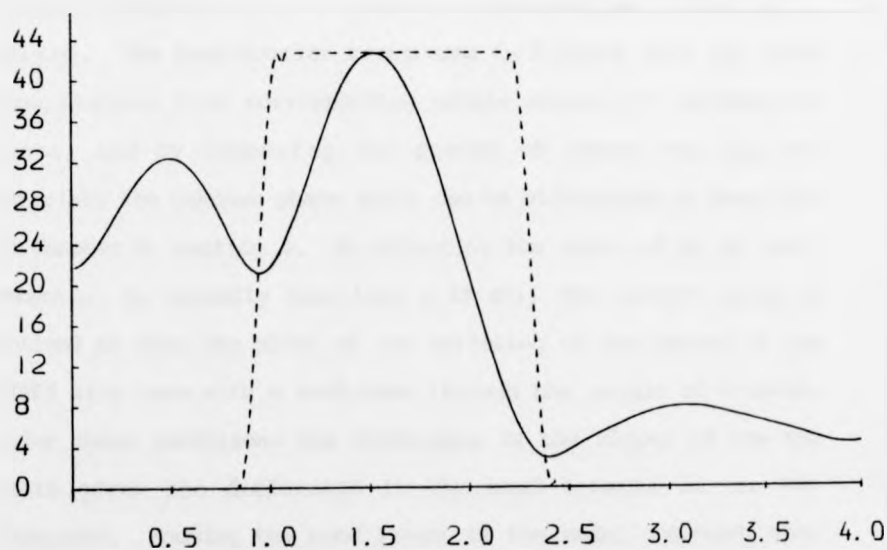


Figure 4.3.4. The EXAFS function $\chi(k)$ weighted by k^3 for the model compound (α - Al_2O_3 "sapphire specimen"). The crosses represent individual data points; the continuous line is the cubic spline fit used for the Fourier transform.

Figure 4.3.5. The Fourier transform of the EXAFS function shown in figure 4.3.4. The dashed line represents the window function placed around the first nearest neighbour.

Thus for the film formed in sodium tartrate the Al-O separation, corresponding to an average nearest neighbour bond length, is 0.190 nm (0.148 + 0.042 nm).

An alternative method for determination of bondlength, suggested by Teo and Lee (1977) has also been used in this study. In this approach the phase shift is taken into account by performing a back Fourier transform of a specific region of the first Fourier transform with a narrow window placed around a particular peak in R-space (see equation 2.11) for both the unknown structure and the reference material (α -Al₂O₃). The result for the anodic oxide formed in sodium tartrate is shown in figure 4.3.3, where the dashed line represents the window function and the dotted line shows the back-Fourier transform. Figure 4.3.5. shows a similar analysis of the data for the reference material (α -Al₂O₃). The back-Fourier transforms in K-space give the EXAFS contributions from corresponding single shells of neighbouring atoms, and by comparing the phases of these for the two materials the unknown phase shift can be eliminated as described in Chapter 2, section 4. By adjusting the value of E_0 by small amounts, E_0 (usually less than ± 10 eV), the correct value is arrived at when the plots of the variation of the phases of the EXAFS sine term with k both pass through the origin of k-space. Under these conditions the difference in the slopes of the two plots gives the difference in the bond lengths of the two materials. Knowing the bond length of the model compound, then the actual bondlength of the anodic oxide can be obtained. Using this method the difference in Al-O bondlengths for the reference material (α -Al₂O₃) and the anodic oxide

formed in sodium tartrate was found to be $\Delta R = -0.003$ nm. Therefore the bondlength of the anodic oxide is 0.189 nm (0.192 - 0.003 nm).

In conclusion therefore, it can be stated that allowing for errors in the analysis the two methods of bondlength determination result in nearly identical values (0.190 nm compared with 0.189 nm). In the next section the likely errors in these determinations will be evaluated.

(vi) Estimation of errors in the EXAFS determination of bondlength

The error in the measured Al-O bondlength arises from random errors in the data and systematic errors arising from the processing of the data. The main contribution to the random errors is due to the counting of the electron yield. This was reduced by averaging 10 scans of EXAFS spectra which resulted in curves such as figure 3.5.2. (curve 1) in which the uncertainty in the data points is less than 1 per cent. There is a further error in the EXAFS oscillation function which results from any imperfect fitting of the polynomial representing μ_0 . An upper limit to the overall random error in the EXAFS oscillation function is 2 per cent. The quality of the data is clearly represented by the close relationship between the data points and the smooth fitted curve shown in figure 4.3.2. The determination of Al-O bondlength is more strongly dependent on systematic errors arising from the choice of E_0 and the window limits used in the Fourier transforms. The influence of the choice of E_0 was investigated by noting the shift in the

nearest neighbour peak position in the Fourier transform when a range of values of E_0 ($\Delta E_0 = \pm 1, \pm 2, \pm 5 \text{ eV}$) is used. It was found that for very small values of ΔE_0 the shift in the peak is negligible but can be as large as $\pm 0.004 \text{ nm}$ when $\Delta E_0 = \pm 5 \text{ eV}$. Similarly the effect of the choice of window, within the range of 30 eV (lower limit) to between 200 and 250 eV (upper limit) was found to result in a spread of peak position of $\pm 0.002 \text{ nm}$. The aggregate of these two errors is therefore $\pm 0.0045 \text{ nm}$. However, the likely error will be considerably less than this because great care was taken to choose E_0 correctly (and the success of this can be seen in figure 4.3.3. which has already been discussed in the previous section) and also to use wide limits for the Fourier window. A reasonable estimate of the overall uncertainty in the measured Al-O bondlength is $\pm 0.0025 \text{ nm}$. This degree of accuracy is expected for measurements on all the oxides and oxy-hydroxides.

4.3.2. The EXAFS results for the oxide formed in sodium oxalate

The weighted EXAFS oscillation function, $\chi(k) k^3$, shown in figure 4.3.6i for the oxide formed in sodium oxalate was obtained from the electron yield spectra using the same procedure as that described in the previous section. The Fourier transform is given in figure 4.3.6ii. The window for the Fourier transform was placed between 2.8 \AA^{-1} and 8.5 \AA^{-1} . The large peak in the Fourier transform at $R = 0.143 \text{ nm}$ is the contribution from the Al-O nearest neighbour shell in the oxide. This is shifted towards the origin by 0.042 nm as a result of the phase shift. Therefore the average Al-O nearest neighbour bondlength is $0.185 \text{ nm} \pm 0.0025 \text{ nm}$.

nearest neighbour peak position in the Fourier transform when a range of values of E_0 ($\Delta E_0 = \pm 1, \pm 2, \pm 5 \text{ eV}$) is used. It was found that for very small values of ΔE_0 the shift in the peak is negligible but can be as large as $\pm 0.004 \text{ nm}$ when $\Delta E_0 = \pm 5 \text{ eV}$. Similarly the effect of the choice of window, within the range of 30 eV (lower limit) to between 200 and 250 eV (upper limit) was found to result in a spread of peak position of $\pm 0.002 \text{ nm}$. The aggregate of these two errors is therefore $\pm 0.0045 \text{ nm}$. However, the likely error will be considerably less than this because great care was taken to choose E_0 correctly (and the success of this can be seen in figure 4.3.3. which has already been discussed in the previous section) and also to use wide limits for the Fourier window. A reasonable estimate of the overall uncertainty in the measured Al-O bondlength is $\pm 0.0025 \text{ nm}$. This degree of accuracy is expected for measurements on all the oxides and oxy-hydroxides.

4.3.2. The EXAFS results for the oxide formed in sodium oxalate

The weighted EXAFS oscillation function, $\chi(k) k^3$, shown in figure 4.3.6i for the oxide formed in sodium oxalate was obtained from the electron yield spectra using the same procedure as that described in the previous section. The Fourier transform is given in figure 4.3.6ii. The window for the Fourier transform was placed between 2.8 \AA^{-1} and 8.5 \AA^{-1} . The large peak in the Fourier transform at $R = 0.143 \text{ nm}$ is the contribution from the Al-O nearest neighbour shell in the oxide. This is shifted towards the origin by 0.042 nm as a result of the phase shift. Therefore the average Al-O nearest neighbour bondlength is $0.185 \text{ nm} \pm 0.0025 \text{ nm}$.

Figure 4.3.6i

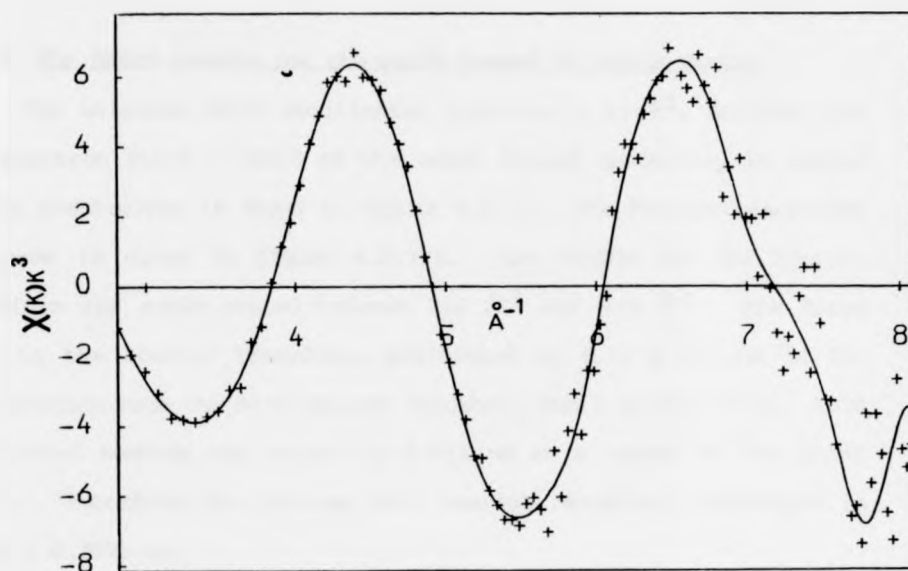


Figure 4.3.6ii

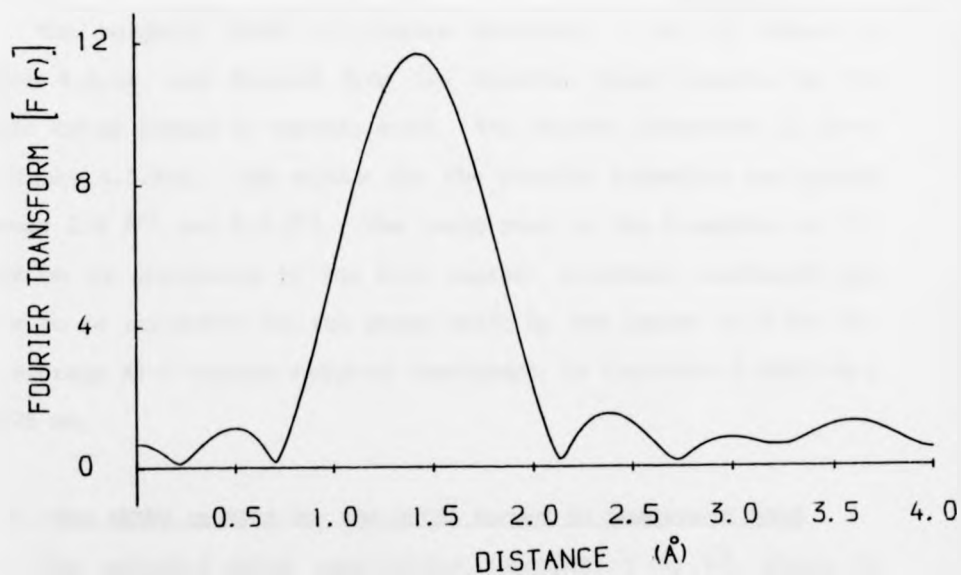


Figure 4.3.6i. The EXAFS function $\chi(k)$ weighted by k^3 for the sodium oxalate-formed oxide. The crosses represent individual data points; the continuous line is the cubic spline fit used for the Fourier transform.

Figure 4.3.6ii. The Fourier transform of the EXAFS function shown in figure 4.3.6i.

4.3.3. The EXAFS results for the oxide formed in sodium borate

The weighted EXAFS oscillation function, $\chi(k) k^3$, derived from the electron yield - EXAFS of the oxide formed anodically in sodium borate electrolyte is shown in figure 4.3.7i. The Fourier transforms of these is given in figure 4.3.7ii. The window for the Fourier transform are again placed between 2.8 \AA^{-1} and 8.5 \AA^{-1} . The large peak in the Fourier transform, positioned at $R = 0.147 \text{ nm}$ is the contribution from the Al-O nearest neighbour shell in the oxide. This is shifted towards the origin by 0.042 nm as a result of the phase shift. Therefore the average Al-O nearest neighbour bondlength is $0.190 \pm 0.0025 \text{ nm}$.

4.3.4. The EXAFS results for the oxide formed in chromic acid

The weighted EXAFS oscillation function, $\chi(k) k^3$, shown in figure 4.3.8i, was derived from the electron yield spectra of the anodic oxide formed in chromic acid. The Fourier transform is given in figure 4.3.8ii. The window for the Fourier transform was placed between 2.8 \AA^{-1} and 8.5 \AA^{-1} . The large peak in the transform at $R = 0.140 \text{ nm}$ is attributed to the Al-O nearest neighbour bondlength and needs to be corrected for the phase shift by the amount of 0.042 nm . The average Al-O nearest neighbour bondlength is therefore $0.1825 \text{ nm} \pm 0.0025 \text{ nm}$.

4.3.5. The EXAFS results for the oxide formed in phosphoric acid

The weighted EXAFS oscillation function, $\chi(k) k^3$, shown in figure 4.3.9i, derived from the electron yield spectra for the oxide formed anodically in phosphoric acid. The Fourier transform of this is given in figure 4.3.9ii. The window for the Fourier transform was

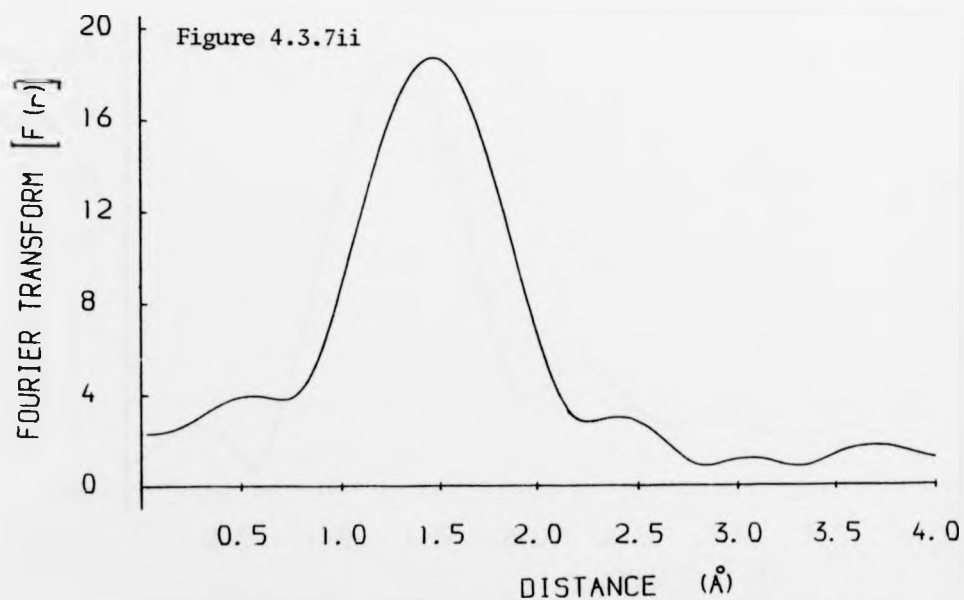
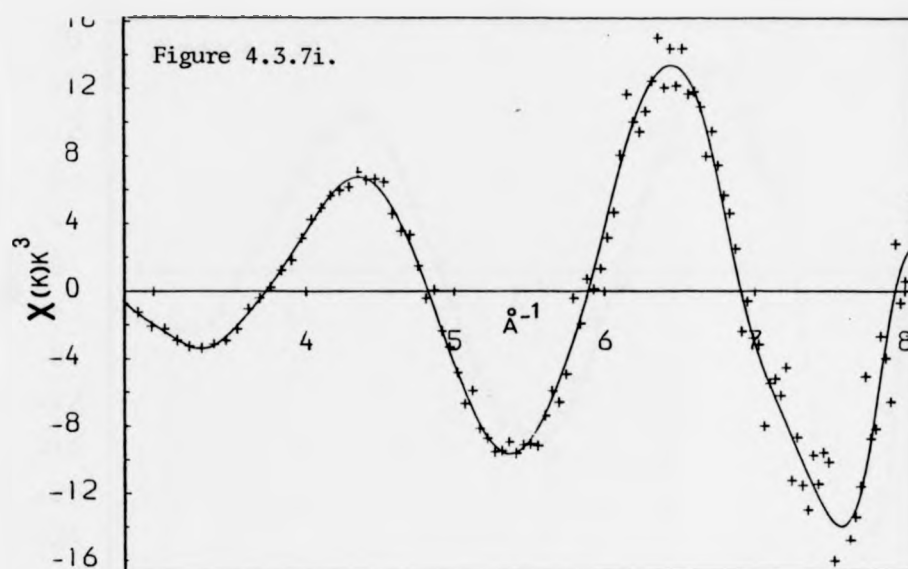


Figure 4.3.7i The EXAFS function $X(k)$ weighted by k^3 for the sodium borate-formed oxide. The crosses represent individual data-points; the continuous line is the cubic spline fit used for the Fourier transform.

Figure 4.3.7ii The Fourier transform of the EXAFS function shown in Figure 4.3.7i.

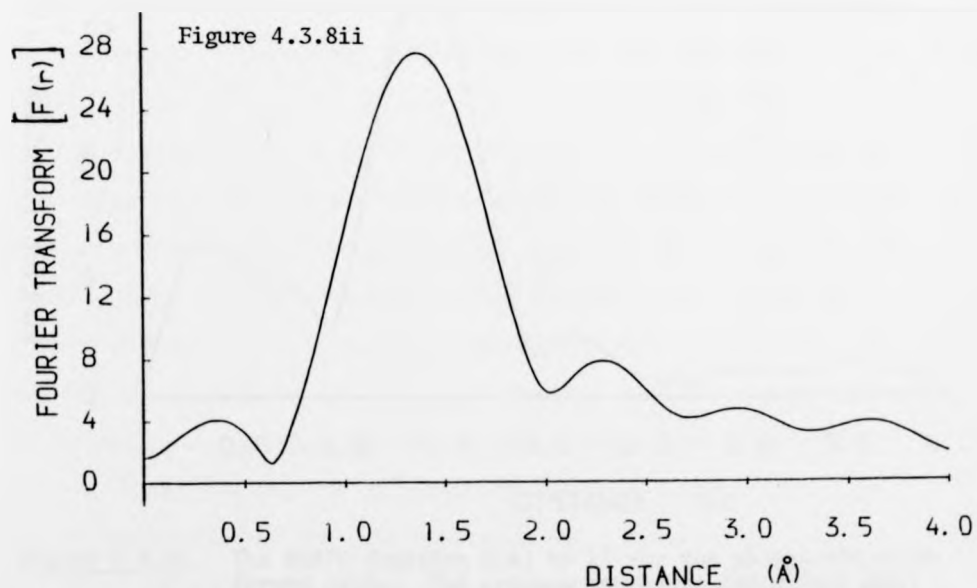
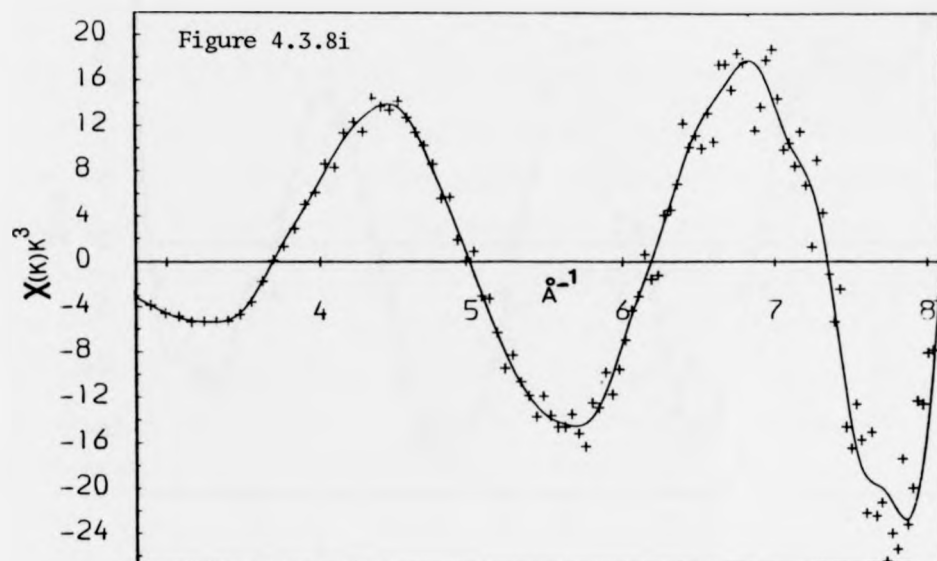


Figure 4.3.8i The EXAFS function $X(k)$ weighted by k^3 for the chromic acid-formed oxide. The crosses represent individual data points; the continuous line is the cubic spline fit used for the Fourier transform.

Figure 4.3.8ii The Fourier transform of the EXAFS function shown in Figure 4.3.8i.

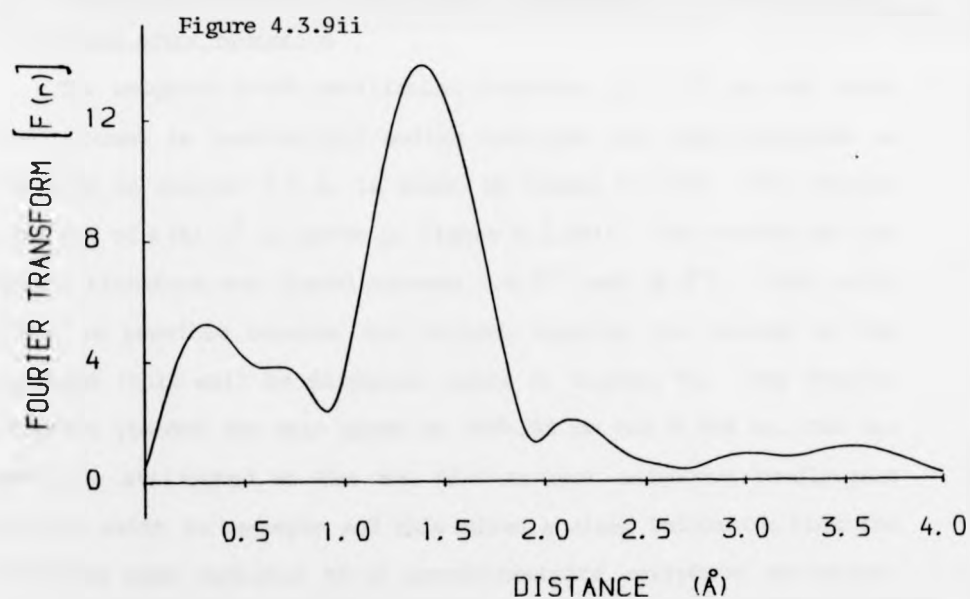
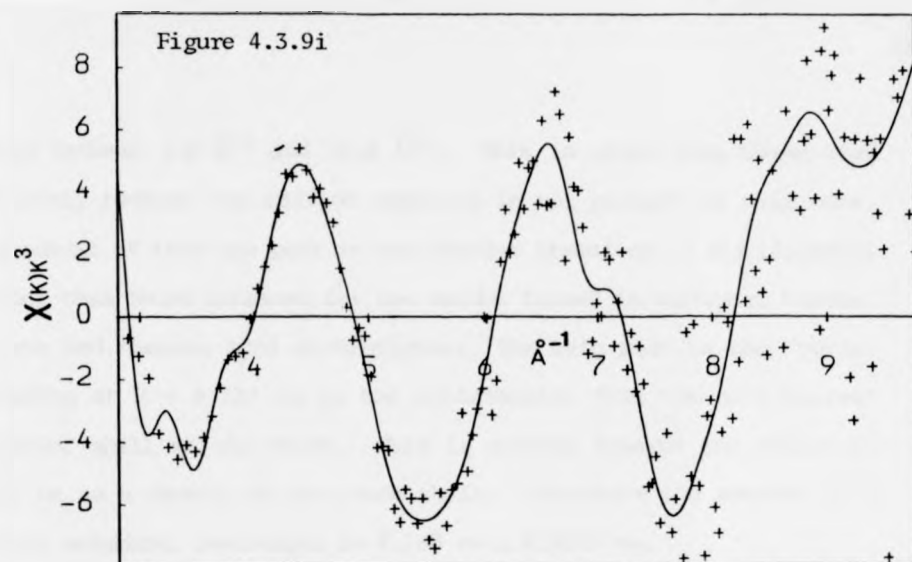


Figure 4.3.9i The EXAFS function $X(k)$ by k^3 for the phosphoric acid-formed oxide. The crosses represent individual data points; the continuous line is the cubic spline fit used for the Fourier transform.

Figure 4.3.9ii The Fourier transform of the EXAFS function shown in Figure 4.3.9i

placed between 2.8 \AA^{-1} and 10.0 \AA^{-1} . This is wider than those used previously because the silicon impurity is not present in this case. As a result of this the peak in the Fourier transform is significantly sharper than those obtained for the oxides formed in tartrate, borate, oxalate and chromic acid electrolytes. The main peak in the Fourier transform at $R = 0.138 \text{ nm}$ is the contribution from the Al-O nearest neighbour shell in the oxide. This is shifted towards the origin by 0.042 nm as a result of the phase shift. Therefore the average Al-O nearest neighbour bondlength is $0.180 \text{ nm} \pm 0.0025 \text{ nm}$.

4.3.6. The EXAFS results for the oxide film formed in sodium tartrate electrolyte after hydration

The weighted EXAFS oscillation function, $\chi(k) k^3$ for the oxide film, formed in neutralized sodium tartrate and then hydrated as described in section 4.2.4, is shown in figure 4.3.10i. The Fourier transform of $\chi(k) k^3$ is given in figure 4.3.10ii. The window for the Fourier transform was placed between 2.8 \AA^{-1} and 10 \AA^{-1} . This wider window is possible because the silicon impurity is removed by the hydration (this will be discussed later in Chapter 6). The Fourier transform yielded two main peaks at $R=0.165 \text{ nm}$ and 0.230 nm . The two peaks are attributed to the two Al-O nearest neighbour bondlengths known to exist in boehmite and this gives a clear indication that the oxide has been hydrated to a pseudo-boehmite amorphous structure. Since the scattering of the photoelectrons again involves primarily Al and O it is reasonable to assume the same shift of the peaks of 0.042 nm due to the phase shift. Therefore the average two Al-O bondlengths are $0.210 \pm 0.0025 \text{ nm}$ and $0.27 \text{ nm} \pm 0.0025 \text{ nm}$.

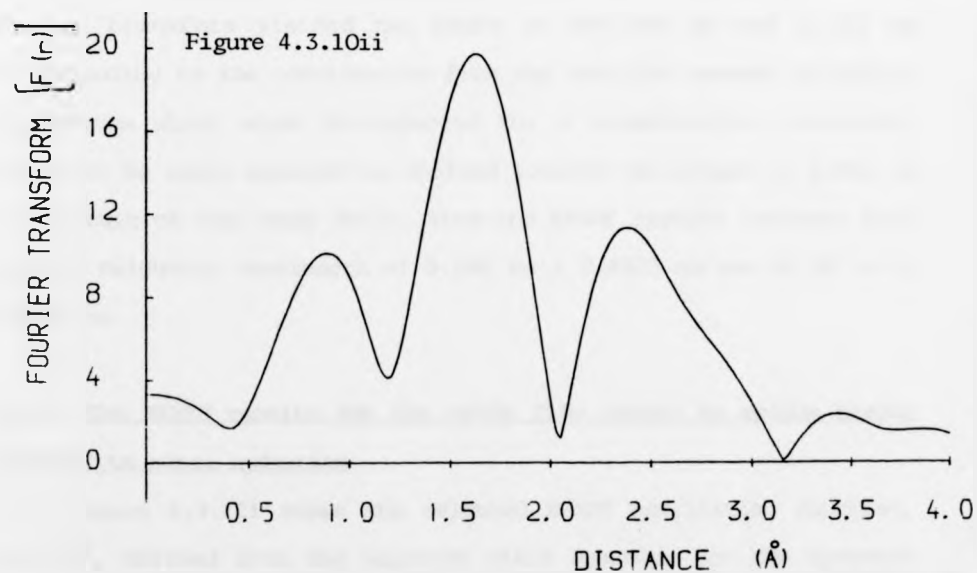
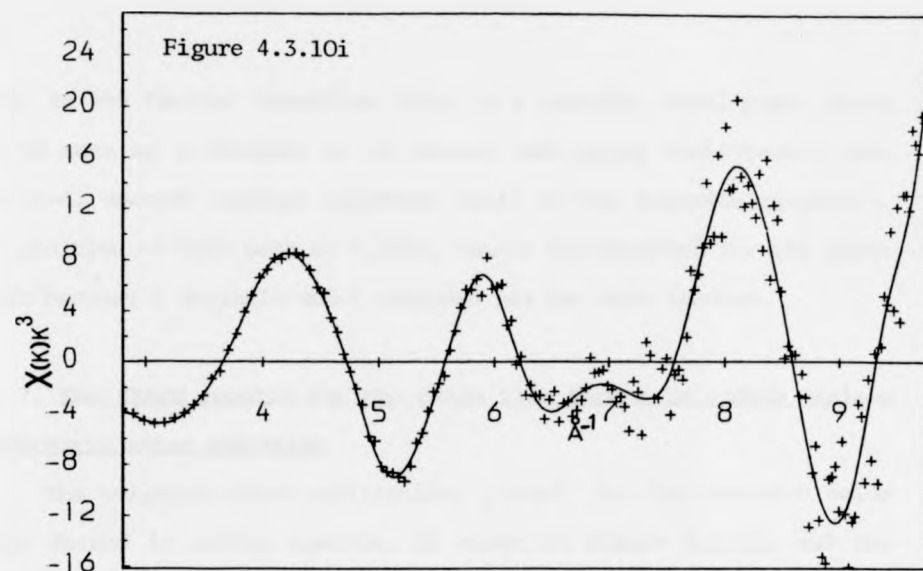


Figure 4.3.10i The EXAFS function $X(k)$ weighted by k^3 for the sodium tartrate formed oxide after immersion in water at 85°C for 30 minutes. The crosses represent individual data points; the continuous line is the cubic spline fit used for the Fourier transform.

Figure 4.3.10ii The Fourier transform of the EXAFS function shown in Figure 4.3.10i

Also, in the Fourier transform there is a possible third peak, which can be seen as a shoulder on the second peak which could result from the Al-Al second- nearest neighbour shell in the boehmite structure. The position of this peak at 0.25nm, cannot be corrected for the phase shift because a suitable model compound has not been studied.

4.3.7. The EXAFS results for the oxide film formed in sodium oxalate electrolyte after hydration

The weighted EXAFS oscillation, $\chi(k)k^3$, for the hydrated oxide film, formed in sodium oxalate, is shown in figure 4.3.11i and the Fourier transform is given in figure 4.3.11ii. The window for the Fourier transform was again placed between 2.8\AA^{-1} and 10\AA^{-1} . The Fourier transform yielded two peaks at $R=0.165\text{ nm}$ and 0.230 nm corresponding to the contribution from the two Al-O nearest neighbour bondlengths which might be expected for a boehmite-like structure. These can be again regarded as shifted towards the origin by 0.042 nm as a result of the phase shift. Thus the EXAFS results indicate Al-O nearest neighbour bondlength of $0.200\text{ nm} \pm 0.0025\text{ nm}$ and $0.280\text{ nm} \pm 0.0025\text{ nm}$.

4.3.8. The EXAFS results for the oxide film formed in sodium borate electrolyte after hydration

Figure 4.3.12i shows the weighted EXAFS oscillation function, $\chi(k) k^3$, derived from the electron yield spectrum for the hydrated oxide formed in neutralised sodium borate. The Fourier transform of this is given in figure 4.3.12ii. The window for the Fourier transform was placed between 2.8\AA^{-1} and 9.5\AA^{-1} . The Fourier transform of this exhibits two peak, at $R=0.164\text{ nm}$ and 0.252 nm , again

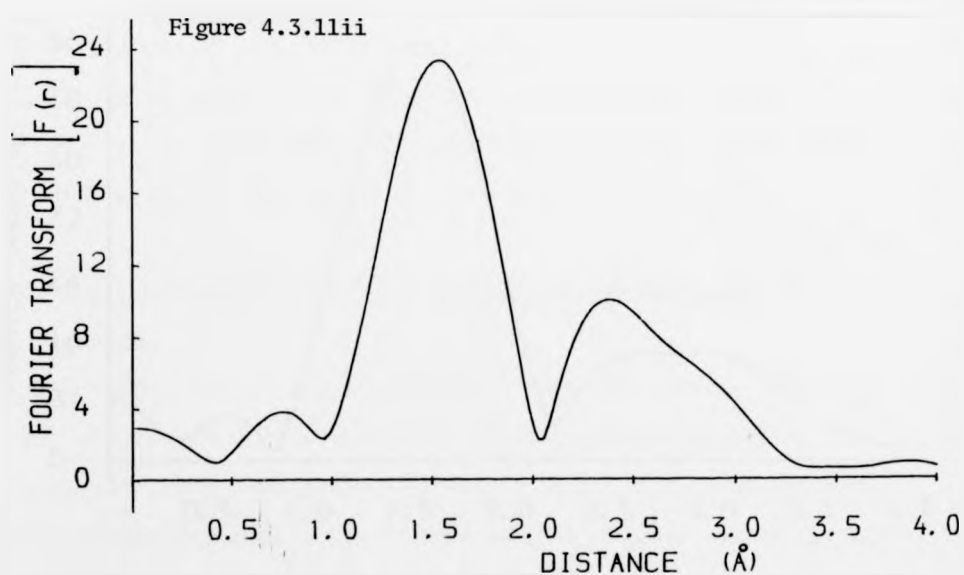
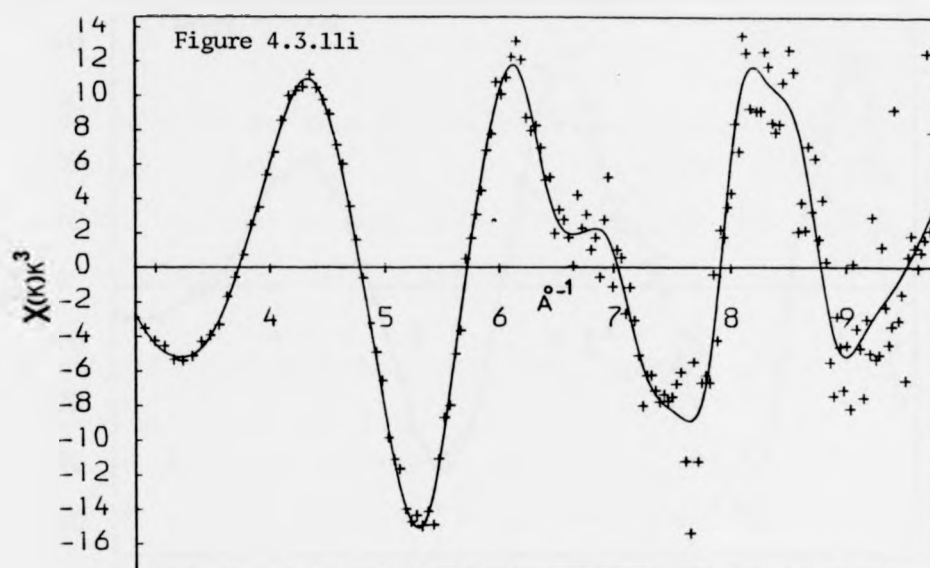


Figure 4.3.11i The EXAFS function $X(k)$ weighted by k^3 for the oxide formed in sodium oxalate after immersion in water at 85°C for 30 minutes. The crosses represent individual data points; the continuous line is the cubic spline fit used for the Fourier transform.

Figure 4.3.11ii The Fourier transform of the EXAFS function shown in Figure 4.3.11i.

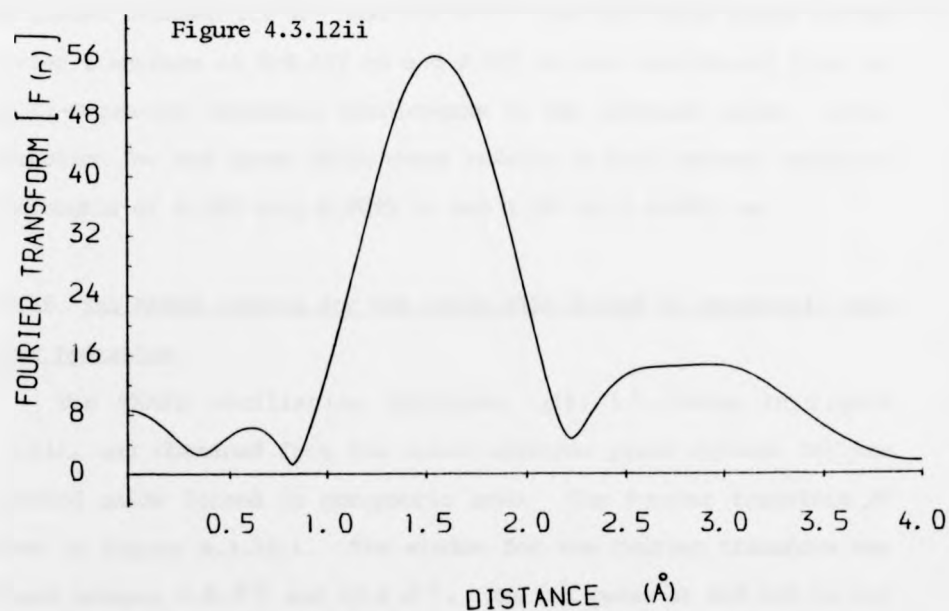
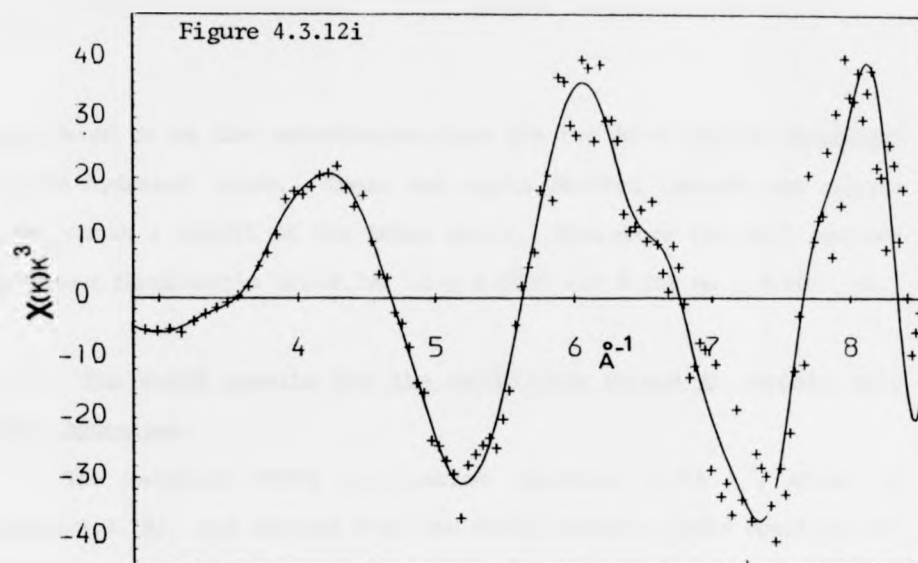


Figure 4.3.12i The EXAFS function $X(k)$ weighted by k^3 for the sodium borate-formed oxide film after immersion in water at 85°C for 30 minutes. The crosses represent the individual data points; the continuous line is the cubic spline fit for the Fourier transform.

Figure 4.3.12ii The Fourier transform of the EXAFS function shown in Figure 4.3.12i.

considered to be the contribution from the two Al-O nearest neighbour in the hydrated oxide. These are again shifted towards the origin 0.042 nm as a result of the phase shift. Therefore the Al-O nearest neighbour bondlengths are 0.200 nm \pm 0.0025 and 0.290 nm \pm 0.0025 nm.

4.3.9. The EXAFS results for the oxide film formed in chromic acid after hydration

The weighted EXAFS oscillation function, $\chi(k) k^3$, shown in figure 4.3.13i, was derived from the total electron yield spectrum for the hydrated oxide formed in chromic acid. The Fourier transform of this is given in figure 4.3.13ii. The window for the Fourier transform was placed between 2.8 \AA^{-1} and 9.5 \AA^{-1} . The two large peaks in the Fourier transform at $R=0.163$ nm and 0.237 nm are contributed from the two Al-O nearest neighbour bondlengths in the hydrated oxide. After correction for the phase shift these results in Al-O nearest neighbour bondlengths of 0.205 nm \pm 0.0025 nm and 0.280 nm \pm 0.0025 nm.

4.3.10. The EXAFS results for the oxide film formed in phosphoric acid after hydration

The EXAFS oscillation function, $\chi(k) k^3$, shown in figure 4.3.14i, was obtained from the total electron yield spectra for the hydrated oxide formed in phosphoric acid. The Fourier transform is given in figure 4.3.14ii. The window for the Fourier transform was placed between 2.8 \AA^{-1} and 10.0 \AA^{-1} . The two peaks at $R=0.168$ nm and 0.238 nm are the contribution from the Al-O nearest neighbour bondlengths in the hydrated oxide. These are shifted towards the origin by 0.042 nm as a result of the phase shift. Therefore the

considered to be the contribution from the two Al-O nearest neighbour in the hydrated oxide. These are again shifted towards the origin 0.042 nm as a result of the phase shift. Therefore the Al-O nearest neighbour bondlengths are 0.200 nm \pm 0.0025 and 0.290 nm \pm 0.0025 nm.

4.3.9. The EXAFS results for the oxide film formed in chromic acid after hydration

The weighted EXAFS oscillation function, $\chi(k) k^3$, shown in figure 4.3.13i, was derived from the total electron yield spectrum for the hydrated oxide formed in chromic acid. The Fourier transform of this is given in figure 4.3.13ii. The window for the Fourier transform was placed between 2.8 \AA^{-1} and 9.5 \AA^{-1} . The two large peaks in the Fourier transform at $R=0.163$ nm and 0.237 nm are contributed from the two Al-O nearest neighbour bondlengths in the hydrated oxide. After correction for the phase shift these results in Al-O nearest neighbour bondlengths of 0.205 nm \pm 0.0025 nm and 0.280 nm \pm 0.0025 nm.

4.3.10. The EXAFS results for the oxide film formed in phosphoric acid after hydration

The EXAFS oscillation function, $\chi(k) k^3$, shown in figure 4.3.14i, was obtained from the total electron yield spectra for the hydrated oxide formed in phosphoric acid. The Fourier transform is given in figure 4.3.14ii. The window for the Fourier transform was placed between 2.8 \AA^{-1} and 10.0 \AA^{-1} . The two peaks at $R=0.168$ nm and 0.238 nm are the contribution from the Al-O nearest neighbour bondlengths in the hydrated oxide. These are shifted towards the origin by 0.042 nm as a result of the phase shift. Therefore the

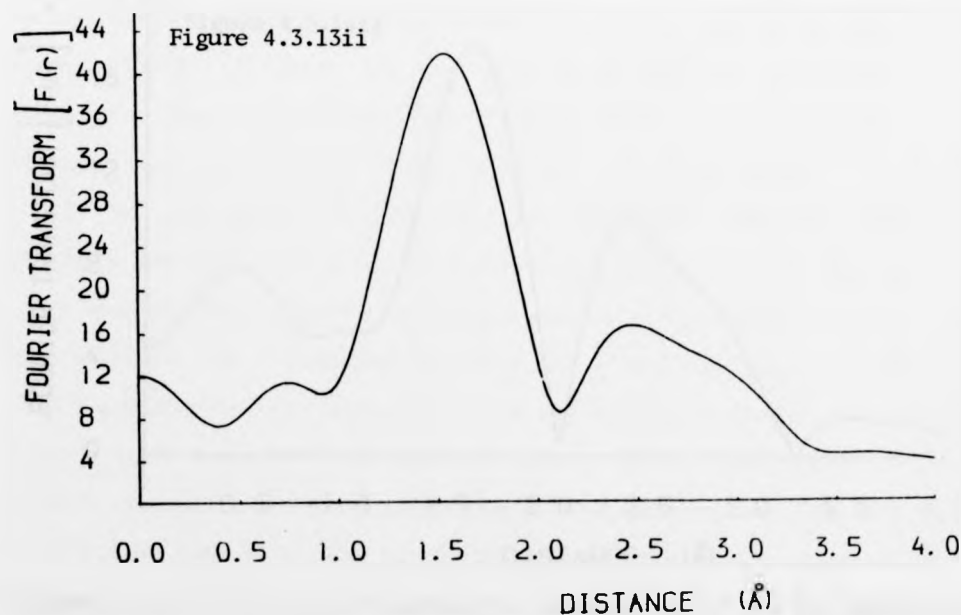
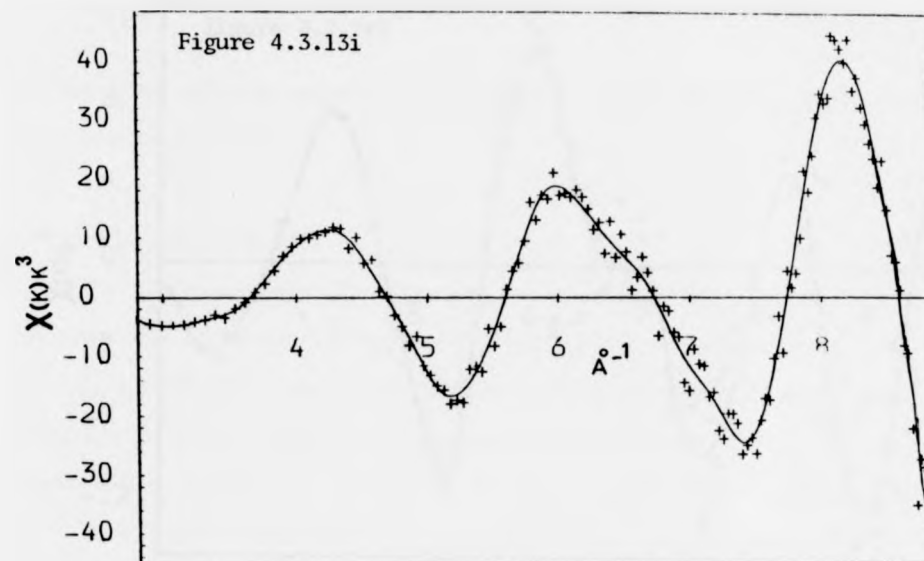


Figure 4.3.13i The EXAFS function $X(k)$ weighted by k^3 for the chromic acid-formed oxide after immersion in water at 85°C for 4 hours. The crosses represent individual data points; the continuous line is the cubic spline used for the Fourier transform.

Figure 4.3.13ii The Fourier transform of the EXAFS function shown in Figure 4.3.13i.

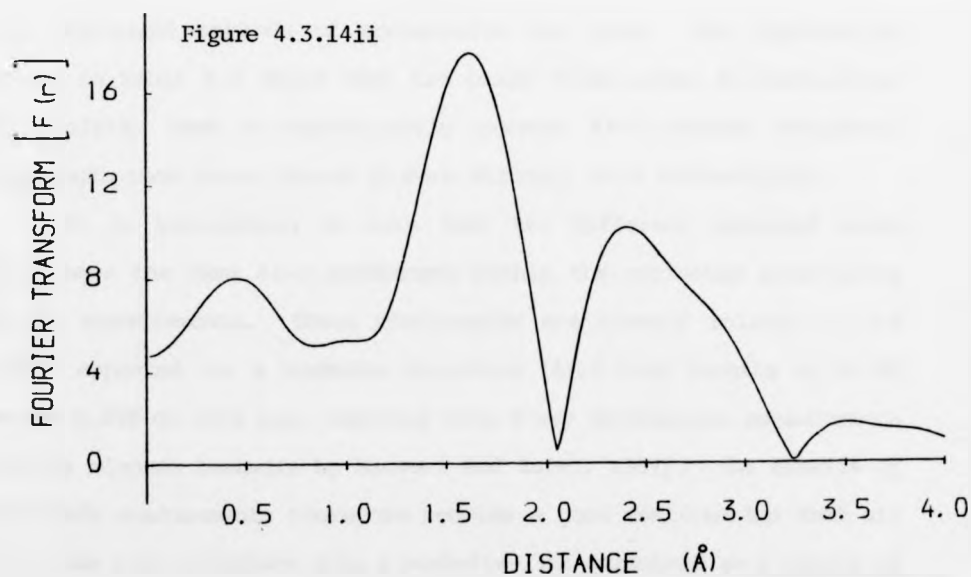
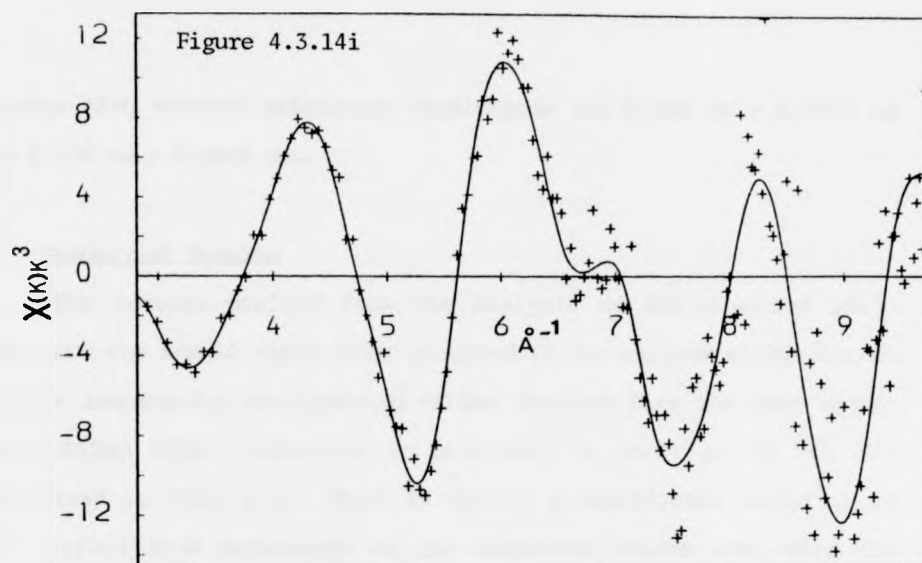


Figure 4.3.14i The EXAFS function $X(k)$ weighted by k^3 for the phosphoric acid-formed oxide after immersion in water at 85°C for 4 hours. The crosses represent individual data points; the continuous line is the cubic spline fit used for the Fourier transform.

Figure 4.3.14ii The Fourier transform of the EXAFS function shown in Figure 4.3.14i.

average Al-O nearest neighbours bondlengths are $0.200 \text{ nm} \pm 0.0025 \text{ nm}$ and $0.280 \text{ nm} \pm 0.0025 \text{ nm}$.

4.4. Summary of Results

The results derived from the analysis of the electron yield EXAFS for the anodic oxide films prepared in the various electrolytes, and the results for the hydrated oxides obtained from the same anodic oxide films after hydration by immersion in water at 85°C , are summarised in Table 4.4. There is clearly a significant variation in the derived Al-O bondlength of the different oxides even when the uncertainty in the measured values of the Al-O bondlength is taken into account. This reflects the variation of the molecular structure when different methods of preparation are used. The bondlengths listed in Table 4.4 shows that the oxide films grown in neutralized electrolytes have a significantly greater Al-O nearest neighbour bondlength than those formed in more strongly acid electrolytes.

It is interesting to note that the different hydrated oxide films have the same Al-O bondlength within the estimated uncertainty in the measurements. These bondlengths are closely related to the values expected for a boehmite structure (Al-O bond lengths of 0.190 nm and 0.250 nm have been reported from X-ray diffraction measurements for the mineral boehmite by Sasvari and Zalai, 1957). The results of the EXAFS measurements therefore provide a good confirmation that all the oxide film transform into a boehmite-like structure as a result of hydration.

The measured bondlength for as-formed oxides agree quite closely with some values reported by other workers and this will be discussed in greater detail in Chapter 6. The EXAFS results for the various

oxides will be discussed at that stage in terms of the known structures of α - and γ -alumina. It will be shown that this permits a useful description of the amorphous structure in terms of the two states of Al-O coordination (tetrahedrally and octahedrally bonded Al states) known to exist in the crystalline structure of Al_2O_3 . This approach will then be used to establish a possible model for amorphous alumina and to give an indication of the structure changes involved in hydration.

TABLE 4.4

Electrolyte solution	Measured Bond Length (nm)		
	Oxide	Hydrated Oxide	
Sodium tartrate	0.190 ± 0.0025	0.210 ± 0.0025	0.270 ± 0.0025
Sodium borate	0.190 ± 0.0025	0.210 ± 0.0025	0.295 ± 0.0025
Sodium oxalate	0.185 ± 0.0025	0.205 ± 0.0025	0.280 ± 0.0025
Chromic Acid	0.1825 ± 0.0025	0.205 ± 0.0025	0.280 ± 0.0025
Phosphoric Acid	0.180 ± 0.0025	0.205 ± 0.0025	0.280 ± 0.0025
α -Al ₂ O ₃ (corundum)*	0.1915		
Boehmite**		0.188	0.251

* average Al-O bond length reported by Wyckoff (1964)

** Al-O bond length reported by Sas vari and Zalai (1957)

REFERENCES

1. Ahearn, J.S., (1983), private communication.
2. Ahearn, J.S., Sun, T.S., Froede, C., Venables, J.D., Hopping, R., (1980), SAMPE Quarterly, Vol. 12.
3. Alwitt, R.S., (1984), private communication.
4. Davis, G.D., Sun, T.S., Ahearn, J.S., Venables, J.D., (1982), J. Mat. Science, 17, 1807.
5. El-Mashri, S.M., Forty, A.J., Freeman, L.A., and Smith, D.J., (1981), Electron Microscopy and Analysis, edited by M.J. Gorringer, Inst. Phys. Conf. Ser. No. 61 (Bristol and London: The Institute of Physics), p.395.
6. El-Mashri, S.M., Jones, R.G. and Forty, A.J., (1983), Phil. Mag. A. 48, 665.
7. Hunter, M.S. and Fowle, P., (1954), J. Electrochem. Soc., 110, 1205.
8. Lee, P.A. and Beni, G., (1977), Phys. Rev. B15, 2862.
9. Sas vari, K., Zalai, A., (1957), Acta. Geological Academy of Science Hungary, 4, 415.
10. Teo, B.K., and Beni, P.A., (1978), J. Amer. Chem. Soc., 101, 2815.
11. Thompson, G.E., and Wood, G.C., (1981), Nature, 290, 230.
12. Venables, J.D., McNamara, D.K., Chen, J.M., Sun, T.S., Hopping, R.L. (1979), Application of Surf. Sci., 3, 88.
13. Wyckoff, R.W.G., (1964), Crystal Structures, Second edition, (New York: Wiley).

CHAPTER 5
MICROMORPHOLOGICAL OBSERVATIONS OF THE ANODIC-OXIDE AND HYDRATED
OXIDE FILMS

5.1. Introduction

High resolution scanning transmission electron microscopy (STEM) has proved to be a great asset in studying and understanding micromorphology, and in following characteristic changes in materials. A JEOL JEM 100 CX transmission electron microscope, equipped with STEM and operated at 30 kV in the SEM mode using the secondary electron emission, was used to study the morphology of the oxide film formed anodically on pure aluminium in the different electrolyte solutions described in the previous chapter. The electron microscope was also fitted with an energy-dispersive X-ray microanalyser (EDAX), which could be used to obtain a qualitative chemical analysis of certain features in the surface oxide films.

A major problem in using SEM to study non-conducting specimens such as oxide-coated metals is the loss of image quality due to electrical charging of the sample during observation. A technique devised to overcome this problem by applying a very thin surface coating of platinum will be discussed and the use of this in high resolution SEM studies of the oxides and hydrated oxides already studied in the EXAFS experiments will be presented. These observations have proved to be particularly useful in the interpretation of the EXAFS results in relation to the process of hydration.

5.2. The surface coating technique

High quality SEM images are generally difficult to obtain from

oxidised surfaces because of the problems of electrical charging referred to earlier. These can be overcome by decorating the surface with a very thin film of highly conducting material. Although a thin conducting coating can be produced by evaporation of metal from a heated filament such a method has several disadvantages when applied to high resolution microscopic studies. The most serious problem is the lack of control over the thickness of the coating. In order to retain the required high spatial resolution the coating should be as thin as possible whilst providing a conducting path to earth. It has been found in the course of this and other studies of anodised surfaces that a more satisfactory method of coating the surface can be obtained by using an ion-beam sputter deposition technique. This was first demonstrated by Venables et. al (1979) and later by El-Mashri, Forty and Jones (1983). The results described in this Chapter have been obtained by using a technique developed in our laboratory using a small ion-beam gun (supplied by Ion Tech) which directs a beam of platinum vapour from a platinum metal target. The ion gun is highly controllable and it has been found possible to deposit films of only a few nm thickness in this way. Various materials can be deposited in this manner, including carbon, gold, gold-palladium, platinum-palladium but pure platinum has been found to be entirely satisfactory.

5.3. ~~SEM~~ Observations

Two similar sets of samples of the non-porous oxide films, formed anodically in sodium tartrate, sodium oxalate and sodium borate, were prepared at 35 volts, using the surface treatment procedure described in Chapter 4. These films were 50 nm thick. One set of specimens was kept in the as-formed condition while the other

set was hydrated by immersion in hot water at 85°C for 30 minutes.

Two similar sets of porous oxide samples were prepared in phosphoric acid and chromic acid, again using the procedures described in Chapter 4. One set of specimens was kept in the as-prepared condition, and the other set hydrated by immersion in hot water at 85°C for 4 hours.

5.3.1. Micromorphological observations of the oxide and hydrated oxide formed in sodium tartrate solution

An SEM image of the thin non-porous oxide layer formed in sodium tartrate electrolyte, using a pyrex glass container (borosilicate beaker), is represented by the micrograph in figure 5.3.1a. The morphology of the film is characteristically structureless, apart from the occurrence of isolated large particles of more strongly electron-emitting material. The scanning electron micrograph in Figure 5.3.1b shows an enlarged image of such a particle, approximately $10\mu\text{m}$ in diameter, attached to the oxidized surface. The energy dispersive X-ray spectra (EDAX) accompanying the micrograph show that, whilst there is no detectable silicon in the oxide film itself, there is a significant accumulation within the volume of the particle. The Al $K\alpha$ -line is also present in the EDAX spectrum from the particle, which probably arises from the oxide film beneath the particle. This is not surprising since the penetration depth for the 30 kV electron beam is quite large. Consequently the technique is not very surface sensitive. This siliceous impurity is thought to originate from the pyrex glass container, silicon being leached from the pyrex during the anodizing treatment. The particles are thought to be the result of a colloid formation in the neutralised sodium tartrate solution. This will be discussed more fully in the next chapter.



Figure 5.3.1a.

SEM image of a 50 nm uniform non-porous (barrier-type) oxide formed anodically on pure aluminium in sodium tartrate, coated with 3nm of platinum.



Figure 5.3.1a.

SEM image of a 50 nm uniform non-porous (barrier-type) oxide formed anodically on pure aluminium in sodium tartrate, coated with 3nm of platinum.



Figure 5.3.1b:

SEM image and EDAX spectra for an oxide formed in sodium tartrate electrolyte. Note the occurrence of a silicon peak in the EDAX spectrum of the particle



Figure 5.3.1b:

SEM image and EDAX spectra for an oxide formed in sodium tartrate electrolyte. Note the occurrence of a silicon peak in the EDAX spectrum of the particle

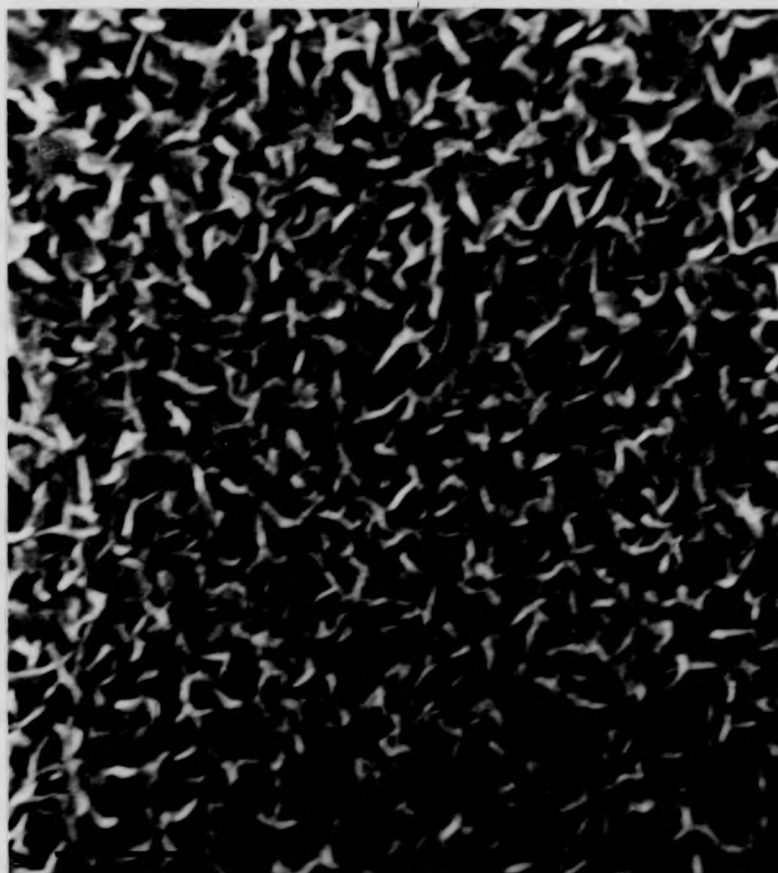


Figure 5.3.1c

SEM image of the same sodium tartrate formed oxide (Fig. 5.3.1a) after hydration at 85°C for 30 minutes. The "cornflake" structure has been revealed by a thin coating (3 nm) of platinum.

Figure 5.3.1d

Schematic representation of the oxy-hydroxide morphology (after Venables et al. 1980).

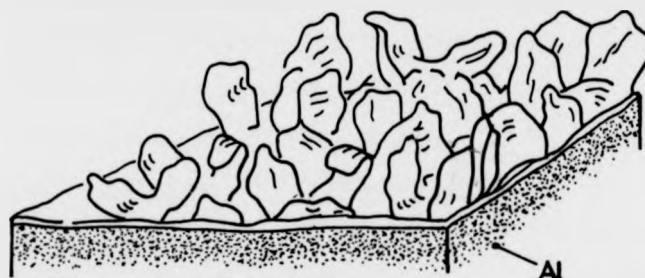
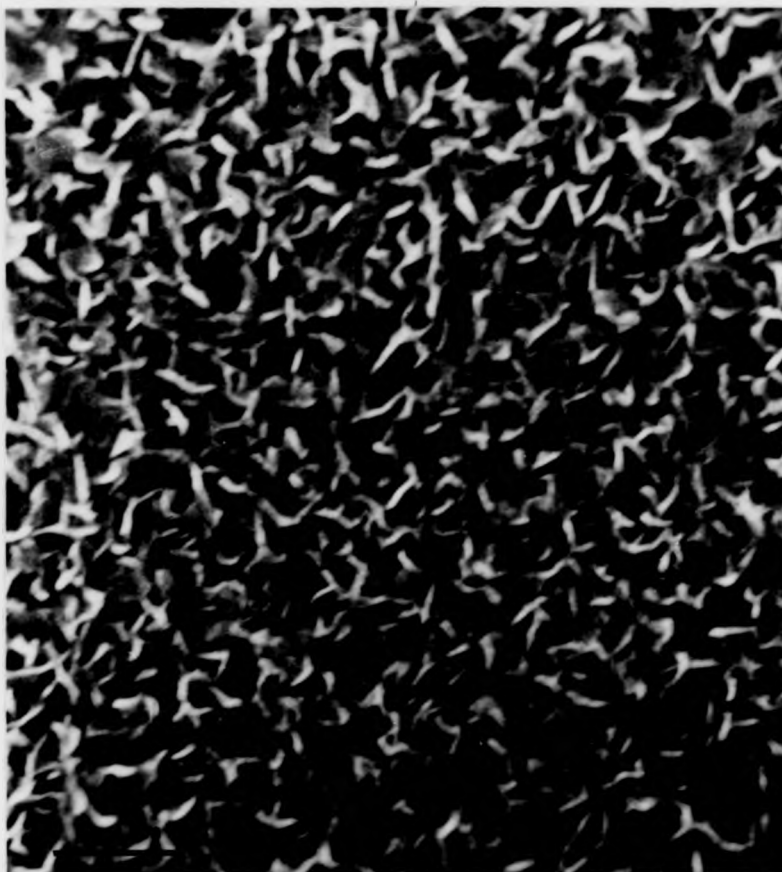


Figure 5.3.1c

SEM image of the same sodium tartrate formed oxide (Fig. 5.3.1a) after hydration at 85°C for 30 minutes. The "cornflake" structure has been revealed by a thin coating (3 nm) of platinum.

Figure 5.3.1d

Schematic representation of the oxy-hydroxide morphology (after Venables et al. 1980).

The morphology of the oxide film changes dramatically as a result of hydration, as can be seen from figure 5.3.1c. This shows what has been described by Venables et al (1979) as a "Cornflake" morphology consisting of discrete irregularly shaped platelets. The uniform, non-porous oxide film has been transformed to the hydrated phase with this new morphology. This confirms the results obtained from the EXAFS measurements described in Chapter 4, that the oxide is converted to a boehmite-like structure. It has been suggested previously by Venables et al (1980) that the new morphology consists of flakes of pseudo-boehmite, which is thought to be amorphous. A schematic of the new morphology is given in figure 5.3.1d (after Venables et al, 1980). It is noteworthy that the particles of siliceous impurity are absent from the hydrated oxide. This is consistent with the EXAFS observations for such films which show the complete removal of the Si absorption peak after hydration.

5.3.2. Micromorphological observations of the oxide and hydrated-oxide formed in sodium oxalate solution

Figure 5.3.2a shows the SEM image of the thin non-porous oxide layer, formed on pure aluminium in sodium oxalate electrolyte. An extensive search by scanning electron microscopy and X-ray microanalysis, showed that the film is uniform and structureless, similar to the film formed in sodium tartrate. Since this type of film was formed using an aluminium container for the electrolyte there is no significant siliceous impurity. This is already evident from the EXAFS spectrum for the oxide formed in sodium oxalate. The morphology of this oxide layer again changes significantly during immersion in hot water as shown in figure 5.3.2b. The cornflake



Figure 5.3.2a.

SEM image of a 50 nm uniform non-porous type oxide formed anodically on pure aluminium in sodium oxalate, coated with 3 nm of platinum.



Figure 5.3.2a.

SEM image of a 50 nm uniform non-porous type oxide formed anodically on pure aluminium in sodium oxalate, coated with 3 nm of platinum.

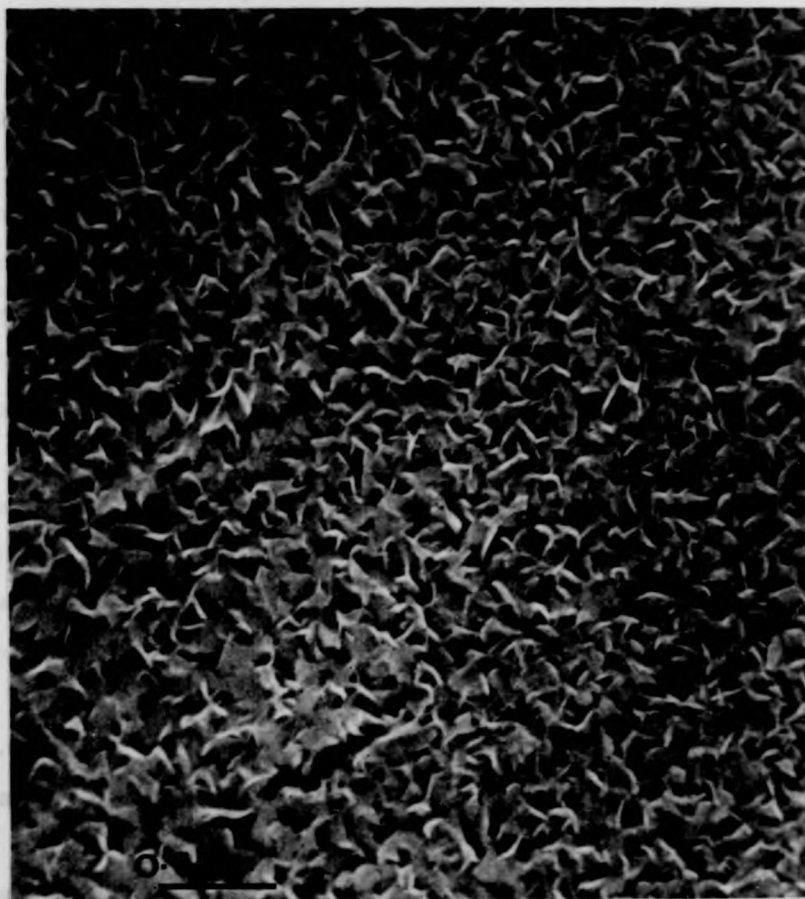


Figure 5.3.2b

SEM image of the same sodium oxalate-formed oxide (Fig. 5.3.2a) after hydration at 85°C for 30 minutes. The "cornflake" structure has been revealed by a thin coating (3 nm) of platinum.



Figure 5.3.2b

SEM image of the same sodium oxalate-formed oxide (Fig. 5.3.2a) after hydration at 85°C for 30 minutes. The "cornflake" structure has been revealed by a thin coating (3 nm) of platinum.

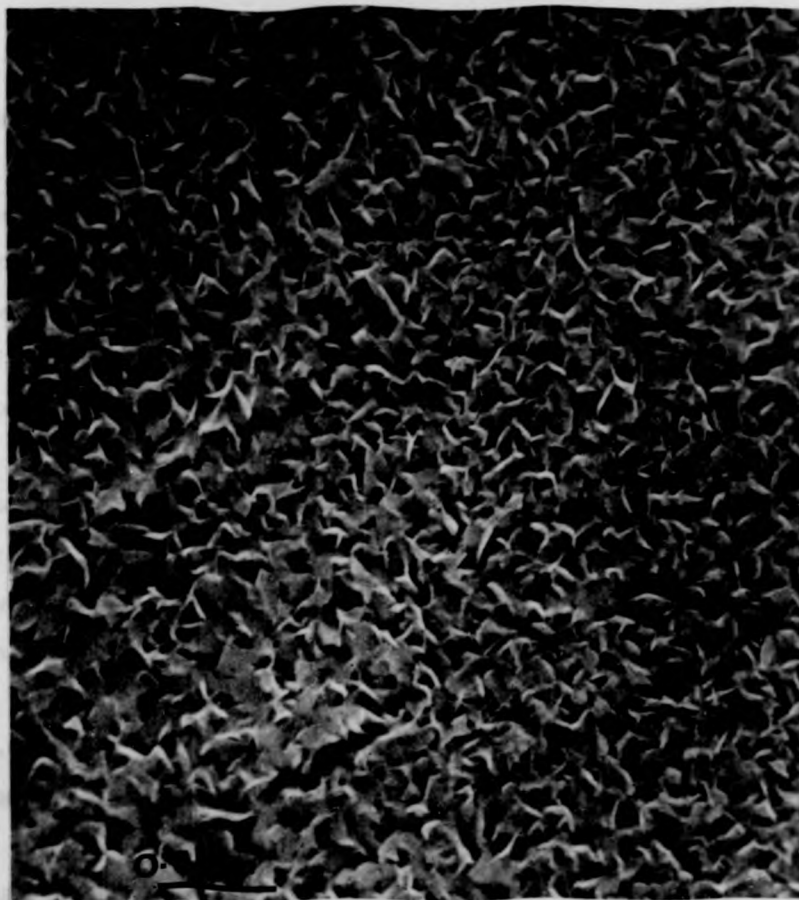


Figure 5.3.2b

SEM image of the same sodium oxalate-formed oxide (Fig. 5.3.2a) after hydration at 85°C for 30 minutes. The "cornflake" structure has been revealed by a thin coating (3 nm) of platinum.

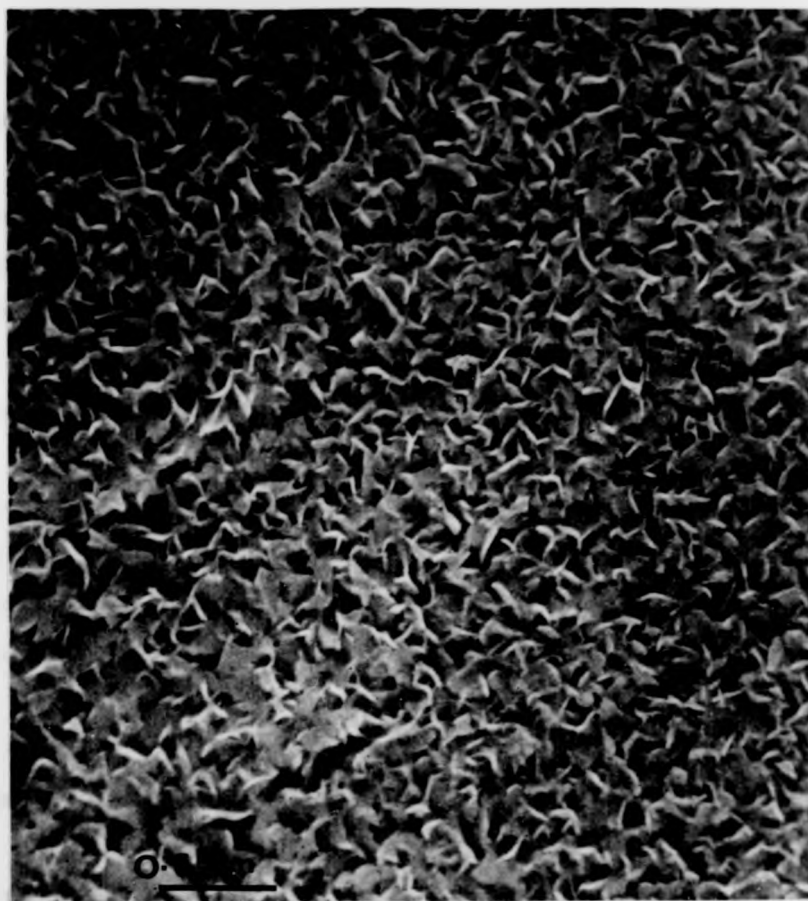


Figure 5.3.2b

SEM image of the same sodium oxalate-formed oxide (Fig. 5.3.2a) after hydration at 85°C for 30 minutes. The "cornflake" structure has been revealed by a thin coating (3 nm) of platinum.

morphology occurs on a slightly finer scale than in the case of the film formed in sodium tartrate and there is a suggestion that parts of the original oxide film have not been fully transformed during hydration.

5.3.3. Micromorphological observations of the oxide and hydrated-oxide formed in sodium borate solution

The morphology of the non-porous oxide layer grown anodically on aluminium in neutral sodium borate solution, observed by scanning electron microscopy is shown in figure 5.3.3a. The SEM image again shows the film to be a uniform oxide layer, covering the entire surface. The oxide morphology appears similar to that of the films prepared in sodium tartrate and sodium oxalate solutions.

When the specimen is immersed in hot water for 30 minutes to cause hydration, the morphology of the film changes again to the characteristic cornflake appearance as can be seen from the SEM image shown in figure 5.3.3b. In this case the cornflake structure has an even finer scale and appears to be fully developed.

5.3.4. Micromorphological observations of the oxide and hydrated oxide formed in phosphoric acid solution

The oxide film formed on the aluminium substrate by anodizing in phosphoric acid electrolyte has interesting micromorphological features. The film appears generally porous as shown in figure 5.3.4a. This indicates that the oxide consists of a shallow cellular structure with a cell diameter of about 40 nm and the cell walls are approximately 8 nm thick. This structure is less pronounced than that found by Venables et al (1979) which might be the result of different



Figure 5.3.3a.

SEM image of a 50 nm uniform non-porous type oxide formed anodically on pure aluminium in sodium borate, coated with 3 nm of platinum.



Figure 5.3.3a.

SEM image of a 50 nm uniform non-porous type oxide formed anodically on pure aluminium in sodium borate, coated with 3 nm of platinum.

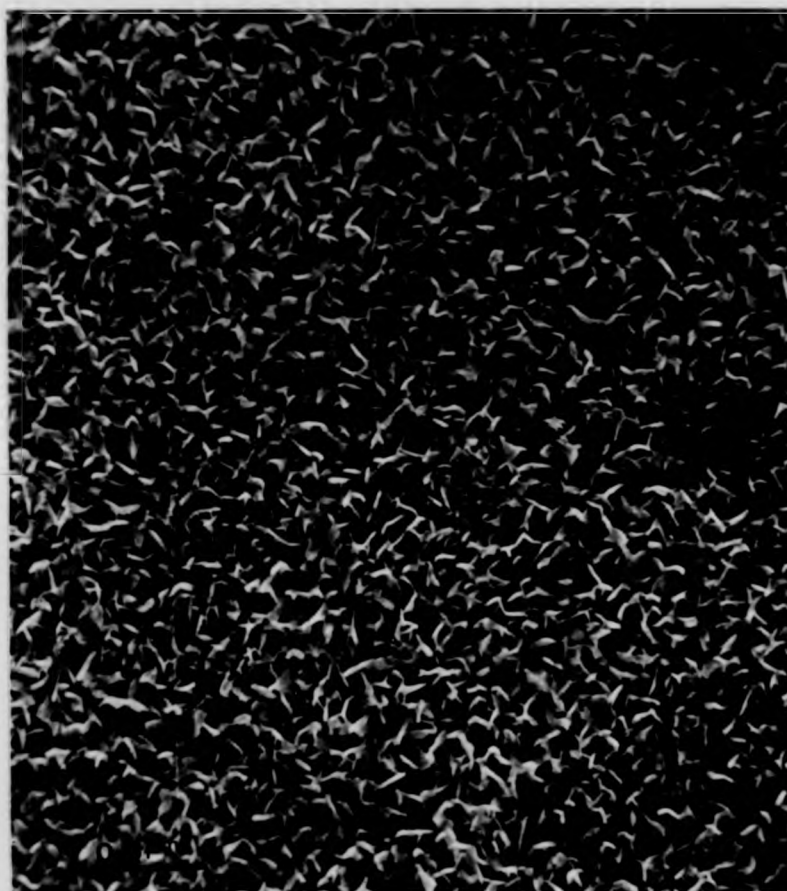


Figure 5.3.3b.

SEM image of the same sodium borate-formed oxide (Fig. 5.3.3a), after hydration at 85°C for 30 minutes. The "cornflake" structure has been revealed by a thin coating (3 nm) of platinum.

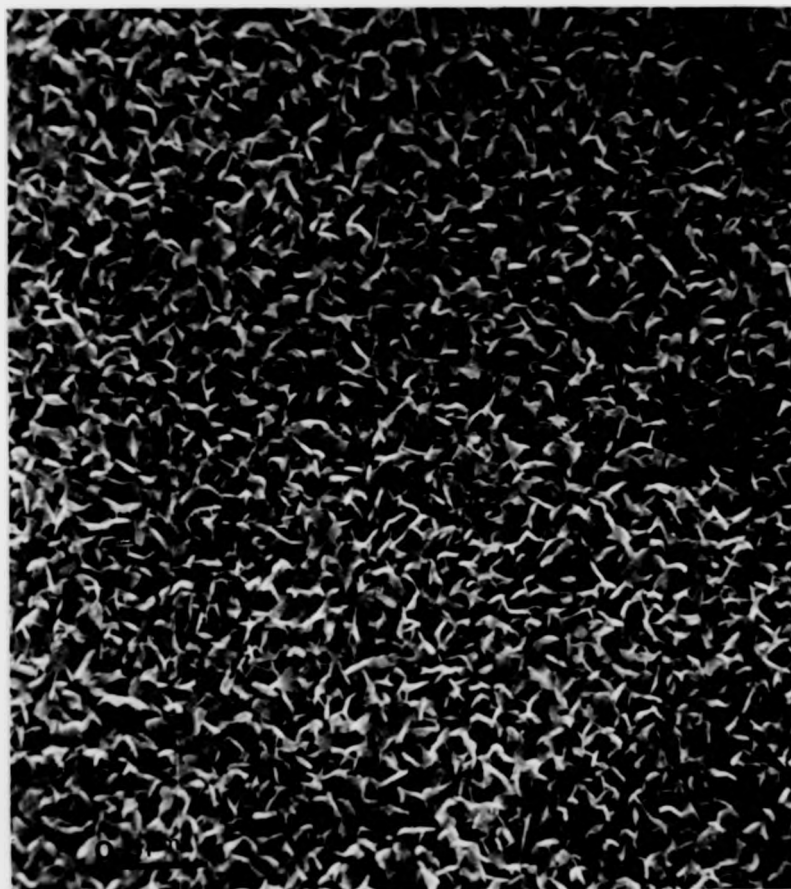


Figure 5.3.3b.

SEM image of the same sodium borate-formed oxide (Fig. 5.3.3a), after hydration at 85°C for 30 minutes. The "cornflake" structure has been revealed by a thin coating (3 nm) of platinum.

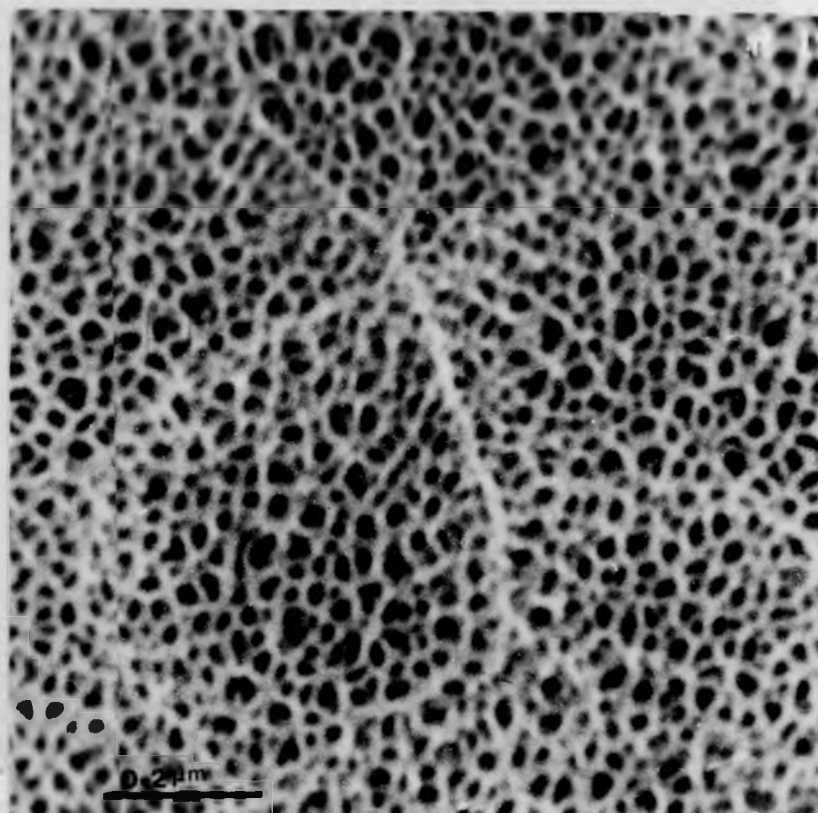


Figure 5.3.4a.

SEM image of 100 nm layer anodically formed on pure aluminium in phosphoric acid. The cellular, porous structure has been revealed by a thin (3 nm) coating of platinum.

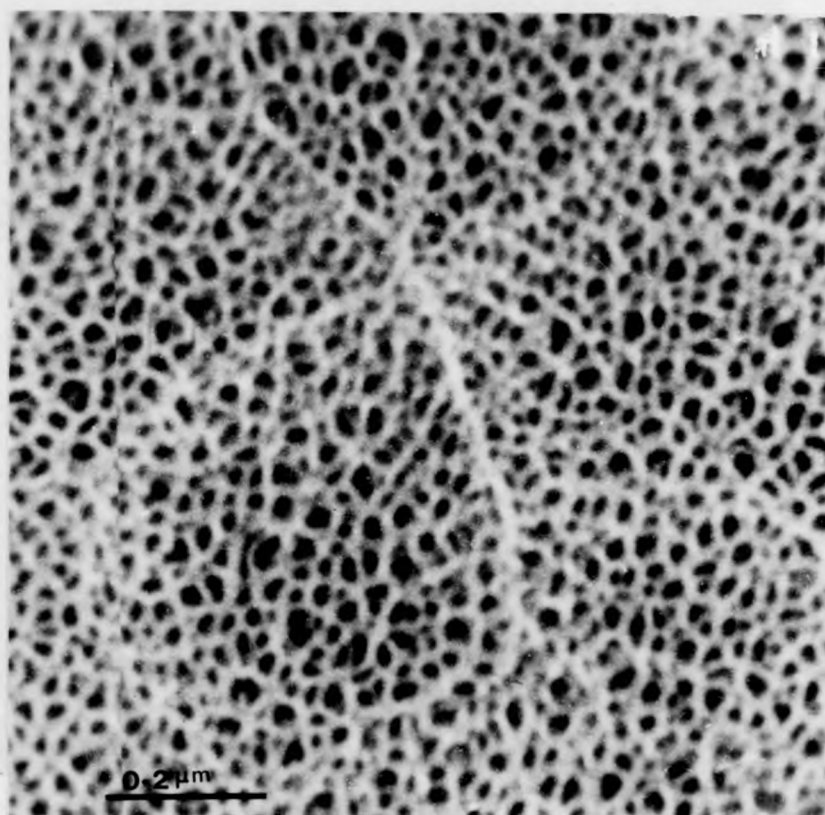


Figure 5.3.4a.

SEM image of 100 nm layer anodically formed on pure aluminium in phosphoric acid. The cellular, porous structure has been revealed by a thin (3 nm) coating of platinum.



Figure 5.3.4b.

SEM image of the same phosphoric acid-formed oxide (Fig. 5.3.4a) after hydration at 85°C for 4 hours. The "cornflake" structure has been revealed by a thin coating (3 nm) of platinum.



Figure 5.3.4b.

SEM image of the same phosphoric acid-formed oxide (Fig. 5.3.4a) after hydration at 85°C for 4 hours. The "cornflake" structure has been revealed by a thin coating (3 nm) of platinum.

anodizing conditions or possibly because their work was done on an aluminium alloy rather than pure metal. It is interesting that there is no evidence for a silicon impurity in this type of films even though the anodising treatment was carried out in a pyrex beaker. As will be discussed in Chapter 6 this is to be expected because the leaching of the pyrex and the consequent formation of a siliceous colloid does not occur in strongly acid electrolyte.

The hydration of this oxide yields the characteristic cornflake morphology which is completely different from the original oxide, as shown in figure 5.3.4b.

5.3.5. Micromorphological observations of the oxide and hydrated oxide formed in chromic acid solution

The oxide layer anodically produced on the surface of a pure aluminium substrate in chromic acid electrolyte appears to have a well developed morphology, as shown in figure 5.3.5a, which is significantly different from that formed in phosphoric acid. The morphology consists of hillocks, about $0.1 \mu\text{m}$ in diameter which have been clearly revealed in the morphology by tilting the specimen 40° away from normal incidence. It is interesting to note that large particles of an impurity phase, approximately 1-10 nm in diameter are attached to many of the hillocks. The EDAX spectra shown in figure 5.3.5a reveal clearly that these particles contain a high concentration of silicon. As in the case of sodium tartrate this oxide was formed by anodizing in a pyrex beaker. The siliceous impurity is therefore thought to be incorporated in the film during the anodizing treatment.



Figure 5.3.5a SEM image of oxide layer anodically formed on pure aluminium in chromic acid. The porous structure has been revealed by a thin (3 nm) coating. The hillocks of oxide have been revealed by tilting the specimen 40° away from normal incidence. Note the occurrence of siliceous impurity particles on many of the hillocks.



Figure 5.3.5a SEM image of oxide layer anodically formed on pure aluminium in chromic acid. The porous structure has been revealed by a thin (3 nm) coating. The hillocks of oxide have been revealed by tilting the specimen 40° away from normal incidence. Note the occurrence of siliceous impurity particles on many of the hillocks.

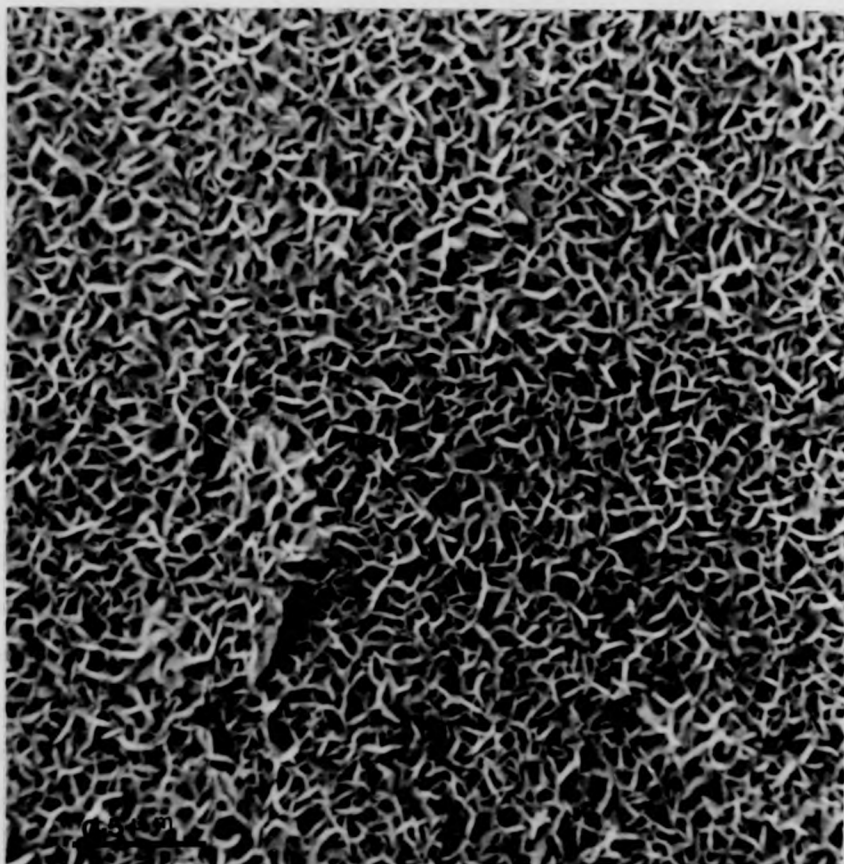


Figure 5.3.5b.

SEM image of the same chromic acid formed oxide (Fig. 5.3.5a) after hydration at 85°C for 4 hours. The "cornflake" structure has been revealed by a thin coating (3 nm) of platinum.

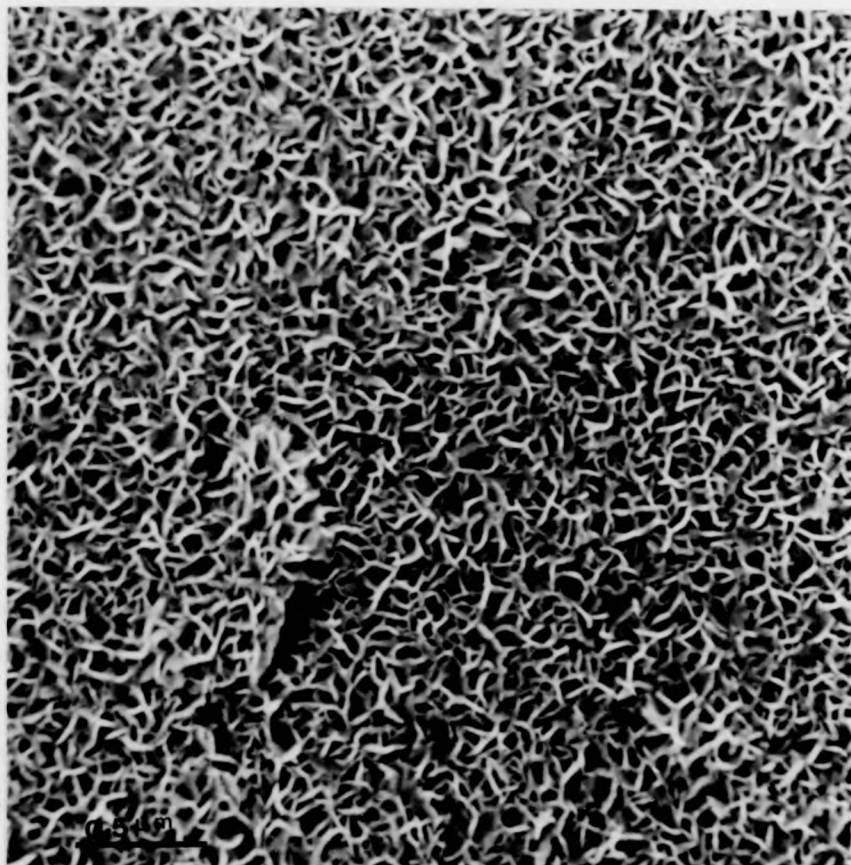


Figure 5.3.5b.

SEM image of the same chromic acid formed oxide (Fig. 5.3.5a) after hydration at 85°C for 4 hours. The "cornflake" structure has been revealed by a thin coating (3 nm) of platinum.

The hydration of this oxide in hot water at 85°C again causes it to transform to the cornflake morphology as shown in the SEM image (figure 5.3.5b). It is clear from this image that the silicon particles originally incorporated in the surface have been removed from the oxide during the hydration process. The cornflake morphology derived from this oxide is more sharply defined.

6.6. Summary

These results provide important new information about the structure of the oxide and the transformation due to hydration of both the non-porous and porous aluminium oxide films. The SEM observations reported here and elsewhere (Venables et al, 1979; Davis et al, 1982; El-Mashri, 1984) show that major morphological changes occur as a result of the hydration.

Both uniform films and porous films are converted to a new phase which is related to the boehmite structure. There are two possible ways in which the hydroxide phase might be formed: (i) by solid state transformation or (ii) by dissolution of the original oxide and re-precipitation in the form of oxyhydroxide. Both these mechanisms will be discussed in detail in the next chapter in the light of these observations and the EXAFS results.

References

1. Davies, G.D., Sun, T.S., Ahearn, J.S., Venables, J.D., (1982), J. Material Science, 17, 1807.
2. El-Mashri, S.M., Forty, A.J., Jones, R.G., (1983), Scanning Electron Microscopy, II: 569.
3. El-Mashri, S.M., (1984), Scanning electron microscopy, 1985/II in press.
4. Venables, J.D., McNamara, D.K., Chen, J.M., Sun, T.S., Hopping, R.L., (1979), Appl. Surface Sci., 3, 88.
5. Venables, J.D., McNamara, D.K., Chen, J.M., Ditchek, B.M., Morgenthaler, J.I., Sun, T.S., Hopping, R.L., (1980), Proceedings of the 12th National SAMPE Symposium, Seattle, Washington, 1980 (SAMPE, Azusa, California), 909.

CHAPTER 6

DISCUSSION OF STRUCTURE AND STRUCTURAL CHEMISTRY OF HYDRATION OF THE OXIDE FILMS

6.1. Introduction

This chapter is intended as a general discussion concerning the various results obtained using the technique of total electron yield EXAFS and scanning electron microscopy for the different aluminium oxides and hydrated oxides. It will also provide a discussion of the molecular structure of these amorphous films, and the structural chemistry of the hydration of the amorphous oxide.

Finally, the incorporation of various impurities (silicon and phosphorus) within the oxide films during the anodizing treatment and its influence on the hydration process will be dealt with.

6.2. The molecular structure of amorphous aluminium oxide

6.2.1. General background

The oxide layers formed by anodic polarization of aluminium in aqueous electrolytes are known to have a complex microstructure. The oxides produced by an anodization treatment in strong acids, such as phosphoric, chromic and sulphuric acid, have a porous morphology with both crystalline and amorphous phases present, as shown in this study and elsewhere, (see for example, Thompson and Wood, (1981); El-Mashri (1984)). The more uniform films formed in sodium tartrate and sodium borate solution are mainly amorphous when thin, but there is an increasing degree of crystallinity as the thickness increases.

Structural studies using electron diffraction and X-ray

diffraction techniques are of only limited value for amorphous solids. Notwithstanding this, Wilsdorf (1951) found that he could relate the diffuse haloes observed in transmission electron diffraction patterns with a possible structure composed of an Al_4O_6 molecular unit in the form of an octahedron of O^{2-} ions with Al^{3+} ions bonded to three O^{2-} ions on four of the faces. Later, Kerr (1956) showed that the broad haloes in electron diffraction patterns of anodic films formed on aluminium could not be immediately related to any of the known crystalline phases of alumina, and he supported Wilsdorf's explanation.

Oka et al (1979) have attempted to account for the various peaks in X-ray scattering patterns in terms of a disordered structure derived from γ -alumina. There is support for such a structure from X-ray fluorescence spectra (Takahashi et al, 1970) which have been interpreted on the basis that the Al^{3+} ions occur in both tetrahedral (4-fold) and octahedral (6-fold) coordination with O^{2-} ions, as in the case of crystalline γ -alumina, although the relative amount of Al^{3+} in these two states of coordination differs.

A more direct way of studying the structure has been used by El-Mashri et al (1981). This uses high voltage, high resolution electron microscopy to study directly the structure in very thin films (< 10 nm thick) prepared in sodium tartrate solution, and stripped from the aluminium metal in dilute HgCl_2 solution. This showed that, whilst the oxide is almost completely of a truly amorphous nature, there are small domains of quasi-crystalline structure. This HVREM study is discussed in detail in Appendix II.

A more direct understanding of the structure of amorphous alumina can be expected from the EXAFS measurements described in

earlier chapters. In this chapter it will be shown how the measurements of Al-O bond lengths can be used to deduce information at the molecular level about the state of coordination of the Al^{3+} ions. In principle it should also be possible to deduce this information from the EXAFS itself by considering the amplitude of the nearest neighbour contribution to the EXAFS. However, this is only possible if a reliable model for the structure is available and this is not yet the position as regards amorphous alumina.

6.2.2. The relationship between bond length and state of coordination

The most important results to be achieved from the EXAFS measurements are those relating to the nearest neighbour Al-O bond length. The Fourier transform of the EXAFS function gives interionic separations. Where there is a distribution of ionic separations, as might be expected for an amorphous material, this gives an average of such bond lengths. These average bond lengths can be used to give information about the average state of coordination. In this study where it is intended to develop the relationship between the measured bond lengths and the coordination number for a series of crystalline and amorphous aluminium oxides, an approach similar to that first adopted by Norman et al (1981), and later by El-Mashri, Jones and Forty (1983a) is used. For solids with predominantly ionic bonding the crystal potential, according to Pauling (1960), can be expressed as:

$$\epsilon = -Ae^2R^{-1} + B e^2R^{-n} \quad (6.1)$$

where A is the Madelung constant, e is the electronic charge, B is a repulsive coefficient, R is the nearest neighbour interionic distance and n is the Born exponent.

If we consider the crystal at absolute zero, the equilibrium condition requires ϵ to be a minimum. Differentiation of equation 6.1, to find the condition for a minimum, $d\epsilon/dR = 0$, results in

$$-Ae^2(-1)R_o^{-2} + Be^2(-n)R_o^{-n-1} = 0$$

which leads to

$$R_o = \left(\frac{Bn}{A} \right)^{\frac{1}{n-1}} \quad (6.2)$$

For similar structures the Madelung constant (A) changes very little, Pauling (1960), whilst the repulsive coefficient (B) is proportional to coordination number, N ; hence equation 6.2, may be written as:

$$R_o = \left(\frac{b Nn}{A} \right)^{\frac{1}{n-1}} \quad (6.3)$$

For the two structures x and y , the ratio of interionic distances is therefore given by

$$\frac{R_o^x}{R_o^y} = \left(\frac{N^x}{N^y} \right)^{\frac{1}{n-1}} \quad (6.4)$$

Since α -alumina was used as a model compound to calculate the phase in the EXAFS function of the various oxides, because its structure is well known and has approximately the same chemical composition as the amorphous solids, it can again be used here to obtain the coordination number for Al^{3+} in the amorphous oxide using equation 6.4, taking the interionic bond length for α -alumina to be $R = 0.1915$ nm, and $N^y = 6$ for reference (All Al^{3+} ions are octahedrally coordinated in α -alumina).

In this study the Born exponent (n) has been chosen to take two values; $n=9$, according to the analysis used by Norman et al (1981), and $n=8$ which could be considered to be more appropriate for the electron configuration in Al_2O_3 (Dekker, 1971).

It is now possible to obtain a simple relation between the measured bond length and the corresponding coordination number. Since the EXAFS for an amorphous oxide gives an average bond length, the coordination number which is deduced in this way is an average representation of the structure. If it is assumed that the amorphous structure is simply a bimodal distribution of octahedral $[\text{AlO}_6]$ and tetrahedral $[\text{AlO}_4]$ bonding, as reported by Oka et al (1979), and Norman et al (1981), it is possible to derive the fractions, a and b , of these two coordination states from the average coordination number:

$$N^x = 6a + 4b \quad (6.5)$$

Using equations 6.4 and 6.5, a simple relation between the measured bond length of a particular oxide and the percentages of the octahedral and tetrahedral bonding can be derived, as well as the average nearest neighbour coordination. A graphical means of doing this directly from the measured bond length, based on equations 6.4 and 6.5 is shown in figure 6.2.1. (a and b). As can be seen in this figure, the two values of the exponent used ($n=9$ and $n=8$) give quite close results for the coordination state; the values diverge more strongly at shorter bond length.

Because of the uncertainty concerning the appropriate value for the Born exponent ($n=8$ or 9), the coordination state deduced from figures 6.2.1 (a and b) is taken as the average value of the two curves. In addition to this systematic error there is an uncertainty in the coordination state arising from the error in determining the bond length from the EXAFS.

Figure 6.2.1

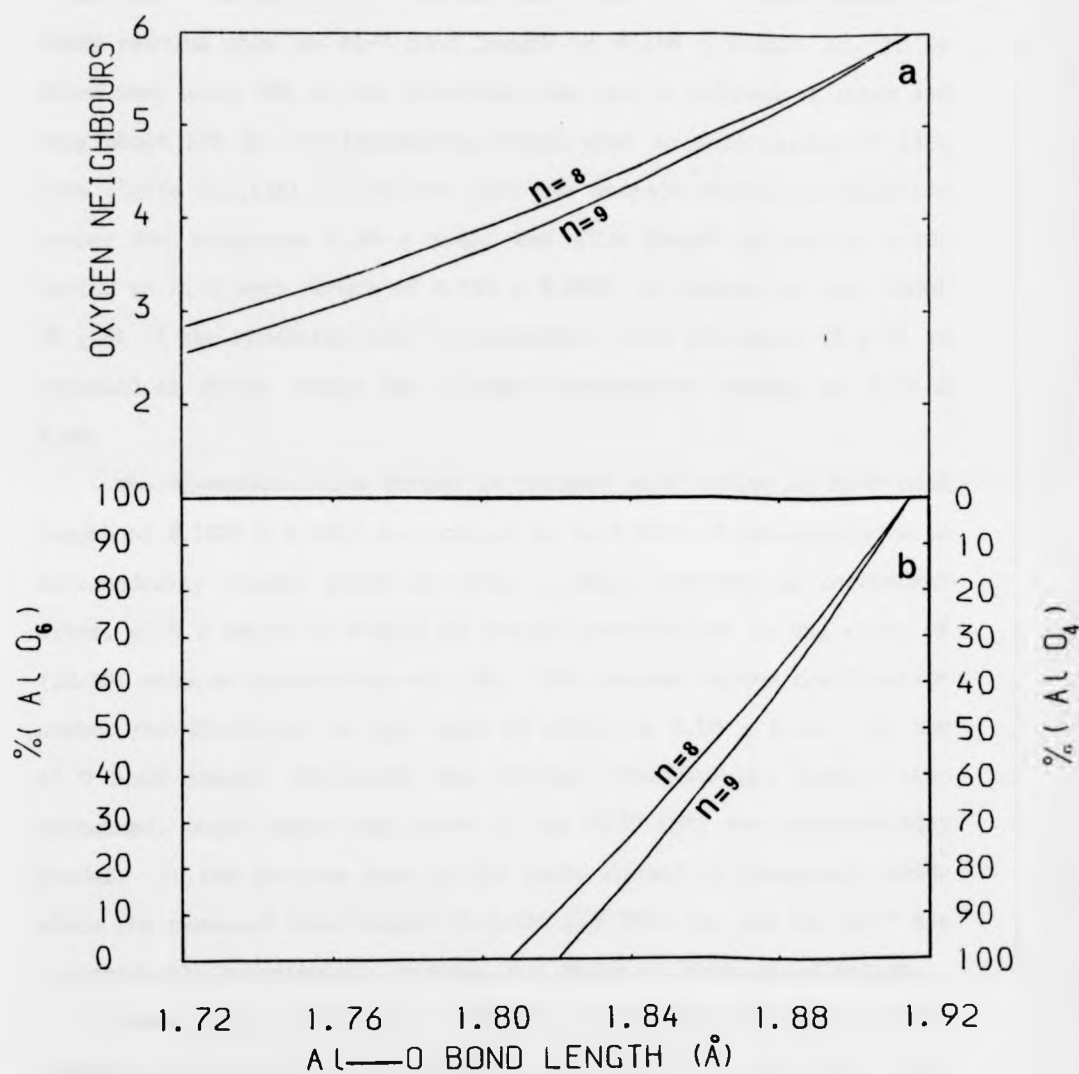


Figure 6.2.1a. The average number of oxygen neighbours of Al versus the average Al-O bondlength for aluminium oxide, assuming ionic bonding.

Figure 6.2.1b. The expected relationship between the distributions of octahedral (AlO_6) and tetrahedral (AlO_4) bond configuration and average bondlength for aluminium oxide, again assuming ionic bonding.

Using this approach for the uniform oxide layers formed on aluminium in sodium tartrate and sodium borate electrolytes, where the EXAFS results give an Al-O bond length of 0.190 ± 0.0025 nm, it is found that about 90% of the aluminium ions are in octahedral sites and only about 10% are in tetrahedral sites with an uncertainty of $\pm 8\%$. From figure 6.2.1(a) it follows that the average oxygen coordination number for aluminium 5.66 ± 0.40 . The film formed in oxalic acid, having an Al-O bond length of 0.185 ± 0.0025 nm appears to have about $30 \pm 8\%$ of the aluminium ions in octahedral sites and about $70 \pm 8\%$ in tetrahedral sites, while the average coordination number is 4.63 ± 0.40 .

The aluminium oxide formed in chromic acid having an Al-O bond length of 0.1825 ± 0.0025 nm, appears to have most of the aluminium in tetrahedrally bonded sites and only a small fraction in octahedral sites, with a ratio of 6-fold to 4-fold coordination in the range of (10/90) with an uncertainty of $\pm 8\%$. The average oxygen coordination number for aluminium in this type of oxide is 4.10 ± 0.40 . As the Al-O bond length decreases the average coordination number also decreases, which means that more of the Al^{3+} ions are tetrahedrally bonded. In the extreme case of the oxide formed in phosphoric acid, where the measured bond length is 0.180 ± 0.0025 nm, all the Al^{3+} are tetrahedrally coordinated, or even in a state of lower coordination.

There is clearly a wide variation in coordination in amorphous alumina, reflecting the variation of molecular structure when different methods of preparation are used. The average coordination number, and the ratio of $\text{AlO}_6/\text{AlO}_4$ for the various oxides are summarized in Table 6.2.

TABLE 6.2

Electrolyte	Al-O (nm)	Calculated Oxygen neighbours to Al	[AlO ₆]/[AlO ₄]
Sodium Tartrate	0.190 ± 0.0025	5.66 ± 0.40	[90/10] ± 8
Sodium Borate	0.190 ± 0.0025	5.66 ± 0.40	[90/10] ± 8
Sodium Oxalate	0.185 ± 0.0025	4.63 ± 0.40	[30/70] ± 8
Chromic Acid	0.1825 ± 0.0025	4.10 ± 0.40	[10/90] ± 8
Phosphoric Acid	0.180 ± 0.0025	4.00 ± 0.40	[0/100] ± 8

6.2.3. Comparison with other determinations of coordination state

In this section a comparison is made between the results obtained in this work and the results derived from other structural studies using electron diffraction, X-ray diffraction and X-ray fluorescence spectroscopy techniques.

Saitoh, Ikegaya and Takahashi (1977), using a radial distribution function, derived from X-ray diffraction for the oxides formed in oxalic acid and sulphuric acid, reported that the coordination number of oxygen with aluminium ions is 5.9 for anodic oxide formed in oxalic acid, which corresponds to a $\text{AlO}_6/\text{AlO}_4$ ratio of 95:5, while the coordination number in the case of oxide formed in sulphuric acid is 40:60. Takahashi et al (1971), measured the Al-O bond length in the oxide film prepared anodically in oxalic acid by means of a radial distribution analysis of X-ray diffraction patterns, and found the bond length to be 0.193 nm. It can be concluded from figure 6.2.1. and the Al-O separation of α -alumina, that this bond length corresponds to a 100% octahedral coordination. The only explanation for this is that the oxide film may have become partially hydrated to form boehmite with a consequent increase in the average Al-O bondlength.

Jones (1974) quotes a $\text{AlO}_6/\text{AlO}_4$ ratio of 8:92 from the transmission electron diffraction pattern, using a radial distribution function, for a stripped oxide film formed in sodium borate at pH 7.0 on pure aluminium. Oka et al (1979) reported a $\text{AlO}_6/\text{AlO}_4$ ratio of 40:60 and 30:70, derived from X-ray fluorescence spectroscopy, for films formed in sulphuric acid using a.c. and d.c. polarizing voltages respectively. Hanada et al (1982), using X-ray fluorescence spectroscopy, find an average coordination number of about 4.8 from an amorphous alumina film formed by r.f. sputter deposition. This value corresponds to a $\text{AlO}_6/\text{AlO}_4$ ratio of 40:60. Popova (1979), using transmission electron diffraction found a bond length of 0.182nm

for an aluminium oxide film formed on aluminium by anodic oxidation in borate solution, which corresponds to completely tetrahedral coordination. Takahashi et al (1971), using radial distribution analysis from X-ray diffraction patterns, found bond lengths of 0.188 nm and 0.193 nm for oxide films formed in pure and impure sulphuric acid respectively. These bond length values correspond to $\text{AlO}_6/\text{AlO}_4$ ratios of 95%:5% and 100%:0% respectively according to figure 6.2.2. Norman et al (1981) reported a bond length of 0.185 nm from surface-EXAFS measurements for an anodized aluminium sample of unknown origin. This corresponds to a ratio of octahedral to tetrahedral sites of about 30:70.

The summary of the results in this study shows that a generalized model for the structure of amorphous alumina might consist of a mixture of $[\text{AlO}_6]$ and $[\text{AlO}_4]$ coordination with different proportions depending on the preparation method and on the electrolyte used; this ratio also depends on the purity of the aluminium substrate and purity of electrolyte, as well as the incorporation of electrolyte anions which can affect the structure. For example, the incorporation of an element of higher valency such as phosphorus or chromium should change the bonding in the oxide and therefore lead to a reduction of $[\text{AlO}_4]$ centres.

The significance of such a conclusion concerning the molecular composition of the amorphous aluminas clearly depends on the accuracy with which the average Al-O bond length is determined. However the quality of the EXAFS spectra obtained in our experiments is good, as shown in Figure 3.5.2 giving an expectation of a high degree of accuracy in measurement of bond lengths (± 0.0025 nm). These results

have also been compared with the results obtained using the technique of TEM EXELFS (extended electron energy loss fine structure) for the oxygen K-edge at 535 eV. EXELFS spectra for the thin amorphous anodic alumina films formed in sodium tartrate have been obtained by Bourdillon, El-Mashri and Forty (1984). The O-Al separation obtained by such measurements is 0.189 nm compared with 0.190 nm obtained by Al K-edge EXAFS. There is, therefore, excellent agreement between the results obtained for the same material by these two techniques, which gives a good confirmation of the reliability of EXAFS as a means of measuring bond lengths. The TEM EXELFS study is presented in Appendix I.

6.2.4 A possible model for the local structure of amorphous alumina

Using all the information that has been obtained from the electron-yield EXAFS on the structure of amorphous alumina reported in this work and elsewhere (Norman et al (1981); El-Mashri, Jones and Forty (1983); Forty and El-Mashri (1985) to be published), a model for the local structure of amorphous aluminium oxide is constructed to be consistent with this information. The model is based on Wilsdorf's conclusion (1951) from electron diffraction that the structural unit in amorphous Al_2O_3 is the Al_4O_6 octahedron shown in figure 6.2.2a. A crystalline analogue for the amorphous structure can be composed from the individual octahedral units, arranged to give the mixture of tetrahedral (AlO_4) and octahedral (AlO_6) bonding and average coordination number found from the EXAFS results. This can be disordered to give the amorphous state by incorporating atomic defects and bond distortions in the regular structure.

Figure 6.2.2 illustrates the method of constructing the crystalline analogue. Figure 6.2.2a shows the Al_4O_6 dimer

suggested by Wilsdorf (1951). The large circles represent O^{2-} ions and the smaller circles are Al^{3+} ions (the relative sizes of the O^{2-} ions and Al^{3+} ions are such that the O^{2-} ions are in close contact but they are separated in the diagram for clarity of presentation; a three-dimensional representation in several different perspectives using a more realistic ratio of O^{2-} and Al^{3+} ionic radii is given in figure 6.2.3. Figure 6.2.2b, shows a sheet of Al_4O_6 octahedra with three-fold sharing of Al-O edges of individual octahedra. The three-dimensional structure is then composed by stacking the two-dimensional sheets on top of each other as shown in figure 6.2.2c. The resulting structure is a distorted hexagonal close-packing sequence of layers of O^{2-} ions interpenetrated by another hexagonal sequence of Al^{3+} ion layers. In the usual notation for close-packed structure, the arrangement can be represented by a sequence



where the Roman letters represent close-packed O^{2-} ion layers and Greek letters are the smaller Al^{3+} ions which occupy interstitial positions between O^{2-} layers. It can readily be seen from figure 6.2.2c that Al^{3+} ions in the β -positions are in tetrahedral (4-fold coordination) sites, between a and b O^{2-} layers, whilst those in γ -positions occupy octahedral (6-fold coordination) sites.

An inspection of figures 6.2.2b and c shows that the sheets of the octahedra do not have the correct chemical composition for Al_2O_3 . Furthermore, figure 6.2.4b shows a projection of a 2-dimensional sheet of Al_4O_6 dimers defining a unit cell of the

Fig.6.2.2.

The proposed model for amorphous alumina:-

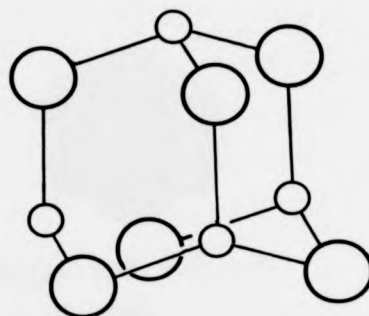
(a) the Al_4O_6 dimer suggested by Wilsdorf (1951). The large circles represent O^{2-} ions and smaller circles are Al^{3+} ions (the relative sizes of the O^{2-} ions and Al^{3+} ions are such that the O^{2-} ions are in close contact but they are separated in the diagram for clarity of presentation);

(b) part of a three-dimensional sheet of edge-sharing Al_4O_6 octahedra;

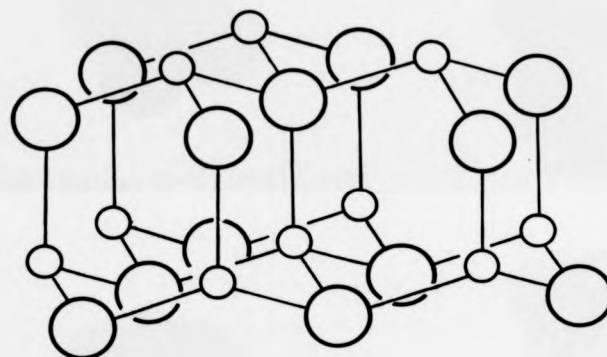
(c) the three-dimensional structure composed of stacked sheets of octahedra. The Roman letters indicate the close packing of layers of O^{2-} ions and the Greek letters indicate Al^{3+} in tetrahedral (β) and octahedral (γ) interstitial sites. Note the occurrence of four O^{2-} ions bonded to each β -type Al^{3+} ion and six O^{2-} ions around each γ -type Al^{3+} ion.



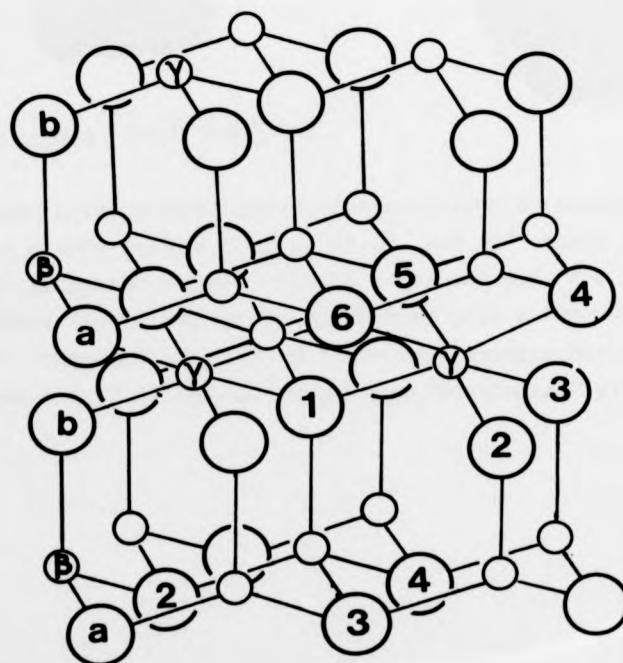
Fig.6.2.2.



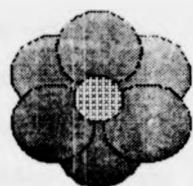
a



b



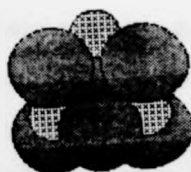
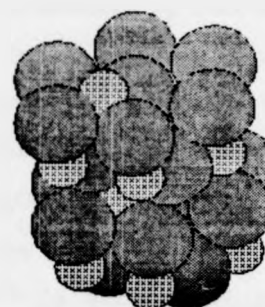
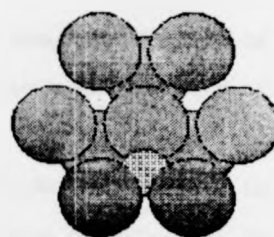
c



Rotation angles: $X=0^\circ$, $Y=0^\circ$, $Z=0^\circ$



Rotation angles: $X=45^\circ$, $Y=45^\circ$, $Z=45^\circ$



Rotation angles: $X=90^\circ$, $Y=90^\circ$, $Z=0^\circ$

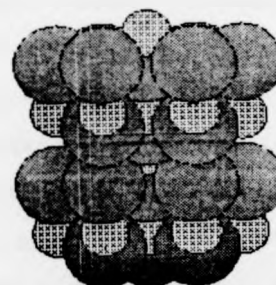


Figure 6.2.3. Shows a three dimensional representation in several different perspectives using a more realistic ratio of O^{2-} and Al^{3+} ionic radii for the proposed model for amorphous alumina. On the left-hand side the Al_4O_6 dimer suggested by Wilsdorf (1951) and on the right-hand side a "two unit cells on top of each other", composed of parts of three edge-sharing octahedra; note the omission of two-thirds of the Al^{3+} ions from "octahedral" sites to achieve stoichiometry.

crystalline analogue denoted by the dotted lines, composed of parts of three edge-sharing octahedra. This unit cell shows equal numbers of Al^{3+} in four-fold and six-fold coordination. The stoichiometric balance can be restored simply by omitting two-thirds of those Al^{3+} in the octahedral sites. However this leads to a ratio of $\text{AlO}_4/\text{AlO}_6$ in the new structure equal to 3:1. Other ratios are obtained by removing Al^{3+} ions from tetrahedral sites as well as from octahedral sites. For example, by omitting 5/9 of those Al^{3+} in octahedral sites and 1/9 of those in tetrahedral sites, as shown in figure 6.2.4c, a ratio of 2:1 is obtained. The measured ratio of $\text{AlO}_4/\text{AlO}_6 = 7:3$ which is suggested by some of the EXAFS measurements (see table 6.2) requires the omission of 9/15 and 1/15 of the Al^{3+} in octahedral and tetrahedral sites, respectively, as shown in figure 6.2.4d. It should be noted that in all cases these defective structures (figure 6.2.4a,b,c,d) have the stoichiometric composition of Al_2O_3 .

This model can be adapted to give the appropriate stoichiometric composition and the measured ratio of $\text{AlO}_4/\text{AlO}_6$ for any of the amorphous aluminas investigated by omitting the right amount of Al^{3+} from the octahedral and tetrahedral sites. Support for the proposed sheet model has been found by studying the structure of amorphous alumina by high resolution transmission electron microscopy (El-Mashri et al, 1981). As already described, very thin amorphous films prepared on pure aluminium by anodizing in neutral sodium tartrate solution were found to contain, small domains, of order 100 \AA in diameter, where the normally amorphous structure is partially ordered into layers a few \AA apart. The measured spacing of these "lattice

Fig. 6.2.4. Basal phase projections of the proposed sheet structure. Large circles represent O^{2-} ions and small circles are Al^{3+} ions. The solid lines represent Al-O bonds. Al^{3+} ion vacancies are introduced to achieve the stoichiometric composition of Al_2O_3 :-

(a) the Wilsdorf octahedron Al_4O_6 ;

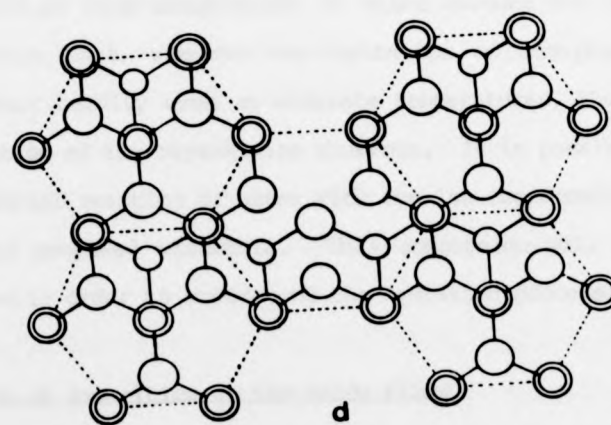
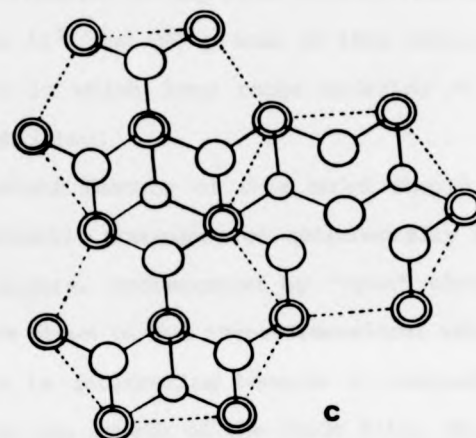
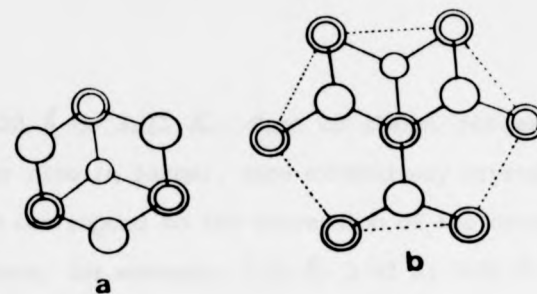
(b) a "unit cell", denoted by the dotted lines, composed of parts of three edge-sharing octahedra; note the omission of two-thirds of the Al^{3+} ions from "octahedra" sites to achieve stoichiometry;

(c) a sheet of three "unit cells" with the omission of 5/9 of the Al^{3+} from "octahedral" sites and 1/9 of Al^{3+} from "tetrahedral" sites to achieve stoichiometry.

(d) a sheet of five "unit cells" with the omission of 9/15 of the Al^{3+} ions from "octahedral" sites and 1/15 from "tetrahedral" sites; this structure is stoichiometric and the tetrahedral sites are occupied in the ratio 7:3.



Fig. 6.2.4.



fringes" ranges from 1.20 Å to 3.71 Å. Some of these, for example 1.38 Å and 1.98 Å, appear also in larger, more extensively crystalline regions of the films and correspond to the conversion of the amorphous oxide to γ -alumina. Others, for example, 3.71 Å, 3.03 Å, 2.62 Å, 2.07 Å and 1.90 Å, do not correspond to any known crystalline oxide but do occur as spacing of the Al^{3+} and O^{2-} planes in this model. They are interpreted as domains in which long range ordering of the sheet structure has been established.

Finally, an important feature of this model should be pointed out; that is, the systematic occurrence of tetrahedrally bonded Al^{3+} ions in basal plane layers, accompanied by "open" channels along particular directions as shown in the three-dimensional representation (Figures 6.2.2). This is interesting because it suggests that ion transport, essential for the growth of the oxide film, can proceed at a significant rate even at room temperature. It might account for the interesting observation that, whereas the hydration of amorphous alumina appears to occur readily even at moderate temperatures, there is little or no hydration of the crystalline aluminas. It is possible to envisage a preferential reaction of water with the low coordination (AlO_4) groups in this proposed structure. This conclusion will be used in later sections in order to understand the hydration process.

6.3. The incorporation of impurities in the oxide films

In practice, it is known that the oxide films, formed by anodic oxidation, appear to have some contamination caused by electrolyte anions being preferentially incorporated on the oxide/electrolyte interface. In this study, two types of impurity contamination were observed in the oxide, namely silicon and phosphorus and these are discussed below.

6.3.1. The incorporation of silicon impurity in the oxide during the anodic oxidation process

During this study, an interesting phenomenon has been observed, namely the occurrence of large irregularly shaped particles which are strongly absorbing in the TEM image of the amorphous alumina films. It is interesting to note that in some of the EXAFS spectra there appeared a second characteristic absorption edge (see for example, figure 3.5.2), which corresponds to the silicon K-edge. The silicon concentration in the alumina film can be estimated using the relative heights of the Al and Si K-edges, since the K-edge photoelectron cross-sections of aluminium and silicon are similar (Storm and Israel, 1970). The relative heights indicate an Al:Si ratio of about 10:1. The increase of the silicon K-edge absorption with film thickness evident in figure 3.6.1 indicates that the silicon impurity is contained within the body of the oxide film and is not simply a deposit on its surface.

Using scanning electron microscopy and EDAX analysis, it has been shown that the irregularly shaped particles are rich in silicon, whilst the surrounding oxide is silicon-free. This is illustrated by figure 5.3.1b.

It is known from an earlier study by Vedder and Vermilyea (1969) that an aluminium surface can be contaminated by a siliceous deposit during the anodic oxidation process. This silicon arises as a result of a leaching action on a pyrex container by the electrolyte, particularly neutralised electrolytes such as sodium tartrate. Pyrex is a borosilicate glass which contains silica (SiO_2), boric acid (B_2O_3), soda (Na_2O) and alumina (Al_2O_3) with ratios of 80:14:4:2 respectively.

The EXAFS and SEM results provide a direct confirmation of the presence of the siliceous impurity and, furthermore, show that the impurity is accommodated as large particles (1-10 μm in diameter). These particles are likely to be produced by a reaction between silica (SiO_2) and water, following the chemical processes reviewed by Iler (1963):

Initially the silica dissolves to form monosilicic acid $\text{Si}(\text{OH})_4$



The monosilicic acid then polymerises to form products ranging from polysilicic acid gel to colloidal silica sols, giving irregularly shaped particles varying in size from 0.01 to 1.0 nm in diameter. In the pH range 7-10, the particles adsorb hydroxyl ions on their surface and become negatively charged:



The amount of charge depends on the salt concentration and controls the aggregation of the particles into sols, and, due to the charge, migration to the anode will occur, followed by deposition in the oxide surface.

In order to avoid this contamination by silicon a non-glass container should be used for the anodising treatment. This precaution was observed in preparing the anodic films after the initial experiments using sodium tartrate electrolyte. It was found that by using an aluminium container oxides could be obtained almost silicon-free.

6.3.2. The incorporation of phosphorus impurity in the oxide film

From the literature, it is known that oxide films produced anodically in phosphoric acid electrolyte appear to have a large

amount of phosphorus impurity. The amount of impurity depends on the anodization conditions (see for example Hunter et al (1959)). Plumb (1958), who examined thin films formed by anodic oxidation in a phosphate electrolyte, reported that the oxide layer contained P_2O_3 which was distributed uniformly through the film. Konno et al (1980) investigated the composition of similar thin anodic oxide films, again formed on aluminium in phosphate solution. Using X-ray photoelectron spectroscopy (XPS) they reported that the films contained phosphorus internally as deep as 75 nm.

In a more recent study, Davis et al (1982) used XPS to map the chemical elements in alumina films. XPS gives the chemical composition of the oxide film within the sampling depth of this technique, which in general is only a small number of atomic layers below the surface. The surface of the freshly formed oxide on an aluminium-copper alloy, using a phosphoric acid electrolyte, was shown to have a composition of $AlPO_4$. In the present study, the EXAFS spectrum (figure 6.3.1) of the oxide film prepared in 10%wt phosphoric acid appears to have a second peak at 2149 eV, corresponding to the phosphorus K-absorption edge. According to the relative heights of the absorption edges in the EXAFS spectrum, the P:Al ratio is about 1:10. Taking into account the thickness of the film and the large sampling depth of the electron yield EXAFS (≈ 50 nm), this ratio suggests that considerably more than a surface monolayer of $AlPO_4$ is present. This finding is supported by the fact that, when the film is hydrated, it appears from the EXAFS spectrum that almost the same amount of phosphorus is retained (this will be discussed in the next section). Our results show, therefore, that the phosphorus impurity is distributed more extensively throughout the oxide, in agreement

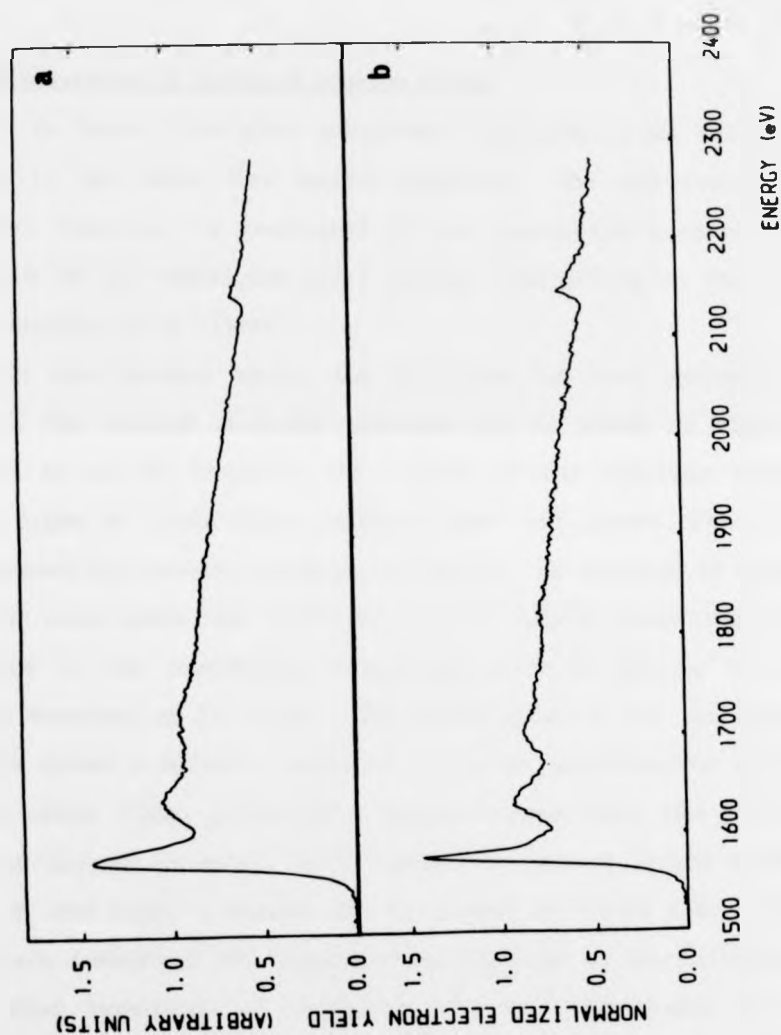


Figure 6.3.1. (a) The electron yield-EXAFS spectrum for the oxide film prepared in phosphoric acid appears to have a second peak at 2149 eV, corresponding to the phosphorus K-absorption edge;

(b) The electron yield-EXAFS spectrum for the same oxide film formed in phosphoric acid after hydration for 4 hours at 85°C.

with the observation reported by Konno et al (1980), and this supports the idea that the phosphorus impurity might modify the internal structure.

6.4. The structure of hydrated alumina films

It is known that when amorphous aluminium oxide films are immersed in hot water they become hydrated. The occurrence of a hydration reaction is indicated by gas evolution arising from hydrolysis of the underlying metal through disruptions in the oxide films, Venables et al (1980).

In this present study, the hydration has been performed by immersing the various anodised specimens in hot water at 85°C, as described in earlier Chapters. The results of this hydration process on both types of oxide films (uniform layer and porous films) have been observed by scanning electron microscopy. As reported in Chapter 5, it has been shown that hydration clearly occurs, resulting in an appearance of the "cornflake" morphology which is similar to that found by Venables et al (1980). The EXAFS spectrum and its Fourier transform showed a definite change of molecular structure for all the hydrated oxide films, producing a hydrated phase with two distinct values of nearest neighbour Al-O separation centred around 0.200 ± 0.0025 nm and 0.280 ± 0.0025 nm, as listed in table 4.4. These results are consistent with observations reported in the literature, namely that hydration of amorphous alumina films leads to the formation of an oxy-hydroxide, which is usually described as pseudo-boehmite, referring to the fact that it is amorphous or quasi-crystalline in structure (see for example, Papee et al, 1958). Crystalline boehmite has a structure of a double layer of

aluminium-centred octahedra which are usually linked by O-H-O bonding to other double layers, Sasvari and Zalai (1957). The distortion of the octahedra gives two distinct Al-O bond lengths of 0.190 nm and 0.250 nm. Allowing for the uncertainty in the determination of the bond lengths from the EXAFS data (0.200 ± 0.0025 nm and 0.280 ± 0.0025 nm) (see table 4.4) the present results seem to give a reasonably good identification of the hydrated oxides as being pseudo-boehmite.

6.5. The structural mechanism of the hydration reaction

The new boehmite-like phase formed by the hydration of amorphous alumina is mechanically weaker than the amorphous material. Hydration therefore leads to a degradation of epoxy-resin/metal bonding, for example. A better understanding of the structural mechanism by which the hydration of amorphous aluminium oxide takes place is therefore highly desirable.

There are two possible ways in which the hydration reaction might occur: either by a solid state transformation of the oxide phase or by dissolution of the oxide and re-precipitation of the oxy-hydroxide phase. The results from the present work on the tartrate-formed films which are contaminated with siliceous particles provide some evidence for the dissolution and re-precipitation reaction. The significant change in the X-ray absorption spectrum after immersion in water at 85°C for 30 minutes, (see, for example, fig. 6.3.1 where the spectrum of the hydrated film is compared with that for the original un-hydrated oxide) together with the SEM observation of the usual cornflake morphology, indicates that the film is transformed to boehmite by hydration. The absence of the siliceous particles in the SEM images of the hydrated film (figure 5.6.1c) and also the absence

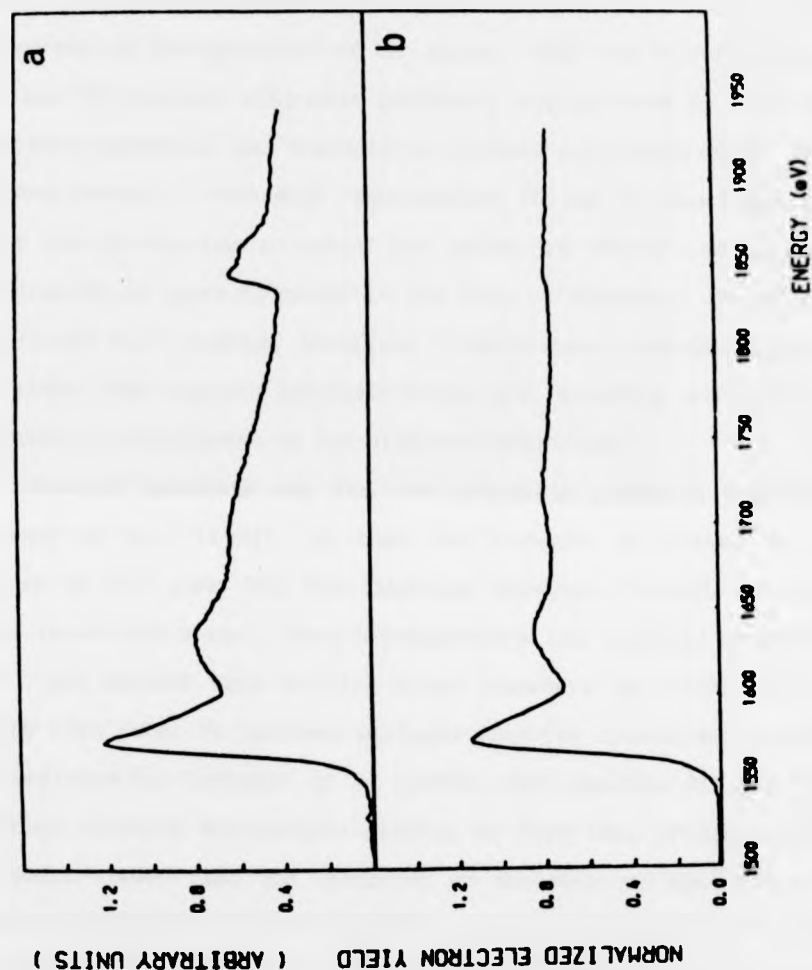


Figure 6.5.1

(a) The electron yield EXAFS spectrum for a 50 nm sodium tartrate-formed oxide on pure aluminium, appears to have a second peak at 1840 eV, corresponding to the silicon K-absorption edge;

(b) the electron yield EXAFS spectrum for the same film after hydration for 15 minutes at 85°C. Noting the disappearance of the silicon K-absorption edge.

of the silicon K absorption edge in the EXAFS spectrum (figure 6.5.1b) suggest that the particles are either dissolved or have become detached during the hydration of the oxide. This was found to be the case also for similar siliceous particles incorporated in the oxide formed when aluminium was anodised in chromic acid electrolyte using the pyrex beaker. From such observations it can be concluded that during the hydration process the oxide is dissolved and the oxy-hydroxide is reprecipitated in the form of boehmite, rather than being formed by a process involving a solid-state transformation of the oxide; the latter process would not readily explain the dissolution or detachment of the siliceous particles.

Another possible way for the hydration reaction to occur, suggested by Hart (1954), is that the boehmite is formed by the migration of Al^{3+} ions from the aluminium substrate through the oxide film to react with water. This interpretation was rejected by Spooner (1956), who showed that boiling water converts an oxide film to boehmite even after it has been stripped from the aluminium. This has been confirmed by El-Mashri et al (1981) (see appendix II), in high resolution electron microscopic studies of very thin stripped oxide films which showed that the character of the thin stripped film was changed by hydration in water at 85°C. At atomic resolution it was found that the small quasi-crystalline domains present in the non-hydrated films become greatly increased in size after exposure to water for only a few minutes.

The presence of a phosphorus peak in the EXAFS spectrum of the oxide formed in phosphoric acid even after the film was hydrated provides further evidence against Hart's suggestion. The hydrated films have the typical cornflake structure (Figure 5.5.4b) which has a

thickness in the region of $0.1 \mu\text{m}$. The excitation depth for electron emission is much smaller than this thickness ($\approx 50 \text{ nm}$). Consequently, if the oxy-hydroxide formation was due to migration of aluminium ions through the existing oxide film to form this typical thicker cornflake structure, as claimed by Hart, phosphorus would not be detected in the EXAFS measurements.

6.6 Suggestions for further work.

Although the conclusions concerning the molecular structure of the anodic aluminium oxides described in this thesis are useful they are strongly dependent on the relationship between measured bondlength and coordination number. The EXAFS measurements of bondlength are subject to significant errors, both random and systematic, and this uncertainty is reflected in the conclusions drawn from them about coordination of the Al^{3+} and O^{2-} ions. Clearly, attempts must be made to refine these measurements so as to increase the reliability of such conclusions about the structure of the oxide. The fractions of octahedral (AlO_6) and tetrahedral (AlO_4) coordination in a given oxide are strongly dependent on the average coordination number which, in turn, is dependent on the measured average bondlength. It is highly desirable to have a more direct probe for the state of coordination.

One possibility for such an improvement in work of this kind is to use the newly developed techniques of Magic-Angle Spinning (MAS) NMR. This gives very high resolution spectra for nuclei of certain atoms with characteristic peaks whose positions depend closely on the electric field due to surrounding atoms. An initial study of

amorphous alumina films formed in sulphuric acid electrolyte using this technique by Dupree and Forty (1985 - to be published) has revealed octahedral (AlO_6) and tetrahedral (AlO_4) centres and also a new type of centre (AlO_5). This 5 co-ordinated centre appears to be related to the incorporation of $(\text{SO}_4)^{2-}$ anions in the oxide.

It is suggested that an application of MAS NMR together with EXAFS studies would lead to a much greater understanding of the structure of alumina films, and particularly the influence of anion and other impurities on the structure.

These more refined structural studies should be accompanied by a detailed investigation of the effects of electrolyte, pH and temperature on the structure of anodic oxides. As a further development there should be an attempt to correlate a systematic study of the kinetics of film growth and the structure of the oxide. The great importance of hydration on the properties of the oxide justifies a more extensive study of the structural factors involved. A correlated investigation of the kinetics of hydration and the influence of impurities, and deliberate additions of inhibitors on the hydration process would be extremely valuable.

REFERENCES

1. Bourdillon, A.J., El-Mashri, S.M. and Forty, A.J. (1984), Phil.Mag., A49, 341.
2. Davis, G.D., Sun, T.S. Ahearn, J.S. and Venables, J.D. (1982), J.Material Science, 17, 1802.
3. Dekker, A.J., (1971), Solid State Physics (MacMillan Press), pl21.
4. El-Mashri, S.M., Forty, A.J., Freeman, L.A. and Smith, D.J., (1981), Electron Microscopy and Analysis, ed: M.J. Goringe, Inst. Phys.Conf., Ser.No.61. (Bristol, London: The Institute of Physics), 395.
5. El-Mashri, S.M. Forty, A.J. and Jones, R.G., (1983), Scann. Electron. Microsc.,II, 569.
6. El-Mashri, S.M., Jones, R.G. and Forty, A.J., (1983a), Phil.Mag.48A, 665.
7. El-Mashri, S.M., Jones, R.G. and Forty, A.J., (1983b), Appl.Surf.Science, 17, 124.
8. El-Mashri, S.M., (1984), Scann.Elect.Microsc., To appear in Vol.II (1985).
9. Forty, A.J. and El-Mashri, S.M., (1985), Phil.Mag. To be submitted.

10. Hanada, T., Alkawa, T. and Soga, N., (1982), J.Non-crystalline Solids, 50, 397.
11. Hart, R.K., (1954), Trans.Frad.Soc., 50, 269.
12. Hunter, M.S., Towner, P.E. and Robinson, D.C., (1959), Amer. Electro-Plat. Soc., Techn. Proc., 220.
13. Iler, R.K., (1973), Surface Colloid Sci., 6, 1.
14. Jones, A.M., (1974), Ph.D. Thesis, Texas Christian University.
15. Kerr, I.S., (1956), Acta Cryst., 9, 879.
16. Konno, M., Goshima, T., Kaneko, Y. and Kudo, T., (1980), Proceedings of Interfinish 80, 250.
17. Norman, D., Brennen, S., Jaeger, R. and Stohr, J., (1981), Surface Science, 105, L297.
18. Oka, Y., Takahashi, T., Okada, K. and Twai, S., (1979), J.Non-cryst. Solids, 30, 349.
19. Papee, D., Tertian, R. and Biaise, R., (1958), Bull.Soc.Chim.Fr., 1301.
20. Pauling, L., (1960), The Nature of the Chemical Bond (Ithaca: Cornell University Press).

21. Plumb, R.C., (1958), J.Electrochem.Soc., 105, 498.
22. Popova, I.A., (1979), Inorg.Mater. (Eng.Transl.), 14, 1503.
23. Saitoh, J., Ikegaya, M. and Takahashi, T., (May 8-13, 1977), The Electrochem.Soc.Inc., Spring Meeting, Philadelphia, Pennsylvania, 155.
24. Sasvari, K. and Zalai, A., (1957), Geologica Hung.,4, 415.
25. Storm, E. and Israel, H.I., (1970), Nuclear Data Tables, A7,567.
26. Spooner, R.C., (1958), Nature, 178, 1113.
27. Takahashi, T., Nagano, T., Wada, K., Ikegaya, M. and Tagai, H., (1971), J.Metal.Finish Soc.,22, 490.
28. Thompson, G.E. and Wood, G.C., (1981), Nature, 290, 320.
29. Vedder, W. and Vermilyea, D.A., (1969), Trans. Faraday Soc., 52, 561.
30. Venables, J.D., McNamara, D.K., Chen, J.M., Ditchek, B.M., Morgenthaler, T.I., Sun, T.S. and Hopping, R.L., (1980), 12th National SAMPE Technical Conference, October 7-9 1980, (SAMPE, Azusa, California), 909.
31. Wilsdorf, R.W.G., (1951), Nature (London),168, 600.

APPENDIX III

A MATHEMATICAL MODEL FOR THE SECONDARY ELECTRON ESCAPE PROCESS

A simple theory of the secondary electron escape process from the surface of a solid applicable to the photon energy band 1500-2500 eV, which gives the maximum kinetic energy of the electron cascade has been described by Jones and Woodruff, (1982). The total electron yield EXAFS spectrum arising from a thin oxide layer on a metal substrate has components from the two phases with proportions depending on the oxide film thickness.

The effective sampling depth of the total electron yield technique can be obtained from a mathematical model of the electron escape process. Consider a slab of thickness dz , a distance z below the surface, figure 1. A soft X-ray photon of intensity I_0 is incident at an angle ϕ to the surface. The photon travels a distance ℓ , through the slab dz . By assuming that: (i) the photon is not attenuated by passing through z or dz and (ii) the number of ionization events within dz is proportional to the path length of the photon ℓ , figure 2.

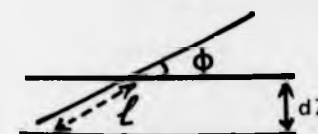


Figure 2

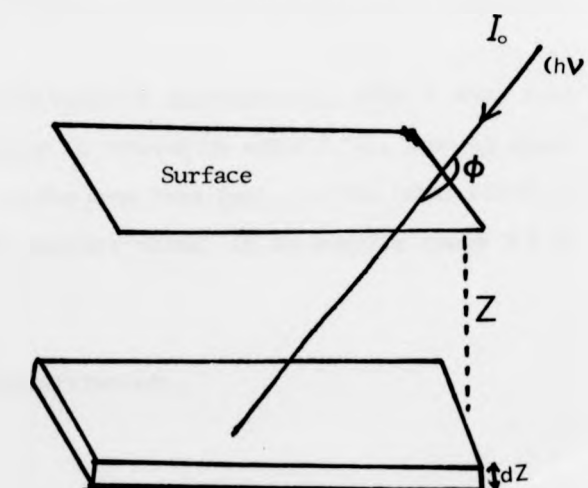


Figure 1

then the electron flux generated within the slab dz is proportional to the photon intensity I_0 , the absorption coefficient (μ), and the path length l . With $l = dz/\sin \phi$, the total electron flux over the full 2π is proportional to $I_0 \mu dz/\sin \phi$, and the total electron flux travelling upwards (i.e. in a direction out of the surface) is proportional to $I_0 \mu dz/2\sin \phi$. Now, if we consider a narrow cone of emission at an angle θ , of width $d\theta$, as shown in figure 3, the number of electrons emitted at an angle θ is proportional to the solid angle defined by $d\Omega$.

solid angle ($d\Omega$) $\equiv \sin \theta d\theta$

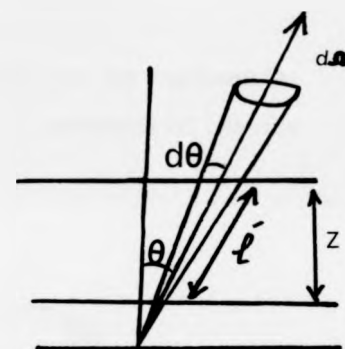


Figure 3

The path length of the electrons out the surface is l' at angle θ , where $l' = z/\cos \theta$.

If the electrons are attenuated exponentially with a mean free path λ , the electron intensity is reduced by $\exp(-l'/\lambda)$, this is equal to $\exp(-z/\lambda \cos \theta)$, where λ is the mean free path, so the total electron yield at an angle θ to the surface normal in an angular range $d\theta$ is given by:

$$(I_0 \mu / 2 \sin \phi) \exp(-z/\lambda \cos \theta) \sin \theta dz d\theta$$

Putting $\mu' = \mu/\sin\phi$, μ being the X-ray absorption coefficient and ϕ the angle of photon incidence, we obtain:

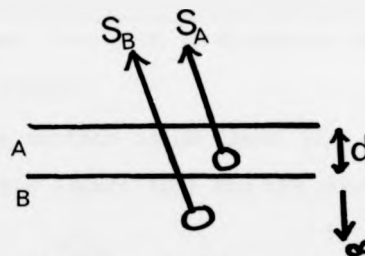
$$(I_0\mu'/2)\exp(-z/\lambda\cos\theta)\sin\theta d\theta dz$$

If we now integrate over a film thickness d ($z = 0$ to $z = d$) and over the whole angular range ($\theta = 0$ to $\theta = \pi/2$), the total electron yield for a thin film (A) is obtained

$$S_A = \left[\frac{I_0\mu'\lambda}{4} \right] \left\{ 1 - \exp\left[-\frac{d}{\lambda}\right] \left[1 - \left(\frac{d}{\lambda}\right) - \left(\frac{d^2}{\lambda^2}\right) \text{Ei}\left(\frac{d}{\lambda}\right) \right] \right\}$$

where $\text{Ei}(x) = \text{Ei}(x) = \int_x^\infty (\exp(-v)/v) dv$ and $\text{Ei}(x)$ is the exponential integral, calculated from standard handbook of mathematical tables (reference 3).

Figure 4



Now consider an oxide film A, of thickness d , on a substrate B, as shown in figure 4. The contribution to the total electron yield from A, S_A , has already been calculated, and we expect an additional contribution from the layer B. This contribution, S_B , is the emission due to the infinite layer B, after it has been attenuated by layer A. So the signal due to infinite layer B (by itself) is:

$$S_{1G} = \frac{I_0\mu'_B\lambda}{4} \left\{ 1 - f\left(\frac{\infty}{\lambda_B}\right) \right\} = \text{const}$$

$$S_B = \underbrace{\left[\frac{I_0\mu'_B\lambda}{4} \right] \left\{ 1 - f\left(\frac{\infty}{\lambda_B}\right) \right\}}_{\text{constant}} \underbrace{\int \exp(-d/\lambda\cos\theta)\sin\theta d\theta}_{\text{attenuation due to layer A}}$$

Consider $f\left(\frac{d}{\lambda}\right) = \exp(-d/\lambda) \left[1 - \left(\frac{d}{\lambda}\right) + \left(\frac{d^2}{\lambda^2}\right) \text{Ei}\left(\frac{d}{\lambda}\right) \right]$ in S_A and S_B .

The relative contributions from the film (A) and the substrate (B) is given by

$$S_A/S_B = \left[\frac{\mu'_A \lambda_A}{\mu'_B \lambda_B} \right] \frac{1-f(d/\lambda_A)}{f(d/\lambda_A)}$$

where λ_A and λ_B are an estimate of the mean free path of an electron in the surface oxide layer (A) and bulk aluminium layer (B). At high energies it has been found that the inelastic scattering mean free path in the surface of aluminium oxide is about twice that in the substrate metal (Norman and Woodruff, 1978):

$$\lambda_A = 2\lambda_B$$

The inelastic scattering mean free path in aluminium metal is $\lambda_B = 65 \text{ \AA}$ (see Jones and Woodruff, 1982).

The signal due to the surface oxide layer (S_A) relative to the total signal detected from the layers (S_A) and the substrate (S_B) is:

$$\frac{S_A}{S_A + S_B} = \left| 1 + \frac{\mu'_B \lambda_B}{\mu'_A \lambda_A} \frac{1}{(f(d/\lambda_A))^{-1}} \right|^{-1}$$

where μ_A and μ_B are the appropriate X-ray absorption coefficients for the different densities of absorber (Al density = 2.702 g cm^{-3} and $\text{Al}_2\text{O}_3 = 2.20 \text{ g cm}^{-3}$). The ratio of the absorption coefficients for the same spectral range around the Al K-edge are related to the density of the aluminium atoms in the oxide and the metal substrate and therefore $\mu_A/\mu_B = \frac{\mu'_{\text{Al}_2\text{O}_3}}{\mu'_{\text{Al}}} = \frac{\rho_{\text{Al}_2\text{O}_3}}{\rho_{\text{Al}}} = 0.82$. The proportional of the contribution from the oxide film in the total electron yield ($S_A/(S_A+S_B)$), according to this simple

mathematical model, is shown in figure 3.6.3. A comparison of the results from this model and the experimental data shows a good agreement, and confirms the conclusion that a reliable sampling of the oxide structure can be obtained for films with a thickness greater than 500 Å.

REFERENCES

1. Norman, D. and Woodruff, D.P., (1978), Surface Science, 75, 179.
2. Jones, R.G. and Woodruff, D.P., (1982), Surface Science, 114, 38.
3. CRC Handbook of Mathematical Sciences (Cleveland, Ohio).